

On Metaplectic Geometrical Optics

for Ray Tracing in Fusion Plasmas

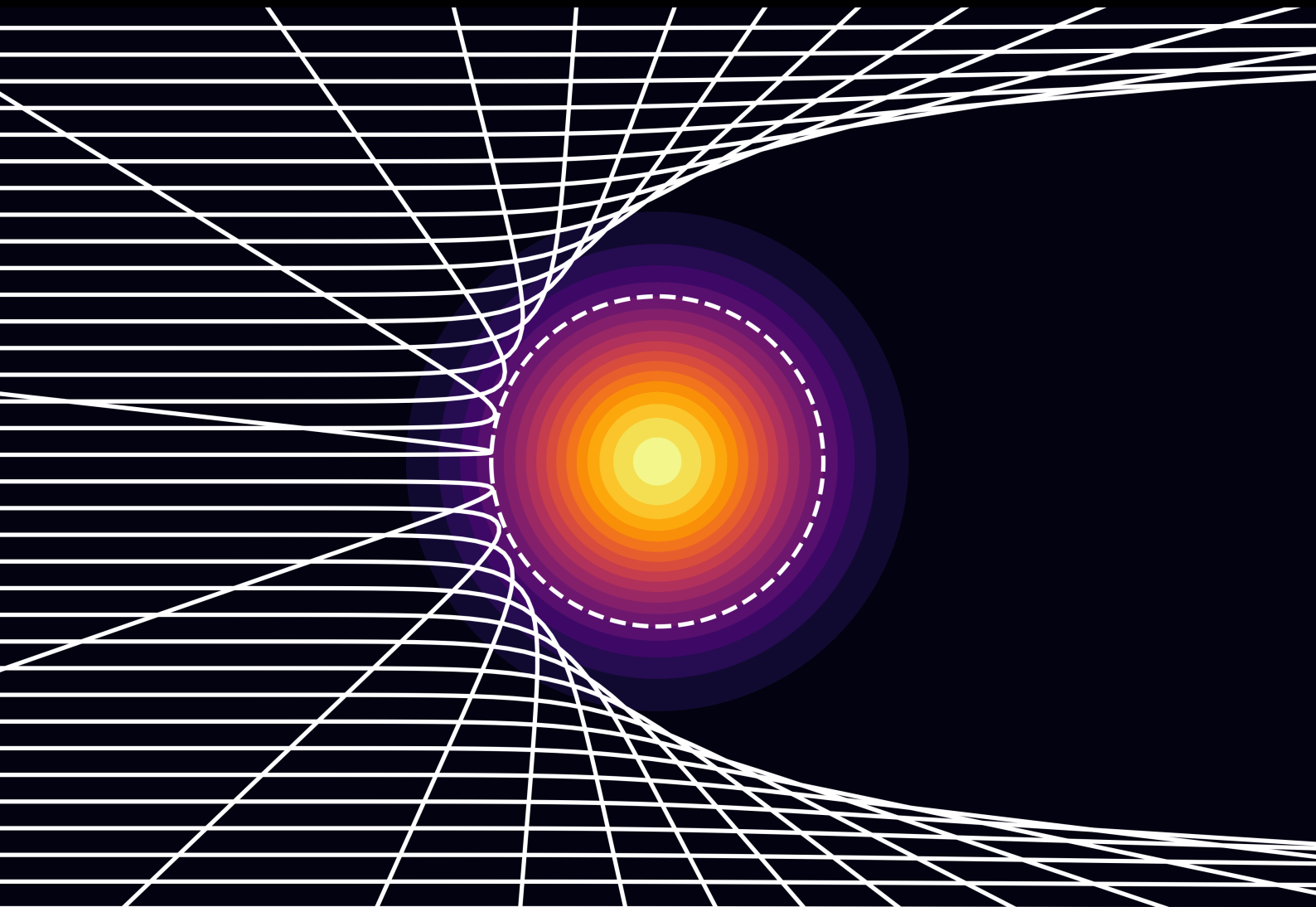
Master's Thesis

July 29th, 2023

By Rune J. O. Højlund (s173965)

Supervisor: Stefan Kragh Nielsen

Co-supervisor: Mads Givskov Senstius



On Metaplectic Geometrical Optics
for Ray Tracing in Fusion Plasmas

Master's Thesis
July 29th, 2023

By
Rune J. O. Højlund

Copyright: Reproduction of this publication in whole or in part must include the customary bibliographic citation, including author attribution, report title, etc.

Published by: DTU, Plasma Physics and Fusion Energy, Bovej, Building 118, 2800 Kgs. Lyngby Denmark

<https://www.fysik.dtu.dk/english>

Approval

This thesis has been prepared over six months at the Section for Plasma Physics and Fusion Energy, at the Technical University of Denmark, DTU, in partial fulfillment for the degree: Master of Science in Engineering Physics, MSc Eng.

Rune J. O. Højlund - s173965

.....
Signature

.....
Date

Abstract

Ray tracing methods based on geometrical optics (GO) are widely used when designing heating systems and non-invasive diagnostics for fusion plasmas. Unfortunately the underlying eikonal (WKB) approximation behind GO theory breaks down at locations where the length scale of variations in the medium is on the order of the wavelength of the field. Such locations are called caustics and they are typically points where rays from the wave are reflected (cutoffs) or focused. As it turns out, caustics are extremely common in plasmas and for many phenomena they are the main points of interest. The breakdown means that the wave amplitude obtained from ray tracing erroneously diverges in the vicinity of caustics. The few strategies, such as Maslov's method, that exist to treat caustics in a systematic way have the disadvantage that they are difficult to implement in a robust automated manner which does not require supervision. A better method for reduced numerical modeling of wave caustics is clearly needed.

In the recent works by N. A. Lopez, I. Y. Dodin and S. M. Donnelly published between 2019 to 2022, the authors propose a new approach called metaplectic geometrical optics (MGO) for reinstating the validity of GO in caustic regions. The method has so far been demonstrated analytically on selected bench-marking examples, but it remains to be implemented in a fully automated numerical ray-tracing code. In this thesis project I have developed a first of its' kind automated numerical implementation of the MGO method proposed by Lopez et al. I demonstrate my implementation on the two bench-marking examples of Airy's equation and Weber's equation which both have a relevant interpretation within plasma physics as well as within quantum mechanics. In both instances, I find that the numerical implementation is able to reproduce the exact results with great accuracy even at caustics. Furthermore, I apply MGO to the case of X-B coupling close to the upper hybrid layer in a plasma with both a constant and a variable local temperature profile. Compared to the non-dimensionalized examples of Airy's and Weber's equation, the XB-coupling example has an entirely different scaling of variables and a much more complicated dispersion relation. I find that my proposed implementation yields reliable results for XB-coupling with a constant temperature profile, but fails to reconstruct the correct field in the more complicated example of X-B-coupling with a varying temperature profile. I suggest three possible contributing error sources behind this behavior and points to the further work needed to solve these technical issues.

In summary I find that MGO presents an extremely promising new paradigm for efficient reduced numerical wave modeling. The openly available code developed as part of this project and the documentation in this thesis delivers many practical solutions to the technical problems that follows with a numerical implementation. Though the examples of MGO shown in this thesis are all one-dimensional, much of the preparatory work for a multidimensional MGO simulation has been worked out in the numerical implementation. Importantly, the method of MGO and its' numerical implementation developed in this project is completely agnostic to the type of wave equation and classification of caustic. Therefore this work lays the groundwork for the efficient reduced modeling of wave fields in many more areas.

Acknowledgements

I would like to thank my supervisors, Steffen Krogh, and Mads Senstius, for keeping the project on the right track and taking aside many hours for detailed technical discussions. Also I would like to say my thanks to Dr. Nicolas Lopez for developing the metaplectic geometrical optics framework, which I have had the pleasure of studying in this project and for readily answering my technical questions hereto. Finally I would like to give a special thanks to my daughter, Thea Jo Højlund Marholt, for brightening every day with her giggle and to Stine Amalie Marholt for always being there and for her deep and infectious interest in physics.

Contents

| | |
|---|-----------|
| Preface | ii |
| Abstract | iii |
| Acknowledgements | iv |
| 1 Introduction | 1 |
| 1.1 Motivation | 1 |
| 1.2 Structure of this thesis | 2 |
| 2 Cold Plasma Waves | 3 |
| 2.1 Wave Equation for a Cold Homogeneous Linear Plasma | 3 |
| 2.1.1 The Conductivity Response | 4 |
| 2.2 Electron Waves | 5 |
| 2.3 Ordinary (O) and Extraordinary (X) Mode | 6 |
| 2.3.1 Cutoffs and Resonances | 6 |
| 2.3.2 Perpendicular and Parallel Solutions | 7 |
| 2.3.3 CMA Diagram | 8 |
| 3 Mathematical Foundation of Phase Space Analysis | 9 |
| 3.1 The Hilbert Space | 9 |
| 3.1.1 Position and Momentum Operator | 10 |
| 3.1.2 Fourier Transforms | 12 |
| 3.2 Weyl Symbol Calculus | 12 |
| 3.2.1 Symplectic Phase Space Translations | 13 |
| 3.2.2 Wigner Operator | 14 |
| 3.2.3 Wigner-Weyl Transform ($\hat{A} \mapsto \mathcal{A}(\mathbf{z})$) | 15 |
| 3.2.4 Inverse Wigner-Weyl Transform ($\mathcal{A}(\mathbf{z}) \mapsto \hat{A}$) | 15 |
| 3.2.5 Important Weyl Correspondences | 16 |
| 4 Geometrical Optics | 19 |
| 4.1 The Stationary Scalar Wave Equation | 19 |
| 4.2 The Eikonal Approximation (WKB) | 20 |
| 4.3 Ray Tracing | 23 |
| 4.3.1 Hamilton's Ray Equations | 25 |
| 4.3.2 Field Reconstruction | 26 |
| 4.3.3 The Caustic Problem | 27 |
| 4.4 Numerical Details | 28 |
| 4.4.1 Calculating Derivatives | 29 |
| 4.4.2 Solving Hamilton's Ray Equations | 32 |
| 4.4.3 Constructing the Field | 32 |
| 5 Examples of Geometrical Optics | 35 |
| 5.1 Traces of O and X mode in cold plasma | 35 |
| 5.2 Airy's Equation (O-mode perpendicular to \mathbf{B}_0) | 38 |
| 5.2.1 Integral Representation and Asymptotic Approximation | 39 |
| 5.2.2 Ray Tracing Airy's Equation | 40 |
| 5.2.3 Numerical Results within geometrical optics (GO) for Airy's Equation | 40 |
| 5.3 Weber's Equation (Quantum harmonic oscillator (QHO)) | 41 |

| | | |
|---------------------------|--|------------|
| 5.3.1 | Ray Tracing Weber's Equation | 42 |
| 5.3.2 | Numerical Results within geometrical optics (GO) for Weber's Equation | 42 |
| 5.4 | Two-dimensional plasma | 44 |
| 6 | Metaplectic Geometrical Optics | 49 |
| 6.1 | Fourier Transformation as a Strategy for Treating Caustics | 49 |
| 6.2 | Symplectic Phase Space Rotations | 51 |
| 6.2.1 | Orthosymplectic Transformations | 52 |
| 6.2.2 | Generator Formalism | 53 |
| 6.2.3 | Orthosymplectic Transformation For Singular \mathbf{B} | 53 |
| 6.3 | Metaplectic Transforms | 54 |
| 6.4 | Geometrical Optics in Rotated Phase Space | 56 |
| 6.5 | The metaplectic geometrical optics (MGO) Recipe | 57 |
| 6.5.1 | Determining orthosymplectic matrix \mathbf{S}_t | 58 |
| 6.5.2 | Obtaining the Wave Field in Rotated Phase Space | 59 |
| 6.5.3 | Linking Solutions with Near-Identity Metaplectic Transform | 60 |
| 6.5.4 | Obtaining Final Solution in the Original Space | 60 |
| 6.5.5 | Analytic Continuation using Function Fits | 61 |
| 6.6 | Summary of metaplectic geometrical optics (MGO) | 61 |
| 7 | Results from Numerical Metaplectic geometrical optics (MGO) Algorithm | 65 |
| 7.1 | Airy's Equation | 65 |
| 7.1.1 | Analytic Derivation of metaplectic geometrical optics (MGO) Solution to Airy's Equation | 65 |
| 7.1.2 | Numerical Results for Airy's Equation | 67 |
| 7.2 | Weber's Equation | 71 |
| 7.2.1 | Analytic Derivation of metaplectic geometrical optics (MGO) Solution to Weber's Equation | 72 |
| 7.2.2 | Numerical Results for Weber's Equation | 74 |
| 7.3 | X-B Coupling at the upper hybrid layer in a warm plasma | 81 |
| 8 | Conclusion | 93 |
| Bibliography | | 95 |
| A Appendix | | 99 |
| A.1 | Notation | 99 |
| A.2 | Acronyms | 102 |
| B Gauss Quadrature | | 103 |
| B.1 | Polynomial Interpolation | 103 |
| B.2 | Sturm-Liouville Theory and Orthogonal Polynomials | 104 |
| B.3 | Gaussian Quadrature | 106 |

1 Introduction

*Shine for them, O disk of day, great of dignity.
All distant lands, you make them live. [...]
Your rays nursing every meadow.
You shine and they live and grow for you.*

Excerpt from translation of ancient Egyptian hymn to the sun god Aton

1.1 Motivation

Research in fusion plasmas is driven by the goal of realizing self-sustained controlled thermonuclear fusion in order to develop a sustainable and reliable energy source for humanity's future generations (Ref. [1]). Crucial to this endeavor is the modeling of plasma waves which play a central role in numerous applications including non-invasive diagnostics, plasma heating, current drive and suppression of instabilities to name a few (Refs. [2, 3]). At the same time there is an incredible variety in the types of waves which may exist in a plasma. The possible frequencies span from the MHz-range of the ion-cyclotron frequency to the GHz range relevant for electron cyclotron resonance heating. This is reflected in the methods used for modeling plasma waves as well. At low frequencies it may be possible to use full-wave models which solve the complete Maxwell equations. However, at high frequencies with short wavelengths, the computational cost of full-wave simulations are often too impractical to be useful (Ref. [4]). A standard approach when analyzing and designing experiments is therefore to rely instead on numerical ray tracing methods based on the theory of geometrical optics (GO).

At the core of GO is the eikonal approximation also known as the WKB or LG approximation (Ref. [5, p. 22]). The approximation assumes that the field can be written in the form

$$\psi(\mathbf{x}) = \phi(\mathbf{x})e^{i\theta(\mathbf{x})}, \quad (1.1)$$

where the amplitude $\phi(\mathbf{x})$ is assumed to vary much more slowly compared to the phase $\theta(\mathbf{x})$. This can also be expressed in the eikonal parameter which is assumed small:

$$\epsilon = \frac{1}{kL} \ll 1 \quad (1.2)$$

Here the wave number $k \sim \partial_{\mathbf{x}}\theta$ defines the phase variation scale and $1/L \sim \partial_{\mathbf{x}}\phi$ defines the envelope variation scale. The envelope follows the background and in this way the eikonal approximation can be seen as requiring that the variation in the background is much longer than the wavelength (Ref. [4, 6]). A gradually varying medium satisfying the eikonal criterion is sometimes said to be weakly inhomogeneous (Ref. [3]). As I shall show in chapter 4, the eikonal approximation is extremely useful, since it converts the original wave equation, which might be a partial differential equation (PDE) or integro-differential equation, into a much simpler initial value problem (IVP). The IVP is in the form of Hamilton's equations and it defines the wave field propagation through the evolution of single line rays. In the method of GO one evolves a finite family of rays from which the entire field in a given region can be reconstructed (Ref. [5]).

However, the eikonal approximation breaks down at points where $kL \rightarrow 0$. These points are known as caustics. Typically caustics are turning points where light rays are reflected

$(k \rightarrow 0)$ or focal points where light rays converge ($L \rightarrow 0$) (Ref. [7]). As I shall show examples of in this thesis, caustics are commonly occurring in plasmas. More importantly, it is often exactly at caustic points that we are interested in knowing the wave field values (Ref. [8]). Currently there exists a few strategies to solve the caustic problem, of which Maslov's method is the most consolidated (Ref. [9]). Maslov's method which I shall explain in chapter 6 works by Fourier transforming the wave field, whenever the ray gets close to a caustic. However, the method is difficult to implement in an automated way that gives reliable results without requiring external supervision.

Recently a new method known as metaplectic geometrical optics (MGO) has been proposed as a way of reinstating the validity of GO in caustic regions (Refs. [10, 11, 12, 7, 8]). It is this method which I study in this thesis. As in Plato's Cave, MGO recognizes that the ray trajectories we observe in position space are in fact mere projections of more ideal rays residing in a higher-dimensional phase space. From this viewpoint, caustics occur when the projection of rays from phase space to position space becomes ill-defined. The good news is that this projection singularity can be lifted by formulating the GO equations in a rotated phase space. I shall present the theory of the method in detail in chapter 6.

In Refs. [10, 11, 12, 7, 8], Lopez et al. demonstrates their MGO method analytically on a few key examples, but the method remains to be implemented in a fully automated numerical ray tracing code. This is where my thesis project comes in. During this thesis I have developed an automated implementation of the MGO framework. The code I have developed is accessible on a repository on GitHub, Ref. [13]. In chapter 7 I shall present the results of applying my numerical implementation to the examples of Airy's equation, Weber's equation and XB-coupling. Overall, I find that MGO is a really promising method which is capable of reconstructing the exact wave fields even at caustics.

1.2 Structure of this thesis

The thesis is structured as follows. In the next chapter, chapter 2, I derive the theory of fundamental plasma waves under the standard assumption of cold homogeneous plasmas. I shall use these results in examples throughout the thesis. In chapter 3 I make a mathematical intermezzo in order to review some necessary prerequisites for deriving the GO and MGO theory. These are the analysis of Hilbert spaces and Weyl symbol calculus. In chapter 4 I then derive the theory of GO using the Weyl symbol calculus. I then move on to apply these results in a numerical implementation in chapter 5. This also allows me to introduce the Airy and Weber equation examples properly, which I later apply the MGO method to. In chapter 6 I am then finally ready to present the main ideas of the MGO theory as presented in Refs. [10, 11, 12, 7, 8]. The thesis culminates in chapter 7 where I demonstrate results from applying my numerical implementation of the MGO method. Finally the conclusion is given in chapter 8.

2 Cold Plasma Waves

This thesis is about modeling wave phenomena in general, but the methods presented are of particular value to plasma physics. Therefore, in this chapter I will derive the basic types of waves that may occur in a cold homogeneous plasma. The end result of the derivation is that a cold plasma may support two modes: The *ordinary* (O) and *extraordinary* (X) mode. I shall use the derived dispersion relation, eq. (2.20 AAH) of these modes in examples throughout the thesis. The derivation is based on Refs. [2, 3, 1].

2.1 Wave Equation for a Cold Homogeneous Linear Plasma

Plasma waves are electromagnetic in nature and the starting point for the study of plasma waves is therefore the Maxwell curl equations:

$$\partial_{\mathbf{x}} \times \mathbf{E} = -\partial_t \mathbf{B} \quad (2.1a)$$

$$\partial_{\mathbf{x}} \times \mathbf{B} = \mu_0 \mathbf{J} + \frac{1}{c^2} \partial_t \mathbf{E}. \quad (2.1b)$$

The plasma physics is packed away in the current density which in the two-fluid picture is:

$$\mathbf{J} = \sum_{\sigma} n_{\sigma} q_{\sigma} \mathbf{u}_{\sigma} \quad (2.2)$$

where $\sigma \in \{e, i\}$ denotes the charge species (electrons or ions), n_{σ} is the density, q_{σ} is the charge and \mathbf{u}_{σ} is the fluid velocity. I will assume that the medium is described by the two-fluid momentum equation:

$$m_{\sigma} n_{\sigma} (\partial_t + \mathbf{u}_{\sigma} \cdot \partial_{\mathbf{x}}) \mathbf{u}_{\sigma} = n_{\sigma} q_{\sigma} (\mathbf{E} + \mathbf{u}_{\sigma} \times \mathbf{B}). \quad (2.3)$$

Note, that this assumes the plasma to be cold such that the thermal effects from the pressure gradient, viscosity tensor and collisions can be neglected.

Taking the curl of eq. (2.1a) and inserting eq. (2.1b) gives the plasma wave equation:

$$\partial_{\mathbf{x}} \times \partial_{\mathbf{x}} \times \mathbf{E} + \frac{1}{c^2} \partial_t^2 \mathbf{E} + \mu_0 \partial_t \mathbf{J} = \mathbf{0}. \quad (2.4)$$

I assume the medium is linear (see Refs. [2, 3]) such that¹:

$$\mathbf{J}(\mathbf{x}, t) = \int d\mathbf{x}' \int dt' \boldsymbol{\sigma}(\mathbf{x}, \mathbf{x}', t, t') \cdot \mathbf{E}(\mathbf{x}', t'), \quad (2.5)$$

where the dielectric tensor $\boldsymbol{\sigma}$ gives the current response to an electric field (see e.g. Ref. [3, p. 18], [2, p. 5] or Ref. [14, p. 95]). Furthermore, I also assume that the medium is homogeneous in space and time-stationary. I.e. $\boldsymbol{\sigma}(\mathbf{x}, \mathbf{x}', t, t') = \boldsymbol{\sigma}(\mathbf{x} - \mathbf{x}', t - t')$. Under this assumption, the Fourier transform of eq. (2.5) with respect to both space and time (see eqs. (3.23) and (3.21 FT)) turns the convolution into a matrix product:

$$\tilde{\mathbf{J}}(\mathbf{k}, \omega) = \tilde{\boldsymbol{\sigma}}(\mathbf{k}, \omega) \cdot \tilde{\mathbf{E}}(\mathbf{k}, \omega). \quad (2.6)$$

¹Note that I have let the time integral go from $-\infty$ to ∞ under the assumption that $\boldsymbol{\sigma}$ is the retarded response and the transient behavior is insignificant.

Assuming that the fields are localized, the Fourier transform over \mathbf{x} and t of eq. (2.4) effectively maps $\partial_{\mathbf{x}} \rightarrow i\mathbf{k}$ and $\partial_t \rightarrow -i\omega$ and the wave equation in (\mathbf{k}, ω) -space therefore is:

$$-\mathbf{k} \times \mathbf{k} \times \tilde{\mathbf{E}} - \frac{\omega^2}{c^2} \tilde{\mathbf{E}} - i\mu_0\omega\tilde{\boldsymbol{\sigma}} \cdot \tilde{\mathbf{E}} = 0$$

Let me introduce the refractive index \mathbf{N} and dielectric tensor $\tilde{\boldsymbol{\epsilon}}$:

$$\mathbf{N} := \frac{c\mathbf{k}}{\omega}, \quad (2.7)$$

$$\tilde{\boldsymbol{\epsilon}} := \mathbf{I} + \frac{i}{\omega\epsilon_0}\tilde{\boldsymbol{\sigma}}, \quad (2.8)$$

where \mathbf{I} is the identity tensor. Using that $c^2 = (\mu_0\epsilon_0)^{-1}$, the wave equation becomes

$$\mathbf{N} \times \mathbf{N} \times \tilde{\mathbf{E}} + \tilde{\boldsymbol{\epsilon}} \cdot \tilde{\mathbf{E}} = 0$$

The double cross product may also be written as (see e.g. Ref. [15, p. 38, eq. (V.2)])

$$\mathbf{N} \times \mathbf{N} \times \tilde{\mathbf{E}} = \mathbf{NN} \cdot \mathbf{E} - \mathbf{N} \cdot \mathbf{NE} = (\mathbf{NN} - N^2\mathbf{I}) \cdot \mathbf{E}.$$

Note that I use implicit outer products (see appendix A.1 for clarifications on the notation). Therefore the wave equation also has the form:

$$[\mathbf{NN} - N^2\mathbf{I} + \tilde{\boldsymbol{\epsilon}}] \cdot \tilde{\mathbf{E}} = 0 \quad (2.9)$$

2.1.1 The Conductivity Response

To determine the conductivity and dielectric tensor I use the two-fluid momentum equation eq. (2.3). I will assume that the fields are linearized without static terms for the fluid velocity and electric field:

$$\mathbf{E}(\mathbf{r}, t) \approx \mathbf{E}_1(\mathbf{r}, t), \quad \mathbf{B}(\mathbf{r}, t) \approx \mathbf{B}_0 + \mathbf{B}_1(\mathbf{r}, t), \quad \mathbf{u}_{\sigma}(\mathbf{r}, t) \approx \mathbf{u}_{\sigma,1}(\mathbf{r}, t). \quad (2.10)$$

Keeping only first order terms simplifies the advective derivative and cross product of eq. (2.3):

$$\begin{aligned} (\partial_t + \mathbf{u}_{\sigma} \cdot \partial_{\mathbf{x}}) \mathbf{u}_{\sigma} &\approx \partial_t \mathbf{u}_{\sigma,1} \\ \mathbf{u}_{\sigma} \times \mathbf{B} &\approx \mathbf{u}_{\sigma,1} \times \mathbf{B}_0. \end{aligned}$$

The Fourier transform of the momentum equation, eq. (2.3), thereby is:

$$-i\omega m_{\sigma} n_{\sigma} \tilde{\mathbf{u}}_{\sigma,1} = n_{\sigma} q_{\sigma} \tilde{\mathbf{E}}_1 + n_{\sigma} q_{\sigma} \tilde{\mathbf{u}}_{\sigma,1} \times \mathbf{B}_0. \quad (2.11)$$

To simplify the equations further, I may choose my coordinate system such that $\mathbf{B} = (0, 0, B)^T$ is parallel to x_3 and $\mathbf{k} = (k_{\perp}, 0, k_{\parallel})^T$ and by extension $\mathbf{N} = (N_{\perp}, 0, N_{\parallel})^T$ lies in the (x_1, x_3) plane. This is sometimes referred to as the Stix basis and is illustrated on fig. 2.1. Note how \perp, \parallel refers to the direction perpendicular and parallel to the magnetic field respectively. Using this convention, eq. (2.11) gives the fluid velocity:

$$\tilde{\mathbf{u}}_{\sigma,1} = i \frac{q_{\sigma}\omega}{m_{\sigma}} \begin{pmatrix} \frac{1}{\omega^2 - \omega_{c\sigma}^2} & -s_{\sigma}i \frac{1}{\omega^2 - \omega_{c\sigma}^2} \frac{\omega_{c\sigma}}{\omega} & 0 \\ s_{\sigma}i \frac{1}{\omega^2 - \omega_{c\sigma}^2} \frac{\omega_{c\sigma}}{\omega} & \frac{1}{\omega^2 - \omega_{c\sigma}^2} & 0 \\ 0 & 0 & 1 \end{pmatrix} \cdot \tilde{\mathbf{E}}_1, \quad (2.12)$$

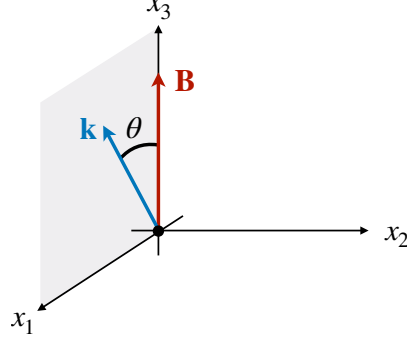


Figure 2.1: Illustration of the Stix basis convention. The coordinate system is chosen such that the magnetic field \mathbf{B} is along the x_3 -axis and the wave vector \mathbf{k} lies in the (x_1, x_3) -plane.

where $s_\sigma = \text{sign } q_\sigma$ is the sign of the charge and I introduced the cyclotron frequencies for the electrons and ions:

$$\omega_{c\sigma} := \frac{|q_\sigma|B_0}{m_\sigma}. \quad (2.13)$$

$\omega_{c,\sigma}$ is the characteristic frequency of the circular orbit a charged particle in a magnetic field makes around its' guiding center. To get an estimate of the range of typical cyclotron frequencies, take $e \approx 1.6 \times 10^{-19} \text{ C}$ and $B_0 = 0.5 \text{ T}$ and use $m_e \approx 9 \times 10^{-31} \text{ kg}$ and $m_i \approx 3 \times 10^{-27} \text{ kg}$ (corresponding to Deuterium). The ion cyclotron frequency then is $\omega_{ci} \approx 2.4 \times 10^7 \text{ Hz}$ and the electron cyclotron frequency is $\omega_{ce} \approx 9 \times 10^{10} \text{ Hz}$. Evidently, the ion cyclotron frequencies are in the MHz range whereas the electron cyclotron frequencies are typically in the GHz range. Since the ions are much heavier than the electrons their gyro motion is much slower.

Now, the conductivity is found by plugging the fluid velocity, eq. (2.12), into Ohms law, eq. (2.6):

$$\tilde{\sigma} = \begin{pmatrix} \tilde{\sigma}_{11} & \tilde{\sigma}_{12} & 0 \\ -\tilde{\sigma}_{12} & \tilde{\sigma}_{11} & 0 \\ 0 & 0 & \tilde{\sigma}_{33} \end{pmatrix}, \quad \text{where} \quad (2.14a)$$

$$\tilde{\sigma}_{11} = i\omega\epsilon_0 \left[\sum_\sigma \frac{\omega_{p\sigma}^2}{\omega^2 - \omega_{c\sigma}^2} \right], \quad \tilde{\sigma}_{12} = i\omega\epsilon_0 \left[i s_\sigma \sum_\sigma \frac{\omega_{p\sigma}^2}{\omega^2 - \omega_{c\sigma}^2} \frac{\omega_{c\sigma}}{\omega} \right], \quad \tilde{\sigma}_{33} = i\omega\epsilon_0 \left[\sum_\sigma \frac{\omega_{p\sigma}^2}{\omega^2} \right], \quad (2.14b)$$

where I introduced the plasma frequencies:

$$\omega_{p\sigma} := \sqrt{\frac{n_\sigma q_\sigma^2}{\epsilon_0 m_\sigma}}. \quad (2.15)$$

2.2 Electron Waves

In many applications within plasma diagnostics and electron cyclotron resonance heating, the frequency ranges used are much higher than the ion plasma and cyclotron frequencies (Ref. [3]). The examples I consider in this thesis will therefore be high frequency waves, i.e. in the GHz-range of the electron cyclotron frequency. Note however, that the methods

I present in later chapters are in no way limited to high frequency applications. In the regime where $\omega \gg \omega_{pi}, \omega_{ci}$ all terms in eq. (2.14b) with ion frequencies are negligible and the ion terms are therefore ignored in the sum. Plugging into eq. (2.8) under the assumption that $\omega \gg \omega_{pi}, \omega_{ci}$ then gives me the following dielectric tensor (Ref. [3]):

$$\tilde{\boldsymbol{\epsilon}} = \begin{pmatrix} \tilde{\epsilon}_{11} & \tilde{\epsilon}_{12} & 0 \\ -\tilde{\epsilon}_{12} & \tilde{\epsilon}_{11} & 0 \\ 0 & 0 & \tilde{\epsilon}_{33} \end{pmatrix}, \quad \text{where} \quad (2.16)$$

$$\tilde{\epsilon}_{11} = 1 - \frac{\omega_{pe}^2}{\omega^2 - \omega_{ce}^2}, \quad \tilde{\epsilon}_{12} = i \frac{\omega_{pe}^2}{\omega^2 - \omega_{ce}^2} \frac{\omega_{ce}}{\omega}, \quad \tilde{\epsilon}_{22} = 1 - \frac{\omega_{pe}^2}{\omega^2}, \quad (2.17)$$

Now that I have obtained the dielectric tensor $\tilde{\boldsymbol{\epsilon}}$ in the high frequency regime, $\omega \gg \omega_{pi}, \omega_{ci}$, I can return to the wave equation eq. (2.9). Using that $\mathbf{N} = (N_\perp, 0, N_\parallel)$ the wave equation becomes (Ref. [3]):

$$\mathcal{D}\tilde{\mathbf{E}} = \begin{pmatrix} \tilde{\epsilon}_{11} - N_\parallel^2 & \tilde{\epsilon}_{12} & N_\parallel N_\perp \\ -\tilde{\epsilon}_{12} & \tilde{\epsilon}_{11} - N_\parallel^2 & 0 \\ N_\parallel N_\perp & 0 & \tilde{\epsilon}_{33} - N_\perp^2 \end{pmatrix} \begin{pmatrix} \tilde{E}_1 \\ \tilde{E}_2 \\ \tilde{E}_3 \end{pmatrix} = 0 \quad (2.18)$$

For the equation to have non trivial solutions, the determinant of \mathcal{D} must be 0. This determines the dispersion relation (Ref. [3]):

$$\tilde{\epsilon}_{11} N_\perp^4 - N_\perp^2 \left[\tilde{\epsilon}_{12}^2 + (\tilde{\epsilon}_{11} + \tilde{\epsilon}_{33}) (\tilde{\epsilon}_{11} - N_\parallel^2) \right] + \tilde{\epsilon}_{33} \left[(\tilde{\epsilon}_{11} - N_\parallel^2)^2 + \tilde{\epsilon}_{12}^2 \right] = 0 \quad (2.19)$$

Note that $N_\parallel = N \cos(\theta), N_\perp = N \sin(\theta)$, where θ is angle between the wave vector and magnetic field (see fig. 2.1). By using this and inserting the expression from eq. (2.17), the relation in eq. (2.19) becomes the Altar-Appleton-Hartree (AAH) dispersion relation (Refs. [2, p. 38], [3, p. 24]):

$$\mathcal{D}(\mathbf{x}, \mathbf{N}, \omega) = 1 - N^2 - \frac{2\omega_{pe}^2(\omega^2 - \omega_{pe}^2)/\omega^2}{2(\omega^2 - \omega_{pe}^2) - \omega_{ce}^2 \sin^2(\theta) \pm \omega_{ce} \Delta} = 0, \quad (2.20 \text{ AAH})$$

$$\text{where } \Delta := \left[\omega_{ce}^2 \sin^4(\theta) + 4\omega^{-2} (\omega^2 - \omega_{pe}^2)^2 \cos^2(\theta) \right]^{1/2}.$$

2.3 Ordinary (O) and Extraordinary (X) Mode

Evidently, eq. (2.20 AAH) has two modes. the solution with the $+$ sign in front of $\omega_{ce} \Delta$ is known as the *ordinary* (O) mode and is denoted N_O . Meanwhile, the solution with the $-$ sign is the *extraordinary* (X) mode and is denoted N_X .

2.3.1 Cutoffs and Resonances

To investigate the characteristics of the modes, I will first look for cutoffs. Cutoffs are defined by one of the equivalent conditions:

$$N \rightarrow 0 \quad \text{or} \quad \lambda = \frac{2\pi}{k} \rightarrow \infty \quad \text{or} \quad v_\phi = \frac{\omega}{k} \rightarrow \infty. \quad (2.21 \text{ cutoff})$$

A wave meeting a cutoff will be reflected and only an exponentially decaying part of it will be transmitted into the evanescent region (also called shadow region) behind the cutoff.

Importantly, cutoffs are caustics as can already be seen by comparing eq. (2.21 cutoff) with the eikonal criterion, eq. (1.2). Inspection of eq. (2.20 AAH) gives the following cutoffs (Ref. [3]):

$$N_O \rightarrow 0 \quad \text{when} \quad \omega = \omega_O = \omega_{pe} \quad (2.22)$$

$$N_X \rightarrow 0 \quad \text{when} \quad \omega = \omega_R = \left(\frac{\omega_{ce}^2}{4} + \omega_{pe}^2 \right)^{1/2} + \frac{\omega_{ce}}{2} \quad (2.23)$$

$$N_X \rightarrow 0 \quad \text{when} \quad \omega = \omega_L = \left(\frac{\omega_{ce}^2}{4} + \omega_{pe}^2 \right)^{1/2} - \frac{\omega_{ce}}{2}. \quad (2.24)$$

The cutoffs are known as the O, R and L cutoffs respectively. As the simplest cutoff the O-cutoff plays a main character in the example of Airy's equation which I present later. Physically it implies that an O-mode wave of frequency ω will be reflected when it reaches a density higher than the critical density where $\omega = \omega_{pe}$.

Resonances are locations of maximal absorption defined by the opposite condition of a cutoff:

$$N \rightarrow \infty \quad \text{or} \quad \lambda = \frac{2\pi}{k} \rightarrow 0 \quad \text{or} \quad v_\phi = \frac{\omega}{k} \rightarrow 0. \quad (2.25 \text{ resonance})$$

From eq. (2.20 AAH) it can be shown that (Ref. [3]):

$$N^2 \rightarrow \infty \quad \text{when} \quad \frac{\omega_{pe}^2}{\omega^2} = \frac{\omega^2 - \omega_{ce}^2}{\omega^2 - \omega_{ce}^2 \cos^2(\theta)} \quad (2.26)$$

At $\theta = \pi/2$ the resonance frequency of eq. (2.26) is called the upper hybrid (UH) resonance frequency:

$$\omega_{UH} := \sqrt{\omega_{ce}^2 + \omega_{pe}^2}. \quad (2.27)$$

For any θ , I shall use $\tilde{\omega}_{UH}$ to denote the more general resonance frequency matching the condition of eq. (2.26).

2.3.2 Perpendicular and Parallel Solutions

Finally, as in Ref. [3] I will inspect two special cases. First, the case of propagation parallel to \mathbf{B}_0 such that $\theta = 0, N_\perp = 0$. This greatly simplifies the wave equation, eq. (2.18) to:

$$\text{if } \mathbf{k} \parallel \mathbf{B}_0 \text{ then:} \quad (2.28a)$$

$$N^2 = 1 - \frac{\omega_{pe}^2}{\omega^2 \pm \omega_{ce}} \quad \text{with} \quad \frac{\tilde{E}_1}{\tilde{E}_2} = \pm i, \quad \tilde{E}_3 = 0 \quad (2.28b)$$

The solution with a + sign is the L mode and the solution with a - sign is the R mode (also called whistler mode, see Ref. [1]). The right equation in eq. (2.28b) shows that the R-mode is right circular polarized, while the L-mode is left circular polarized.

Next, consider the case of propagation perpendicular to \mathbf{B}_0 such that $\theta = \pi/2, N_\parallel = 0$. the wave equation, eq. (2.18) then gives (Refs. [3, 1]):

$$\text{if } \mathbf{k} \perp \mathbf{B}_0 \text{ then:} \quad (2.29a)$$

$$N_O^2 = 1 - \frac{\omega_{pe}^2}{\omega^2} \quad \text{with} \quad \tilde{E}_1 = \tilde{E}_2 = 0 \quad (2.29b)$$

$$N_X^2 = 1 - \frac{\omega_{pe}^2}{\omega^2} \frac{\omega^2 - \omega_{pe}^2}{\omega^2 - \omega_{UH}^2} \quad \text{with} \quad \frac{\tilde{E}_1}{\tilde{E}_2} = -i \frac{1}{\omega} \frac{\omega^2 - \omega_{UH}^2}{\omega_{pe}^2 \omega_{ce}}. \quad (2.29c)$$

This shows that an O-mode is linearly polarized with \mathbf{E} and \mathbf{B} parallel while the X-mode is elliptically polarized.

2.3.3 CMA Diagram

To get an overview of the AAH dispersion relation I have shown the two plots on fig. 2.2. Figure 2.2 (a) shows the dispersion relation for the case $\theta = \pi/2$, i.e. the graphs of eq. (2.29). I have plotted N^2 vs. ω_{pe}^2/ω^2 such that moving right in the plot takes you deeper into the plasma and moving up decreases the wavelength. The dashed lines show the solutions for the O-mode and X-mode respectively. For instance, the O-mode is seen to be linear on this plot, as one would expect from eq. (2.29b). Furthermore I have also shown the positions of the R, O, L cutoffs (dashed lines) and the UH resonance (solid line). The evanescent region where $N^2 < 0$ has been colored gray to indicate that it is a region of no propagation. It is clear from the plot, how the cutoffs coincides with the locations where the dispersion relation crosses $N = 0$. Similarly, N is seen to diverge at the UH resonance within the cold plasma model.

Next, on fig. 2.2 b) I present the Clemmow-Mullay-Allis (CMA) diagram which is a standard way to represent cold plasma waves. On a CMA diagram I plot ω_{ce}/ω vs. ω_{pe}^2/ω^2 . In other words, the lower left corner is the high frequency regime and the upper right corner is the low frequency regime. The y axis is proportional to the strength of the magnetic field, while the x axis is proportional to the density. So again, moving right takes you deeper into the plasma while moving up takes you to regions of higher magnetic field strength.

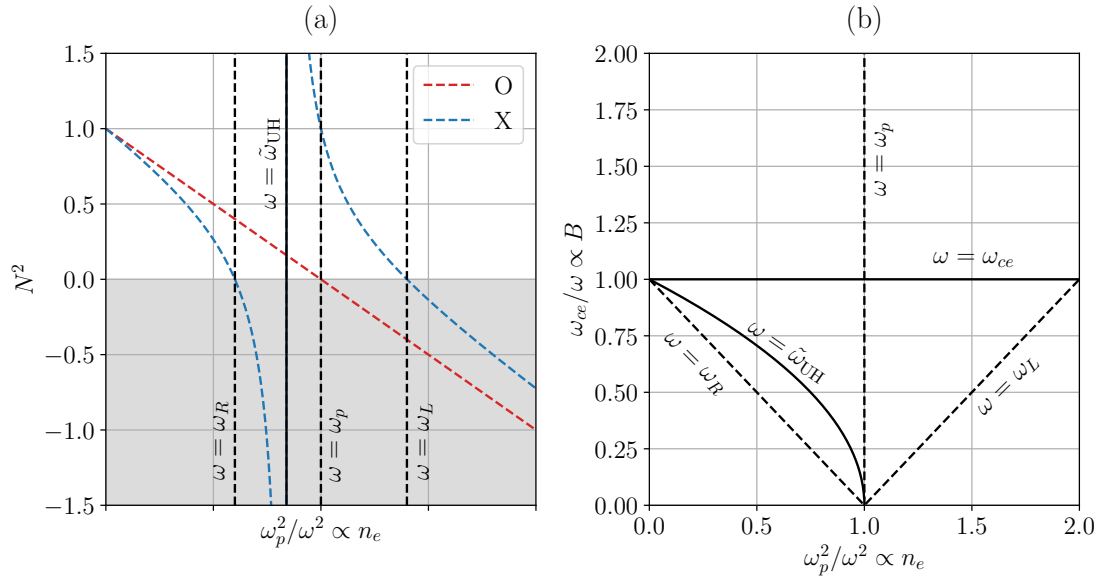


Figure 2.2: (a) Illustration of the AAH dispersion relation, eq. (2.20 AAH), for perpendicular propagation $\theta = 90^\circ$ to the magnetic field. The dashed lines are solutions of the dispersion relation in the special case of perpendicular propagation, eq. (2.29). The solid vertical line is the location of the upper hybrid resonance ($N \rightarrow \infty$) in the plasma. The vertical dashed lines are the locations of the O, R and L cutoffs ($N \rightarrow 0$). The gray region marks the evanescent region of no propagation. (b) CMA diagram with ω_{ce}/ω plotted vs. ω_{pe}^2/ω^2 . The x axis is proportional to the plasma density, while the y -axis is proportional to the B -field. As on (a) the solid lines marks the resonances whereas the dashed lines marks cutoffs.

3 Mathematical Foundation of Phase Space Analysis

Mathematics is the art of giving the same name to different things.

Henri Poincaré

In this chapter I give a resume of important mathematical prerequisites behind the modern formulation of GO. The wave field analysis studied in this thesis rests among other things upon the foundation of rigged Hilbert spaces and the Weyl symbol calculus.

3.1 The Hilbert Space

As is common in physics, by the Hilbert space \mathcal{H} , I specifically mean the $L^2(\mathbb{R}^N)$ space of square-integrable functions. That is, any two functions $\psi_1, \psi_2 \in \mathcal{H}$ will have a well-defined finite inner product given by¹:

$$\langle \psi_1 | \psi_2 \rangle := \int d\mathbf{x} \psi_1^*(\mathbf{x}) \psi_2(\mathbf{x}), \quad (3.1)$$

where the asterix denotes complex conjugation, $\mathbf{x} \in \mathbb{R}^N$ and N is the number of dimensions. The Hilbert space is equipped with the L^2 norm:

$$\|\psi\|_{L^2} := \sqrt{\langle \psi | \psi \rangle}. \quad (3.2) \quad (\|\cdot\|_{L^2})$$

An operator, $\hat{A} : \mathcal{H} \rightarrow \mathcal{H}$, map functions in the Hilbert space to other functions in the Hilbert space and can be defined by its' kernel function $A(\mathbf{x}, \mathbf{x}')$ as follows [4]:

$$\hat{A}\psi(\mathbf{x}) := \int d\mathbf{x}' A(\mathbf{x}, \mathbf{x}') \psi(\mathbf{x}'). \quad (3.3)$$

The adjoint operator \hat{A}^\dagger of \hat{A} satisfies:

$$\langle \hat{A}\psi_1 | \psi_2 \rangle = \langle \psi_1 | \hat{A}^\dagger \psi_2 \rangle, \quad \forall \psi_1, \psi_2 \in \mathcal{H}. \quad (3.4)$$

Hermitian operators (sometimes called self-adjoint) are defined by satisfying $\hat{A} = \hat{A}^\dagger$. Unitary operators are defined by satisfying $\hat{U}\hat{U}^\dagger = \hat{U}^\dagger\hat{U} = \hat{\mathbb{1}}$ where $\hat{\mathbb{1}}$ is the identity operator. For a given $\psi \in \mathcal{H}$, the family of unitarily transformed functions $\{\hat{U}\psi\}$ will be isomorphically equivalent and may therefore be regarded as the same state vector $|\psi\rangle \in \mathcal{H}$ (Ref. [4]). I use Dirac's bracket notation in which a vector in \mathcal{H} is denoted with a ket. The Hilbert space \mathcal{H} has a corresponding dual space of linear functionals on \mathcal{H} . Riesz' representation theorem guarantees that there is a one-to-one correspondence between linear functionals on \mathcal{H} and state vectors in \mathcal{H} (see Refs. [16, 17]). It is therefore meaningful to use the bra notation, $\langle \psi_1 |$, to denote the functional $\langle \psi_1 | : \mathcal{H} \rightarrow \mathbb{C}$ which is defined to take the inner product with the vector it acts upon:

$$\langle \psi_1 | | \psi_2 \rangle := \langle \psi_1 | \psi_2 \rangle. \quad (3.5)$$

¹The inner product is linear in the second component as is customary in physics rather than in the first component as is customary in mathematics.

In other words, $\langle \psi_1 |$ is an instruction to take the inner product of whatever comes to the right of it. If $|\psi_1\rangle$ has unit norm, i.e. $\langle \psi_1 | \psi_1 \rangle = 1$, then eq. (3.5) gives the projection of $|\psi_2\rangle$ onto $\langle \psi_1 |$. By this logic $|\psi_1\rangle \langle \psi_1 |$ is a projection operator.

A practical issue of the Hilbert space is that it does not include the Dirac delta function $\delta(\mathbf{x})$ (which is really a distribution and not a function, see Ref. [18, Ch. 1]) nor the plane wave function $e^{i\mathbf{k}\cdot\mathbf{x}}$ which is the eigenfunction of the differential operator $i\partial_{\mathbf{x}}$. To resolve this it is attractive instead to work with the extended rigged Hilbert space². The interested reader may study the mathematical technicalities in Ref. [17, Ch. 1], but for our purposes it is sufficient to note that these functions are included in the extended Hilbert space. From this point forward I take it to be implicit that all functions encountered live in the universe of the extended Hilbert space.

3.1.1 Position and Momentum Operator

Two operators are of particular importance: The position operator $\hat{\mathbf{x}} = (\hat{x}_1, \dots, \hat{x}_N)^T$ and the momentum operator $\hat{\mathbf{k}} = (\hat{k}_1, \dots, \hat{k}_N)^T$. The position operator, \hat{x}_i , is defined to satisfy $\hat{x}_i \psi(\mathbf{x}) = x_i \psi(\mathbf{x})$ for all ψ . The eigenstate of the position operator $\hat{\mathbf{x}}$ with eigenvalue \mathbf{x}_0 is the Dirac delta function:

$$\hat{\mathbf{x}} \delta(\mathbf{x} - \mathbf{x}_0) = \mathbf{x} \delta(\mathbf{x} - \mathbf{x}_0) = \mathbf{x}_0 \delta(\mathbf{x} - \mathbf{x}_0) \quad (3.6)$$

In Dirac's notation the eigenfunction of $\hat{\mathbf{x}}$ is written $|\mathbf{x}_0\rangle$. That is

$$\hat{\mathbf{x}} |\mathbf{x}_0\rangle = \mathbf{x}_0 |\mathbf{x}_0\rangle. \quad (3.7)$$

By the definition of the delta-function and the definition of the bra in eq. (3.5) the dual functional of the eigenvector $|\mathbf{x}_0\rangle$ must be defined by:

$$\langle \mathbf{x}_0 | \psi \rangle = \int d\mathbf{x}' \delta(\mathbf{x}' - \mathbf{x}_0) \psi(\mathbf{x}') = \psi(\mathbf{x}_0). \quad (3.8)$$

Therefore $\psi(\mathbf{x})$ may be perceived as the projection of the state $|\psi\rangle$ onto the position basis $|\mathbf{x}\rangle$ and we may call $\psi(\mathbf{x})$ the position representation of $|\psi\rangle$. Importantly, the preceding analysis also shows that $|\mathbf{x}\rangle$ is an orthonormal basis (ONB) in the continuous sense:

$$\langle \mathbf{x} | \mathbf{x}' \rangle = \delta(\mathbf{x} - \mathbf{x}') \quad \text{or} \quad \int d\mathbf{x} |\mathbf{x}\rangle \langle \mathbf{x}| = \hat{\mathbb{1}}. \quad (3.9)$$

Similar to the position representation of states, the function $A(\mathbf{x}, \mathbf{x}') = \langle \mathbf{x} | \hat{A} | \mathbf{x}' \rangle$ of eq. (3.3) is the position representation of the operator \hat{A} . In fact, operators only act directly on the state vectors $|\psi\rangle \in \mathcal{H}$, not on their position representations as in eq. (3.3). The operator \hat{A} should strictly be defined by:

$$\hat{A} := \int d\mathbf{x} \int d\mathbf{x}' |\mathbf{x}\rangle A(\mathbf{x}, \mathbf{x}') \langle \mathbf{x}'|. \quad (3.10)$$

However, the notation of eq. (3.3) is fully valid if I take it to mean:

$$\hat{A}\psi(\mathbf{x}) := \langle \mathbf{x} | \hat{A} | \psi \rangle, \quad (3.11)$$

in which case I end up with eq. (3.3). The trace of an operator is the sum of diagonal elements. For a continuous basis like the position-basis this looks like:

$$\text{Tr}[\hat{A}] = \int d\mathbf{x} \langle \mathbf{x} | A | \mathbf{x} \rangle = \int d\mathbf{x} A(\mathbf{x}, \mathbf{x}). \quad (3.12 \text{ Tr})$$

²In this context *rigged* should be understood as "ready to be applied", see Ref. [17, p. 28].

If the trace of the product of two operators is finite, we may define the Hilbert-Schmidt inner product between the operators as:

$$\langle \hat{A}, \hat{B} \rangle_{\text{HS}} = \text{Tr}[\hat{A}^\dagger \hat{B}] \quad (3.13)$$

The norm induced from this is the Hilbert-Schmidt norm:

$$\|\hat{A}\|_{\text{HS}} := \sqrt{\text{Tr}[\hat{A}^\dagger \hat{A}]} \quad (3.14 \ \|\cdot\|_{\text{HS}})$$

The momentum operator $\hat{\mathbf{k}} = (\hat{k}_1, \dots, \hat{k}_N)^T$ can be defined by its' position representation which is $-i\partial_{\mathbf{x}}$. Formally,

$$\hat{k}_i := \int d\mathbf{x}' |\mathbf{x}'\rangle (-i\partial_{x'_i}) \langle \mathbf{x}'| \quad \text{or} \quad (3.15a)$$

$$\hat{\mathbf{k}} := \int d\mathbf{x}' |\mathbf{x}'\rangle (-i\partial_{\mathbf{x}'}) \langle \mathbf{x}'|. \quad (3.15b)$$

In effect, the momentum operator takes the gradient of the function to the right of it:

$$\hat{\mathbf{k}}\psi(\mathbf{x}) := \langle \mathbf{x} | \int d\mathbf{x}' |\mathbf{x}'\rangle (-i\partial_{\mathbf{x}'}) \langle \mathbf{x}' | \psi \rangle = \int d\mathbf{x}' \delta(\mathbf{x} - \mathbf{x}') (-i\partial_{\mathbf{x}'}) \psi(\mathbf{x}') = -i\partial_{\mathbf{x}}\psi(\mathbf{x}). \quad (3.16)$$

The position and momentum operator satisfy the canonical commutation relation:

$$[\hat{x}_i, \hat{k}_j] := \hat{x}_i \hat{k}_j - \hat{k}_j \hat{x}_i = i\delta_{ij}, \quad (3.17)$$

where δ_{ij} is Kroenecker's delta. The commutation relation is straightforward to prove by simply applying the commutator $[\hat{x}_i, \hat{k}_j]$ to a $\psi(\mathbf{x})$. The eigenstate of the momentum operator has the position representation of a plane wave function $a e^{i\mathbf{k}\cdot\mathbf{x}}$, $a \in \mathbb{C}$ as can easily be checked from its' definition, eq. (3.15):

$$\hat{k}(a e^{i\mathbf{k}\cdot\mathbf{x}}) = -i\partial_{\mathbf{x}}(a e^{i\mathbf{k}\cdot\mathbf{x}}) = \mathbf{k}(a e^{i\mathbf{k}\cdot\mathbf{x}}). \quad (3.18)$$

The momentum eigenstate $|\mathbf{k}\rangle$ can be unit normalized by setting $a := (2\pi)^{-N/2}$, but it is customary instead to set $a = 1$ (see e.g. Ref. [14]) which then imply the normalization:

$$\langle \mathbf{k} | \mathbf{k}' \rangle = \int d\mathbf{x} e^{i\mathbf{x}\cdot(\mathbf{k}'-\mathbf{k})} = (2\pi)^N \delta(\mathbf{k}' - \mathbf{k}), \quad \text{or} \quad \int \frac{d\mathbf{k}}{(2\pi)^N} |\mathbf{k}\rangle \langle \mathbf{k}| = \hat{\mathbb{1}}. \quad (3.19)$$

where I used one of the possible definitions of the delta-function, Ref. [18, p. 77]. Finally, the momentum representation of the position operator $\hat{\mathbf{x}}$ is $i\partial_{\mathbf{k}}$ as can for instance be proven by insertion of the identities of eqs. (3.9) and (3.19):

$$\begin{aligned} \hat{\mathbf{x}} &= \int \frac{d\mathbf{k}}{(2\pi)^N} |\mathbf{k}\rangle \langle \mathbf{k}| \int d\mathbf{x} |\mathbf{x}\rangle \langle \mathbf{x}| \hat{\mathbf{x}} = \int \frac{d\mathbf{k}}{(2\pi)^N} \int d\mathbf{x} |\mathbf{k}\rangle \mathbf{x} e^{-i\mathbf{k}\cdot\mathbf{x}} \langle \mathbf{x}| \\ &= \int \frac{d\mathbf{k}}{(2\pi)^N} |\mathbf{k}\rangle (i\partial_{\mathbf{k}}) \left\{ \int d\mathbf{x} \langle \mathbf{k} | \mathbf{x} \rangle \langle \mathbf{x} | \right\} = \int \frac{d\mathbf{k}}{(2\pi)^N} |\mathbf{k}\rangle (i\partial_{\mathbf{k}}) \langle \mathbf{k}|. \end{aligned}$$

In summary, I have the following relations:

$$\hat{\mathbf{x}} = \int d\mathbf{x}' |\mathbf{x}'\rangle \mathbf{x}' \langle \mathbf{x}'|, \quad \hat{\mathbf{k}} = \int d\mathbf{x}' |\mathbf{x}'\rangle (-i\partial_{\mathbf{x}'}) \langle \mathbf{x}'| \quad (3.20a)$$

$$\hat{\mathbf{x}} = \int \frac{d\mathbf{k}'}{(2\pi)^N} |\mathbf{k}'\rangle (i\partial_{\mathbf{k}'}) \langle \mathbf{k}'|, \quad \hat{\mathbf{k}} = \int \frac{d\mathbf{k}'}{(2\pi)^N} |\mathbf{k}'\rangle \mathbf{k}' \langle \mathbf{k}'| \quad (3.20b)$$

$$\hat{\mathbf{x}} |\mathbf{x}\rangle = \mathbf{x} |\mathbf{x}\rangle, \quad \hat{\mathbf{k}} |\mathbf{k}\rangle = \mathbf{k} |\mathbf{k}\rangle \quad (3.20c)$$

$$[x_i, k_j] = i\delta_{ij}, \quad [k_i, x_j] = -i\delta_{ij} \quad (3.20d)$$

$$\hat{\mathbb{1}} = \int d\mathbf{x} |\mathbf{x}\rangle \langle \mathbf{x}|, \quad \hat{\mathbb{1}} = \int \frac{d\mathbf{k}}{(2\pi)^N} |\mathbf{k}\rangle \langle \mathbf{k}| \quad (3.20e)$$

$$\langle \mathbf{x} | \mathbf{k} \rangle = e^{i\mathbf{k} \cdot \mathbf{x}}, \quad \langle \mathbf{k} | \mathbf{x} \rangle = e^{-i\mathbf{k} \cdot \mathbf{x}}. \quad (3.20f)$$

3.1.2 Fourier Transforms

The Dirac bracket notation makes it elegant to express the Fourier transform of a field $\psi(\mathbf{x})$. By definition, the Fourier transform $\mathcal{F}\{\psi(\mathbf{x})\}$ of $\psi(\mathbf{x})$ is found as the momentum representation of $|\psi\rangle$ and conversely the inverse transform is defined as the position representation. That is:

$$\tilde{\psi}(\mathbf{k}) := \mathcal{F}(\psi(\mathbf{x})) := \langle \mathbf{k} | \psi \rangle = \int d\mathbf{x} \langle \mathbf{k} | \mathbf{x} \rangle \langle \mathbf{x} | \psi \rangle = \int d\mathbf{x} e^{-\mathbf{k} \cdot \mathbf{x}} \psi(\mathbf{x}) \quad (3.21 \text{ FT})$$

$$\psi(\mathbf{x}) := \mathcal{F}^{-1}(\tilde{\psi}(\mathbf{k})) := \langle \mathbf{x} | \psi \rangle = \int \frac{d\mathbf{k}}{(2\pi)^N} \langle \mathbf{x} | \mathbf{k} \rangle \langle \mathbf{k} | \psi \rangle = \int \frac{d\mathbf{k}}{(2\pi)^N} e^{i\mathbf{k} \cdot \mathbf{x}} \tilde{\psi}(\mathbf{k}) \quad (3.22 \text{ Inv. FT})$$

As is done above, when using the Fourier transformed field I often decorate it with a tilde to make explicit that it is the momentum representation of $|\psi\rangle$ I am dealing with. The interpretation of the Fourier transform as a projection onto \mathbf{k} -space will become important later where I shall introduce the more generalized metaplectic transform.

In complete analogy with eq. (3.21 FT), I define the Fourier transforms between the time and frequency domains as:

$$\tilde{\psi}(\omega) = \int dt \psi(t) e^{i\omega t} \quad (3.23)$$

$$\psi(t) = \int \frac{d\omega}{2\pi} \tilde{\psi}(\omega) e^{-i\omega t}. \quad (3.24)$$

The Fourier transform in time has a similar interpretation as its' spatial counterpart, but with $-t$ playing the role of \mathbf{x} .

3.2 Weyl Symbol Calculus

The three-dimensional physical space which we all inhabit can mathematically be described as the continuous spectrum \mathbf{x} of the position operator $\hat{\mathbf{x}}$. In a similar manner, the momentum operator has an associated \mathbf{k} -space. While it may feel most natural to represent wave equations such as Maxwell's equations in the position space, the previous discussion on the Hilbert space formalism suggests that it is really the field state vector $|\psi\rangle$ and the operator \hat{A} and not their position representations $\psi(\mathbf{x}), A(\mathbf{x}, \mathbf{x}')$ which are the central objects. The Fourier transformations of eqs. (3.21 FT) and (3.22 Inv. FT) expose the arbitrariness in projecting the physical fields onto \mathbf{x} -space. In modern wave theory, \mathbf{x} and \mathbf{k} space is instead treated on an equal footing by describing the physical

laws in phase space $\mathbf{z} = (\mathbf{x}, \mathbf{k})^T$. To do this, we need a systematic theory for representing operators in phase space. This theory is provided by Weyl's Symbol calculus. Though originally developed for quantum mechanics, the methodology is highly applicable for all wave phenomena alike [5]. The following section is based on Refs. [4, 19, 5, 7]. Please refer to Ref. [19] for a generalization to curvilinear coordinates.

3.2.1 Symplectic Phase Space Translations

Weyl's symbol calculus provides a one-to-one transformation from operators to functions of phase space coordinates. The central trick of this *Wigner-Weyl transform* which I shall define shortly is to decompose any operator into an expansion of translations in phase space. Let $\zeta = (\xi, \kappa)^T$ be a pair of phase space coordinates and consider the operators (note that $\hat{\mathbf{x}}, \hat{\mathbf{k}}$ in the exponents are operators):

$$\hat{T}_\xi := e^{-i\xi \cdot \hat{\mathbf{k}}} = \int d\mathbf{x}' |\mathbf{x}'\rangle \langle \mathbf{x}' - \xi| \quad \text{and} \quad \hat{T}_\kappa := e^{i\kappa \cdot \hat{\mathbf{x}}} = \int \frac{d\mathbf{k}'}{(2\pi)^N} |\mathbf{k}'\rangle \langle \mathbf{k}' - \kappa|. \quad (3.25)$$

As indicated, \hat{T}_ξ translates in position space, whereas \hat{T}_κ translates in momentum space (in other words \hat{T}_κ modulates). That is: $\hat{T}_\xi \psi(\mathbf{x}) = \psi(\mathbf{x} - \xi)$. To see this, use eqs. (3.20c), (3.20e) and (3.20f). For instance for the position space translation:

$$e^{-i\xi \cdot \hat{\mathbf{k}}} = \int d\mathbf{x} \int \frac{d\mathbf{k}}{(2\pi)^N} |\mathbf{x}\rangle \langle \mathbf{x}| \mathbf{k} \rangle \langle \mathbf{k}| e^{-i\xi \cdot \hat{\mathbf{k}}} = \int d\mathbf{x} \int \frac{d\mathbf{k}}{(2\pi)^N} |\mathbf{x}\rangle e^{i\mathbf{x} \cdot \mathbf{k}} e^{-i\xi \cdot \mathbf{k}} \langle \mathbf{k}| \quad (3.26)$$

$$= \int d\mathbf{x} \int \frac{d\mathbf{k}}{(2\pi)^N} |\mathbf{x}\rangle \langle \mathbf{x} - \xi| \mathbf{k} \rangle \langle \mathbf{k}| = \int d\mathbf{x} |\mathbf{x}\rangle \langle \mathbf{x} - \xi|. \quad (3.27)$$

Note that $\hat{T}_\xi^\dagger = \hat{T}_{-\xi}$, $\hat{T}_\kappa^\dagger = \hat{T}_{-\kappa}$.

Now, let me introduce the symplectic matrix J_{2N} :

$$J_{2N} := \begin{pmatrix} \mathbf{0}_N & \mathbf{I}_N \\ -\mathbf{I}_N & \mathbf{0}_N \end{pmatrix}, \quad (3.28)$$

where $\mathbf{0}_N$ is an $N \times N$ zero-matrix and \mathbf{I}_N is the $N \times N$ identity. J_{2N} allows me to define the bilinear symplectic product, $\zeta \wedge \mathbf{z}$, between two phase space coordinates, $\zeta = (\xi, \kappa)^T$ and $\mathbf{z} = (\mathbf{x}, \mathbf{k})^T$ (see e.g. Refs. [5, 19]³):

$$\zeta \wedge \mathbf{z} := \zeta^T J_{2N} \mathbf{z} = \xi \cdot \mathbf{k} - \kappa \cdot \mathbf{x}. \quad (3.29)$$

With the symplectic product, I may define the *Heisenberg generating operator*, which performs a symplectic phase space translation:

$$\hat{T}_\zeta := e^{i\zeta \wedge \hat{\mathbf{z}}} = e^{i(\xi \cdot \hat{\mathbf{k}} - \kappa \cdot \hat{\mathbf{x}})}. \quad (3.30)$$

\hat{T}_ζ should be evaluated with care, since $\hat{\mathbf{x}}$ and $\hat{\mathbf{k}}$ does not commute as indicated by eq. (3.20d). In a case like this where two operators, \hat{A}, \hat{B} , commute with their commutator, $[\hat{A}, \hat{B}]$, we can use the Campbell-Baker-Hausdorff theorem (see Ref. [6, p. 121] or [17, p. 95]):

$$\begin{aligned} \text{if } [\hat{A}, [\hat{A}, \hat{B}]] = [\hat{B}, [\hat{A}, \hat{B}]] = 0 \quad \text{then:} \\ e^{\hat{A} + \hat{B}} = e^{\hat{A}} e^{\hat{B}} e^{-\frac{1}{2}[\hat{A}, \hat{B}]} = e^{\hat{B}} e^{\hat{A}} e^{\frac{1}{2}[\hat{A}, \hat{B}]} \end{aligned} \quad (3.31 \text{ CBH})$$

³Note, that my sign of the symplectic product is the same as used in Ref. [5], but opposite to the sign used in Ref. [19]

Using this on eq. (3.30) together with the canonical commutation relation of eq. (3.20d) gives:

$$\hat{T}_\zeta = e^{i\zeta \wedge \hat{\mathbf{z}}} = e^{i\boldsymbol{\xi} \cdot \hat{\mathbf{k}}} e^{-i\boldsymbol{\kappa} \cdot \hat{\mathbf{x}}} e^{\frac{i}{2}\boldsymbol{\xi} \cdot \boldsymbol{\kappa}} = e^{-i\boldsymbol{\kappa} \cdot \hat{\mathbf{x}}} e^{i\boldsymbol{\xi} \cdot \hat{\mathbf{k}}} e^{-\frac{i}{2}\boldsymbol{\xi} \cdot \boldsymbol{\kappa}} \quad (3.32)$$

$$= \hat{T}_{-\boldsymbol{\xi}} \hat{T}_{-\boldsymbol{\kappa}} e^{\frac{i}{2}\boldsymbol{\xi} \cdot \boldsymbol{\kappa}} = \hat{T}_{-\boldsymbol{\kappa}} \hat{T}_{-\boldsymbol{\xi}} e^{-\frac{i}{2}\boldsymbol{\xi} \cdot \boldsymbol{\kappa}}. \quad (3.33)$$

Note that $\hat{T}_\zeta^\dagger = \hat{T}_{-\boldsymbol{\zeta}}$.

Using eq. (3.33) together with eq. (3.25) and eq. (3.20f), the Heisenberg generating operator can also be written as:

$$\hat{T}_\zeta = e^{i\zeta \wedge \hat{\mathbf{z}}} = \int d\mathbf{x}' e^{-i\boldsymbol{\kappa} \cdot \hat{\mathbf{x}}} |\mathbf{x}'\rangle \langle \mathbf{x}' + \boldsymbol{\xi}| e^{-\frac{i}{2}\boldsymbol{\xi} \cdot \boldsymbol{\kappa}} = \int d\mathbf{x}' |\mathbf{x}'\rangle \left\langle \boldsymbol{\kappa} \left| \mathbf{x}' + \frac{\boldsymbol{\xi}}{2} \right. \right\rangle \langle \mathbf{x}' + \boldsymbol{\xi}|. \quad (3.34)$$

The trace, eq. (3.12 Tr), of the Heisenberg operator is:

$$\text{Tr}[\hat{T}_\zeta] = \int d\mathbf{x} \int d\mathbf{x}' \langle \mathbf{x} | \mathbf{x}' \rangle \left\langle \boldsymbol{\kappa} \left| \mathbf{x}' + \frac{\boldsymbol{\xi}}{2} \right. \right\rangle \langle \mathbf{x}' + \boldsymbol{\xi} | \mathbf{x} \rangle = \delta(\boldsymbol{\xi}) \int d\mathbf{x} e^{i(\boldsymbol{\kappa} \cdot \mathbf{x})} = (2\pi)^N \delta(\boldsymbol{\zeta}). \quad (3.35)$$

3.2.2 Wigner Operator

Before defining the Wigner-Weyl transform, let me introduce the Wigner operator defined as the phase space Fourier transform of the Heisenberg generating operator (Ref. [19]):

$$\hat{\Delta}_{\mathbf{z}} := \int \frac{d\boldsymbol{\zeta}}{(2\pi)^N} e^{-i\zeta \wedge \mathbf{z}} \hat{T}_\zeta = \int \frac{d\boldsymbol{\zeta}}{(2\pi)^N} e^{-i\zeta \wedge (\mathbf{z} - \hat{\mathbf{z}})} = \int d\boldsymbol{\xi} e^{-i\boldsymbol{\xi} \cdot \mathbf{k}} \left| \mathbf{x} - \frac{\boldsymbol{\xi}}{2} \right\rangle \left\langle \mathbf{x} + \frac{\boldsymbol{\xi}}{2} \right|. \quad (3.36 \hat{\Delta}_{\mathbf{z}})$$

To show the last equality, I use eq. (3.34):

$$\begin{aligned} \hat{\Delta}_{\mathbf{z}} &= \int d\boldsymbol{\xi} \int \frac{\boldsymbol{\kappa}}{(2\pi)^N} e^{-i(\boldsymbol{\xi} \cdot \mathbf{k} - \boldsymbol{\kappa} \cdot \mathbf{x})} \hat{T}_\zeta \\ &= \int d\boldsymbol{\xi} e^{-i\boldsymbol{\xi} \cdot \mathbf{k}} \int \frac{\boldsymbol{\kappa}}{(2\pi)^N} \langle \mathbf{x} | \boldsymbol{\kappa} \rangle \left[\int d\mathbf{x}' |\mathbf{x}'\rangle \left\langle \boldsymbol{\kappa} \left| \mathbf{x}' + \frac{\boldsymbol{\xi}}{2} \right. \right\rangle \langle \mathbf{x}' + \boldsymbol{\xi}| \right] \\ &= \int d\boldsymbol{\xi} e^{-i\boldsymbol{\xi} \cdot \mathbf{k}} \int d\mathbf{x}' |\mathbf{x}'\rangle \langle \mathbf{x}| \left(\int \frac{\boldsymbol{\kappa}}{(2\pi)^N} |\boldsymbol{\kappa}\rangle \langle \boldsymbol{\kappa}| \right) \left| \mathbf{x}' + \frac{\boldsymbol{\xi}}{2} \right\rangle \langle \mathbf{x}' + \boldsymbol{\xi}| \\ &= \int d\boldsymbol{\xi} e^{-i\boldsymbol{\xi} \cdot \mathbf{k}} \int d\mathbf{x}' |\mathbf{x}'\rangle \left\langle \mathbf{x} \left| \mathbf{x}' + \frac{\boldsymbol{\xi}}{2} \right. \right\rangle \langle \mathbf{x}' + \boldsymbol{\xi}| \\ &= \int d\boldsymbol{\xi} e^{-i\boldsymbol{\xi} \cdot \mathbf{k}} \left| \mathbf{x} - \frac{\boldsymbol{\xi}}{2} \right\rangle \left\langle \mathbf{x} + \frac{\boldsymbol{\xi}}{2} \right|. \end{aligned}$$

Note that the Wigner operator is hermitian, $\hat{\Delta}_{\mathbf{z}}^\dagger = \hat{\Delta}_{\mathbf{z}}$. This together with eq. (3.35) shows that Wigner operators are Hilbert-Schmidt orthogonal (Ref. [19]):

$$\begin{aligned} \langle \hat{\Delta}_{\mathbf{z}}, \hat{\Delta}_{\mathbf{z}'} \rangle_{\text{HS}} &= \text{Tr}[\hat{\Delta}_{\mathbf{z}} \hat{\Delta}_{\mathbf{z}'}] = \int \frac{d\boldsymbol{\zeta}}{(2\pi)^N} \int \frac{d\boldsymbol{\zeta}'}{(2\pi)^N} e^{-i\zeta \wedge \mathbf{z}} e^{-i\zeta' \wedge \mathbf{z}'} \text{Tr}[\hat{T}_\zeta \hat{T}_{\zeta'}] \\ &= \int \frac{d\boldsymbol{\zeta} d\boldsymbol{\zeta}'}{(2\pi)^{2N}} e^{-i(\zeta \wedge \mathbf{z} + i\zeta' \wedge \mathbf{z}')} \text{Tr}[\hat{T}_{\zeta+\zeta'}] \\ &= \int \frac{d\boldsymbol{\zeta} d\boldsymbol{\zeta}'}{(2\pi)^N} e^{-i(\zeta \wedge \mathbf{z} + i\zeta' \wedge \mathbf{z}')} \delta(\boldsymbol{\zeta} + \boldsymbol{\zeta}') \\ &= \int \frac{d\boldsymbol{\zeta}}{(2\pi)^N} e^{-i\zeta \wedge (\mathbf{z} - \mathbf{z}')} \\ &= (2\pi)^N \delta(\mathbf{z} - \mathbf{z'}). \end{aligned} \quad (3.37)$$

3.2.3 Wigner-Weyl Transform ($\hat{A} \mapsto \mathcal{A}(\mathbf{z})$)

I am now finally ready to define the Wigner-Weyl transform $\mathbb{W}_{\mathbf{z}}$ which maps an operator \hat{A} to a function $\mathcal{A}(\mathbf{z})$ of phase space coordinates $\mathbf{z} = (\mathbf{x}, \mathbf{k})^T \in \mathbb{R}^{2N}$. Its' definition is:

$$\mathcal{A}(\mathbf{z}) := \mathbb{W}_{\mathbf{z}}[\hat{A}] := \text{Tr}[\hat{\Delta}_{\mathbf{z}} \hat{A}] \quad (3.38)$$

Here Tr denotes the trace defined in eq. (3.12 Tr) and $\hat{\Delta}_{\mathbf{z}}$ is the Wigner operator of eq. (3.36 $\hat{\Delta}_{\mathbf{z}}$). The function $\mathcal{A}(\mathbf{z})$ is known as the *Weyl Symbol* and I shall consistently write it in calligraphic letters. Using eq. (3.36 $\hat{\Delta}_{\mathbf{z}}$) the Wigner-Weyl transform may be written:

$$\mathcal{A}(\mathbf{z}) = \mathbb{W}_{\mathbf{z}}[\hat{A}] = \int d\mathbf{x}' \langle \mathbf{x}' | \hat{\Delta}_{\mathbf{z}} \hat{A} | \mathbf{x}' \rangle = \int d\boldsymbol{\xi} e^{-i\boldsymbol{\xi} \cdot \mathbf{k}} \left\langle \mathbf{x} + \frac{\boldsymbol{\xi}}{2} \middle| \hat{A} \middle| \mathbf{x} - \frac{\boldsymbol{\xi}}{2} \right\rangle. \quad (3.39 \mathbb{W}_{\mathbf{z}})$$

Note, in complete analogy with the above, the Wigner-Weyl transform may also be expressed as \mathbf{k} -basis matrix elements:

$$\mathbb{W}_{\mathbf{z}}[\hat{A}] = \int \frac{d\boldsymbol{\kappa}}{(2\pi)^N} e^{i\boldsymbol{\kappa} \cdot \mathbf{x}} \left\langle \mathbf{k} + \frac{\boldsymbol{\kappa}}{2} \middle| \hat{A} \middle| \mathbf{k} - \frac{\boldsymbol{\kappa}}{2} \right\rangle. \quad (3.40)$$

The Wigner-Weyl transform of an adjoint operator is simply the complex conjugated symbol:

$$\begin{aligned} \mathbb{W}_{\mathbf{z}}[\hat{A}^\dagger] &= \int d\boldsymbol{\xi} e^{-i\boldsymbol{\xi} \cdot \mathbf{k}} \left\langle \mathbf{x} + \frac{\boldsymbol{\xi}}{2} \middle| \hat{A}^\dagger \middle| \mathbf{x} - \frac{\boldsymbol{\xi}}{2} \right\rangle = \int d\boldsymbol{\xi} e^{-i\boldsymbol{\xi} \cdot \mathbf{k}} \left\langle \mathbf{x} - \frac{\boldsymbol{\xi}}{2} \middle| \hat{A} \middle| \mathbf{x} + \frac{\boldsymbol{\xi}}{2} \right\rangle^* \\ &= \int d\boldsymbol{\xi} e^{i\boldsymbol{\xi} \cdot \mathbf{k}} \left\langle \mathbf{x} + \frac{\boldsymbol{\xi}}{2} \middle| \hat{A} \middle| \mathbf{x} - \frac{\boldsymbol{\xi}}{2} \right\rangle^* = (\mathbb{W}_{\mathbf{z}}[\hat{A}])^* \end{aligned} \quad (3.41)$$

3.2.4 Inverse Wigner-Weyl Transform ($\mathcal{A}(\mathbf{z}) \mapsto \hat{A}$)

The inverse Wigner Weyl transform maps a symbol, $\mathcal{A}(\mathbf{z})$ (i.e. a function of phase space coordinates) to an operator \hat{A} :

$$\hat{A} = \mathbb{W}^{-1}[\mathcal{A}(\mathbf{z})] := \int \frac{d\mathbf{z}}{(2\pi)^N} \mathcal{A}(\mathbf{z}) \hat{\Delta}_{\mathbf{z}}. \quad (3.42 \mathbb{W}^{-1})$$

To show that this is in fact the inverse transform I use eq. (3.39 $\mathbb{W}_{\mathbf{z}}$) and eq. (3.36 $\hat{\Delta}_{\mathbf{z}}$):

$$\begin{aligned} \mathbb{W}^{-1}[\mathbb{W}_{\mathbf{z}}[\hat{A}]] &= \int \frac{d\mathbf{z}}{(2\pi)^N} \left(\int d\boldsymbol{\xi} e^{-i\boldsymbol{\xi} \cdot \mathbf{k}} \left\langle \mathbf{x} + \frac{\boldsymbol{\xi}}{2} \middle| \hat{A} \middle| \mathbf{x} - \frac{\boldsymbol{\xi}}{2} \right\rangle \right) \int d\boldsymbol{\xi}' e^{-i\boldsymbol{\xi}' \cdot \mathbf{k}} \left\langle \mathbf{x} - \frac{\boldsymbol{\xi}'}{2} \middle| \hat{\Delta}_{\mathbf{z}} \middle| \mathbf{x} + \frac{\boldsymbol{\xi}'}{2} \right\rangle \\ &= \int d\mathbf{x} \int d\boldsymbol{\xi} \int d\boldsymbol{\xi}' \left(\int \frac{d\mathbf{k}}{(2\pi)^N} e^{-i\mathbf{k} \cdot (\mathbf{x} + \boldsymbol{\xi}')} \right) \left\langle \mathbf{x} - \frac{\boldsymbol{\xi}'}{2} \middle| \hat{\Delta}_{\mathbf{z}} \middle| \mathbf{x} + \frac{\boldsymbol{\xi}'}{2} \right\rangle \left\langle \mathbf{x} + \frac{\boldsymbol{\xi}'}{2} \middle| \hat{A} \middle| \mathbf{x} - \frac{\boldsymbol{\xi}'}{2} \right\rangle \\ &= \int d\mathbf{x} \int d\boldsymbol{\xi} \int d\boldsymbol{\xi}' \delta(\boldsymbol{\xi} + \boldsymbol{\xi}') \left\langle \mathbf{x} - \frac{\boldsymbol{\xi}'}{2} \middle| \hat{A} \middle| \mathbf{x} - \frac{\boldsymbol{\xi}'}{2} \right\rangle \left\langle \mathbf{x} + \frac{\boldsymbol{\xi}'}{2} \middle| \hat{A} \middle| \mathbf{x} - \frac{\boldsymbol{\xi}'}{2} \right\rangle \\ &= \int d\mathbf{x} \int d\boldsymbol{\xi} \left\langle \mathbf{x} + \frac{\boldsymbol{\xi}}{2} \middle| \hat{A} \middle| \mathbf{x} - \frac{\boldsymbol{\xi}}{2} \right\rangle \left\langle \mathbf{x} - \frac{\boldsymbol{\xi}}{2} \middle| \hat{A} \middle| \mathbf{x} + \frac{\boldsymbol{\xi}}{2} \right\rangle \\ &= \int d\mathbf{x} \int d\boldsymbol{\xi} \left\langle \mathbf{x} + \frac{\boldsymbol{\xi}}{2} \middle| \hat{A} \middle| \mathbf{x} - \frac{\boldsymbol{\xi}}{2} \right\rangle \left\langle \mathbf{x} - \frac{\boldsymbol{\xi}}{2} \middle| \hat{A} \middle| \mathbf{x} + \frac{\boldsymbol{\xi}}{2} \right\rangle \\ &= \int d\mathbf{x} \int d\boldsymbol{\xi} \int d\mathbf{x}' \int d\mathbf{x}'' | \mathbf{x}' \rangle \left\langle \mathbf{x}' \middle| \mathbf{x} + \frac{\boldsymbol{\xi}}{2} \right\rangle \left\langle \mathbf{x} + \frac{\boldsymbol{\xi}}{2} \middle| \hat{A} \middle| \mathbf{x} - \frac{\boldsymbol{\xi}}{2} \right\rangle \left\langle \mathbf{x} - \frac{\boldsymbol{\xi}}{2} \middle| \mathbf{x}'' \right\rangle \langle \mathbf{x}'' | \\ &= \int d\mathbf{x}' \int d\mathbf{x}'' | \mathbf{x}' \rangle \langle \mathbf{x}' | \hat{A} | \mathbf{x}'' \rangle \langle \mathbf{x}'' | \\ &= \hat{A}. \end{aligned}$$

Conversely, It can be shown that $\mathbb{W}_z[\mathbb{W}^{-1}[\mathcal{A}(z)]] = \mathcal{A}(z)$. The invertibility of \mathbb{W}_z shows that \mathbb{W}_z is a bijection, that is a one-to-one correspondence, $\hat{A} \leftrightarrow \mathcal{A}(z)$, between operators and symbols. Importantly, the Wigner-Weyl transform and its' inverse has a number of desirable properties. First, eq. (3.41) shows that $\mathbb{W}_z, \mathbb{W}^{-1}$ preserves hermiticity in the sense:

$$\hat{A} = \hat{A}^\dagger \Leftrightarrow \mathcal{A}(z) \in \mathbb{R} \quad \forall z \in \mathbb{R}^{2N}. \quad (3.43)$$

Second, the transform is linear:

$$\mathbb{W}_z[\alpha \hat{A} + \beta \hat{B}] = \alpha \mathbb{W}_z[\hat{A}] + \beta \mathbb{W}_z[\hat{B}] \quad \text{and} \quad (3.44)$$

$$\mathbb{W}^{-1}[\alpha \mathcal{A}(z) + \beta \mathcal{B}(z)] = \alpha \mathbb{W}^{-1}[\mathcal{A}(z)] + \beta \mathbb{W}^{-1}[\mathcal{B}(z)]. \quad (3.45)$$

And third, the transform is norm-preserving (here I use eqs. (3.37), (3.2 $\|\cdot\|_{L^2}$) and (3.14 $\|\cdot\|_{HS}$):

$$\begin{aligned} \|\hat{A}\|_{HS}^2 &= \text{Tr}[\hat{A}^\dagger \hat{A}] = \int \frac{dz}{(2\pi)^N} \int \frac{dz'}{(2\pi)^N} \mathcal{A}^*(z) \mathcal{A}(z') \text{Tr}[\hat{A}_z \hat{A}_{z'}] \\ &= \int \frac{dz}{(2\pi)^N} \int \frac{dz'}{(2\pi)^N} \mathcal{A}^*(z) \mathcal{A}(z') (2\pi)^N \delta(z - z') = \int \frac{dz}{(2\pi)^N} \mathcal{A}^*(z) \mathcal{A}(z) = \|\mathcal{A}\|_{L^2}^2. \end{aligned}$$

This means, that two symbols that are close to each other as measured by the L^2 -norm will map to two operators that are close to each other in the Hilbert-Schmidt norm. The Wigner-Weyl symbol calculus thereby provides an efficient scheme for approximating operators: First transform the operator to its' symbol, then approximate the symbol by Taylor expansions (or by some other method) and finally transform the approximated symbol back to an operator.

3.2.5 Important Weyl Correspondences

The correspondence between operators and symbols established by the bijection \mathbb{W} is called the Weyl-correspondence. In the following I shall briefly show a few of the most important operator-to-symbol correspondences. First, consider the symbol of the position operator using the definition of eq. (3.39 \mathbb{W}_z):

$$\mathbb{W}_z[\hat{x}] = \int d\xi e^{-i\xi \cdot k} \left\langle x + \frac{\xi}{2} \middle| \hat{x} \middle| x - \frac{\xi}{2} \right\rangle = \int d\xi e^{-i\xi \cdot k} \left(x - \frac{\xi}{2} \right) \delta(\xi) = x. \quad (3.46)$$

Analogously, using eq. (3.40) I obtain $\mathbb{W}[\hat{k}] = k$. In fact, from the Taylor expansion of any function of only \hat{x} or only \hat{k} , I have: $\mathbb{W}[f(\hat{x})] = f(x)$ and $\mathbb{W}[f(\hat{k})] = f(k)$. This is of course what we could and should expect from a mapping between operators and symbols. However, when considering products of the position and momentum operator things become a bit less trivial:

$$\begin{aligned} \mathbb{W}[\hat{x}_i \hat{k}_j] &= \int d\xi e^{-i\xi \cdot k} \left\langle x + \frac{\xi}{2} \middle| \hat{x}_i \hat{k}_j \middle| x - \frac{\xi}{2} \right\rangle = \int d\xi e^{-i\xi \cdot k} \left(x_i + \frac{\xi_i}{2} \right) \left\langle x + \frac{\xi}{2} \middle| \hat{k}_j \middle| x - \frac{\xi}{2} \right\rangle \\ &= x_i \mathbb{W}[k_j] + \frac{1}{2} \int d\xi \xi_i e^{-i\xi \cdot k} \left\langle x + \frac{\xi}{2} \middle| \hat{k}_j \middle| x - \frac{\xi}{2} \right\rangle = x_i \mathbb{W}[k_j] + \frac{i}{2} \partial_{k_i} \mathbb{W}[k_j] = x_i k_j + \frac{i}{2} \delta_{ij}. \end{aligned}$$

Conversely, I have $\mathbb{W}[\hat{k}_j \hat{x}_i] = x_i k_j - \frac{i}{2} \delta_{ij}$. For dot products this mean

$$\mathbb{W}[\hat{x} \cdot \hat{k}] = x \cdot k + N \frac{i}{2}, \quad \mathbb{W}[\hat{k} \cdot \hat{x}] = x \cdot k - N \frac{i}{2}. \quad (3.47)$$

Evidently, the Wigner-Weyl transform takes the non-commutativity of the position and momentum operators into account and therefore $\hat{x}_i \hat{k}_j$ does not map to the same symbol as $\hat{k}_j \hat{x}_i$. In the words of Tracy et al., the Weyl symbol calculus treats position and momentum space on an equal footing. Therefore the operator corresponding to the symbol $x_i k_j$ is the symmetrized product:

$$\mathbb{W} \left[\frac{\hat{x}_i \hat{k}_j + \hat{k}_j \hat{x}_i}{2} \right] = x_i k_j. \quad (3.48)$$

The Wigner-Weyl transform of the product of two operators is known as the Moyal star product

$$\mathbb{W} [\hat{A} \hat{B}] = \mathcal{A}(\mathbf{z}) \star \mathcal{B}(\mathbf{z}). \quad (3.49)$$

It is possible to show (see Ref. [19]) that the Moyal star product can be given as an infinite series:

$$\mathcal{A}(\mathbf{z}) \star \mathcal{B}(\mathbf{z}) = \mathcal{A}(\mathbf{z}) \left[\sum_{m=0}^{\infty} \frac{1}{m!} \left(\frac{i}{2} \right)^m \left(\overleftarrow{\partial}_{\mathbf{x}} \cdot \overrightarrow{\partial}_{\mathbf{k}} - \overleftarrow{\partial}_{\mathbf{k}} \cdot \overrightarrow{\partial}_{\mathbf{x}} \right)^m \right] \mathcal{B}(\mathbf{z}) \quad (3.50a)$$

$$= \mathcal{A}(\mathbf{z}) \mathcal{B}(\mathbf{z}) + \frac{i}{2} \{ \mathcal{A}(\mathbf{z}), \mathcal{B}(\mathbf{z}) \} + \dots \quad (3.50b)$$

where $\overleftarrow{\partial}$ denotes differentiation to the left, $\overrightarrow{\partial}$ differentiation to the right and $\{ \mathcal{A}(\mathbf{z}), \mathcal{B}(\mathbf{z}) \}$ is the Poisson bracket defined as:

$$\{ \mathcal{A}(\mathbf{z}), \mathcal{B}(\mathbf{z}) \} := \partial_{\mathbf{x}} \mathcal{A}(\mathbf{z}) \cdot \partial_{\mathbf{k}} \mathcal{B}(\mathbf{z}) - \partial_{\mathbf{k}} \mathcal{A}(\mathbf{z}) \cdot \partial_{\mathbf{x}} \mathcal{B}(\mathbf{z}) \quad (3.51)$$

The differential operator in the parenthesis is known as the Janus operator (Ref. [19]):

$$\hat{\mathcal{L}} := \overleftarrow{\partial}_{\mathbf{x}} \cdot \overrightarrow{\partial}_{\mathbf{k}} - \overleftarrow{\partial}_{\mathbf{k}} \cdot \overrightarrow{\partial}_{\mathbf{x}} = \overleftarrow{\partial}_{\mathbf{z}} \wedge \overrightarrow{\partial}_{\mathbf{z}}. \quad (3.52)$$

It allows to write the Moyal star product on the compact exponential form:

$$\mathcal{A}(\mathbf{z}) \star \mathcal{B}(\mathbf{z}) = \mathcal{A}(\mathbf{z}) \exp \left(\frac{i}{2} \hat{\mathcal{L}} \right) \mathcal{B}(\mathbf{z}). \quad (3.53)$$

Finally, I will state without further proofs some important Weyl-correspondences (Refs. [19, 7]):

$$f(\hat{\mathbf{x}}) \leftrightarrow f(\mathbf{x}) \quad (3.54a)$$

$$f(\hat{\mathbf{k}}) \leftrightarrow f(\mathbf{k}) \quad (3.54b)$$

$$\hat{x}_i \hat{k}_j \leftrightarrow x_i k_j + \frac{i}{2} \delta_{ij} \quad (3.54c)$$

$$\hat{k}_j \hat{x}_i \leftrightarrow x_i k_j - \frac{i}{2} \delta_{ij} \quad (3.54d)$$

$$\frac{\hat{x}_i \hat{k}_j + \hat{k}_j \hat{x}_i}{2} \leftrightarrow x_i k_j \quad (3.54e)$$

$$\hat{A} \hat{B} \leftrightarrow \mathcal{A}(\mathbf{z}) \star \mathcal{B}(\mathbf{z}) \quad (3.54f)$$

$$\frac{\hat{\mathbf{k}} f(\hat{\mathbf{x}}) + f(\hat{\mathbf{x}}) \hat{\mathbf{k}}}{2} \leftrightarrow \mathbf{k} f(\mathbf{x}) \quad (3.54g)$$

$$\frac{\hat{\mathbf{k}} \cdot \mathbf{f}(\hat{\mathbf{x}}) + \mathbf{f}(\hat{\mathbf{x}}) \cdot \hat{\mathbf{k}}}{2} \leftrightarrow \mathbf{k} \cdot \mathbf{f}(\mathbf{x}) \quad (3.54h)$$

4 Geometrical Optics

Simplicity lies concealed in this chaos, and it is only for us to discover it.

Augustin-Jean Fresnel, 1788 – 1827

4.1 The Stationary Scalar Wave Equation

Any linearized physical wave equation may be written on the following general integral form [5]

$$\sum_{n=1}^N \int d\mathbf{x}' \int dt' D_{mn}(\mathbf{x}, \mathbf{x}', t, t') \psi_n(\mathbf{x}', t') = 0, \quad (4.1)$$

where ψ_n are components of the N -dimensional wave field ψ and $D \in \mathbb{C}^{N \times N}$ is the dispersion kernel matrix, sometimes called the wave operator matrix. The wave equation must be equipped with sufficient initial or boundary conditions. The use of δ -functions allow us to include both local and non-local effects in the integral formulation of eq. (4.1). As an example the scalar Helmholtz equation (see e.g. Ref. [18, p. 415]) given by:

$$\nabla^2 \psi(\mathbf{x}) + n^2(\mathbf{x}) \psi(\mathbf{x}) = 0 \quad (4.2)$$

has the integral representation of eq. (4.1) with (Ref. [7, p. 8]):

$$D(\mathbf{x}, \mathbf{x}') = \nabla'^2 \delta(\mathbf{x} - \mathbf{x}') + n^2(\mathbf{x}') \delta(\mathbf{x} - \mathbf{x}'). \quad (4.3)$$

When applying the dispersion kernel above to ψ , the derivative of the δ -function can be transferred to ψ via integration by parts.

In this thesis, from this point and forward, I will only consider stationary scalar wave equations. I assume cartesian coordinates and as a further simplification, I will also assume the background to be time-stationary implying that the dispersion function D can only depend on the time difference $t - t'$ (Ref. [5, p. 81])¹. The time-stationarity transforms the scalar wave equation into a convolution, which we may Fourier transform into frequency space:

$$\int dt' \int d\mathbf{x}' D(\mathbf{x}, \mathbf{x}', t - t') \psi(\mathbf{x}', t') = 0 \Rightarrow \int d\mathbf{x}' D(\mathbf{x}, \mathbf{x}', \omega) \psi(\mathbf{x}', \omega) = 0 \quad (4.4)$$

In the following derivation I shall assume a fixed ω is given and suppress the dependency of the dispersion relation on ω . The time-stationary scalar wave equation I consider is therefore:

$$\int d\mathbf{x}' D(\mathbf{x}, \mathbf{x}') \psi(\mathbf{x}') = 0, \quad (4.5)$$

It is definitely possible to generalize the theory to time-dependent fields. Non-stationary waves could be included by replacing the spatial coordinates \mathbf{x} with space-time coordinates equipped with an appropriate metric, see Ref. [4]. To the best of my knowledge, the

¹It is a general feature of response functions for time independent Hamiltonians that they are translation invariant in time. See Ref. [14, p. 89].

MGO theory described in Refs. [10, 11, 12, 7, 8] has thus far only been derived for scalar wave fields. The interested reader may consult Ref. [5] for a gentle introduction to GO formulated for vector fields or Ref. [4] which also provides the generalization to curvilinear coordinates (also Ref. [15] is a good introduction to curvilinear coordinates in the context of plasma physics).

As discussed in section 3.1 of chapter 3, the function $D(\mathbf{x}, \mathbf{x}')$ of eq. (4.5) can be seen as the position representation of a dispersion operator \hat{D} . That is $D(\mathbf{x}, \mathbf{x}') = \langle \mathbf{x} | \hat{D} | \mathbf{x}' \rangle$. I may therefore write the general wave equation, eq. (4.5), in Dirac bracket notation:

$$\hat{D}(\hat{\mathbf{x}}, \hat{\mathbf{k}}) |\psi\rangle = |0\rangle, \quad (4.6)$$

where $|0\rangle$ is the null vector and I assume that the operator \hat{D} can be expressed as a function of the position and momentum operators.

4.2 The Eikonal Approximation (WKB)

The essential step in deriving the GO equations is to describe the field $\psi(\mathbf{x})$ as rapid oscillations modulated by gradual variations in amplitude and wavelength. This is the eikonal approximation, also known as the WKB approximation (Wentzel, Kramers, Brillouin)². The eikonal ansatz assumes solutions on the form

$$\psi(\mathbf{x}) = \phi(\mathbf{x}) e^{i\theta(\mathbf{x})}. \quad (4.7)$$

$\phi(\mathbf{x})$ is the envelope and $\theta(\mathbf{x})$ is the phase. The approximation lies in assuming that the amplitude $\phi(\mathbf{x})$ is slowly varying, such that high order derivatives can be neglected. I will return to this. For now, motivated by eq. (4.7) and without making any approximation yet, I may define the envelope field:

$$|\phi\rangle := e^{-i\theta(\hat{\mathbf{x}})} |\psi\rangle. \quad (4.8)$$

By transferring the phase dependence from the field $|\psi\rangle$ to the operator \hat{D} I may represent eq. (4.6) as an equation of the envelope $|\phi\rangle$. For the representations to agree, matrix elements of the old \hat{D} and new phase-dependent \hat{D} must be equal³:

$$\langle \psi_1 | \hat{D} | \psi_2 \rangle = \langle \phi_1 | e^{-i\theta(\hat{\mathbf{x}})} \hat{D} e^{i\theta(\hat{\mathbf{x}})} | \phi_2 \rangle. \quad (4.9)$$

Thereby eq. (4.6) becomes

$$\hat{D}' |\phi\rangle = |0\rangle \quad \text{where} \quad \hat{D}' = e^{-i\theta(\hat{\mathbf{x}})} \hat{D}(\hat{\mathbf{x}}, \hat{\mathbf{k}}) e^{i\theta(\hat{\mathbf{x}})}. \quad (4.10)$$

The wave equation, eq. (4.10), is so far exact. To approximate it I employ the Weyl symbol calculus introduced in section 3.2 of chapter 3 in three steps: I) I transform the operator

²Wentzel, Kramers, and Brillouin published the first examples of applying this approximation scheme to Schrödinger's equation in 1926, see Ref. [5, p. 22]. Similar approximation schemes had also been invented already in the nineteenth century by Liouville and Green among others and therefore the approximation is sometimes called the LG method.

³Note, how this is in complete analogy with the Heisenberg picture of quantum mechanics (Ref. [14, ch. 5]), where $-\hat{H}t$ plays the role of our phase $\theta(\hat{\mathbf{x}})$. In the Heisenberg picture, the Hamiltonian H is assumed time-independent and the time dependence is transferred from the state to the operator by:

$$|\psi_{\text{Heisenberg}}\rangle := e^{i\hat{H}t} |\psi(t)\rangle$$

$$\hat{A}_{\text{Heisenberg}} := e^{i\hat{H}t} \hat{A} e^{-i\hat{H}t}.$$

For a time-stationary system like ours, the effective Hamiltonian therefore is $\hat{H} = -\hat{\Omega} := -\partial_t \theta(\hat{\mathbf{x}}, t)$.

$\hat{D}' = e^{-i\theta(\hat{\mathbf{x}})} \hat{D}(\hat{\mathbf{x}}, \hat{\mathbf{k}}) e^{i\theta(\hat{\mathbf{x}})}$ to its' corresponding Weyl symbol $\mathcal{D}'(\mathbf{z})$. II) I approximate the symbol. III) I transform it back to an approximated operator. Schematically the procedure looks like:

$$\begin{array}{ccc} \hat{D}' & \approx & \hat{D}'' \\ \text{I) } \downarrow \mathbb{W}_{\mathbf{z}} & & \text{III) } \uparrow \mathbb{W}^{-1} \\ \mathcal{D}'(\mathbf{z}) & \stackrel{\text{II) }}{\approx} & \mathcal{D}''(\mathbf{z}) \end{array} \quad (4.11)$$

Step I)

With the definition in eq. (3.39 $\mathbb{W}_{\mathbf{z}}$), the Wigner-Weyl transform of the phase dependent dispersion operator is:

$$\begin{aligned} \mathcal{D}'(\mathbf{z}) = \mathbb{W}_{\mathbf{z}} \left[e^{-i\theta(\hat{\mathbf{x}})} \hat{D}(\hat{\mathbf{x}}, \hat{\mathbf{k}}) e^{i\theta(\hat{\mathbf{x}})} \right] &= \int d\xi e^{-i\xi \cdot \mathbf{k}} \left\langle \mathbf{x} + \frac{\xi}{2} \middle| e^{-i\theta(\hat{\mathbf{x}})} \hat{D}(\hat{\mathbf{x}}, \hat{\mathbf{k}}) e^{i\theta(\hat{\mathbf{x}})} \middle| \mathbf{x} - \frac{\xi}{2} \right\rangle \\ &= \int d\xi e^{-i[\xi \cdot \mathbf{k} + \theta(\mathbf{x} + \frac{\xi}{2}) - \theta(\mathbf{x} - \frac{\xi}{2})]} \left\langle \mathbf{x} + \frac{\xi}{2} \middle| \hat{D}(\hat{\mathbf{x}}, \hat{\mathbf{k}}) \middle| \mathbf{x} - \frac{\xi}{2} \right\rangle. \end{aligned} \quad (4.12)$$

From eq. (A.10 Taylor), the Taylor expansion of $\theta\left(\mathbf{x} \pm \frac{\xi}{2}\right)$ is (Ref. [4]):

$$\theta\left(\mathbf{x} \pm \frac{\xi}{2}\right) = \theta(\mathbf{x}) \pm \frac{1}{2} \xi \cdot \partial_{\mathbf{x}} \theta(\mathbf{x}) + \frac{1}{2^2} \frac{1}{2!} \xi \xi : \partial_{\mathbf{x}} \partial_{\mathbf{x}} \theta(\mathbf{x}) \pm \frac{1}{2^3} \frac{1}{3!} \xi \xi \xi : \partial_{\mathbf{x}} \partial_{\mathbf{x}} \partial_{\mathbf{x}} \theta(\mathbf{x}) + \dots \quad (4.13)$$

Therefore, the difference in phases in the exponent is:

$$\theta\left(\mathbf{x} + \frac{\xi}{2}\right) - \theta\left(\mathbf{x} - \frac{\xi}{2}\right) = \xi \cdot \partial_{\mathbf{x}} \theta(\mathbf{x}) + \frac{1}{24} \xi \xi \xi : \partial_{\mathbf{x}} \partial_{\mathbf{x}} \partial_{\mathbf{x}} \theta(\mathbf{x}) + \dots \quad (4.14)$$

With this, the exponential of eq. (4.12) becomes:

$$\begin{aligned} e^{-i[\xi \cdot \mathbf{k} + \theta(\mathbf{x} + \frac{\xi}{2}) - \theta(\mathbf{x} - \frac{\xi}{2})]} &= e^{-i\xi \cdot [\mathbf{k} + \partial_{\mathbf{x}} \theta(\mathbf{x})]} \exp\left(-i\left[\frac{1}{24} \xi \xi \xi : \partial_{\mathbf{x}} \partial_{\mathbf{x}} \partial_{\mathbf{x}} \theta(\mathbf{x}) + \dots\right]\right) \\ &= e^{-i\xi \cdot [\mathbf{k} + \partial_{\mathbf{x}} \theta(\mathbf{x})]} \left(1 - i\left[\frac{1}{24} \xi \xi \xi : \partial_{\mathbf{x}} \partial_{\mathbf{x}} \partial_{\mathbf{x}} \theta(\mathbf{x}) + \dots\right] - \dots\right) \\ &= \left(1 - i\left[-\frac{i}{24} \partial_{\mathbf{x}} \partial_{\mathbf{x}} \partial_{\mathbf{x}} \theta(\mathbf{x}) : \partial_{\mathbf{k}} \partial_{\mathbf{k}} \partial_{\mathbf{k}} + \dots\right] - \dots\right) e^{-i\xi \cdot [\mathbf{k} + \partial_{\mathbf{x}} \theta(\mathbf{x})]}, \end{aligned}$$

where I in the second equality expanded the last exponential and in the third equality used that $\xi e^{i\xi \cdot \mathbf{k}} = i \partial_{\mathbf{k}} e^{i\xi \cdot \mathbf{k}}$. The Weyl symbol of eq. (4.12) therefore is:

$$\mathcal{D}'(\mathbf{z}) = \left[\int d\xi e^{-i\xi \cdot [\mathbf{k} + \partial_{\mathbf{x}} \theta(\mathbf{x})]} \left\langle \mathbf{x} + \frac{\xi}{2} \middle| \hat{D}(\hat{\mathbf{x}}, \hat{\mathbf{k}}) \middle| \mathbf{x} - \frac{\xi}{2} \right\rangle \right] \quad (4.15)$$

$$- \frac{1}{24} \partial_{\mathbf{x}} \partial_{\mathbf{x}} \partial_{\mathbf{x}} \theta(\mathbf{x}) : \partial_{\mathbf{k}} \partial_{\mathbf{k}} \partial_{\mathbf{k}} \left[\int d\xi e^{-i\xi \cdot [\mathbf{k} + \partial_{\mathbf{x}} \theta(\mathbf{x})]} \left\langle \mathbf{x} + \frac{\xi}{2} \middle| \hat{D}(\hat{\mathbf{x}}, \hat{\mathbf{k}}) \middle| \mathbf{x} - \frac{\xi}{2} \right\rangle \right] + \dots \quad (4.16)$$

$$= \mathcal{D}[\mathbf{x}, \mathbf{k} + \partial_{\mathbf{x}} \theta(\mathbf{x})] - \frac{1}{24} \partial_{\mathbf{x}} \partial_{\mathbf{x}} \partial_{\mathbf{x}} \theta(\mathbf{x}) : \partial_{\mathbf{k}} \partial_{\mathbf{k}} \partial_{\mathbf{k}} \mathcal{D}[\mathbf{x}, \mathbf{k} + \partial_{\mathbf{x}} \theta(\mathbf{x})] + \dots \quad (4.17)$$

So far everything is still exact. Now for the approximation of the Weyl symbol:

Step II)

Note how the integral of eq. (4.15) has the rapidly oscillating exponential factor $e^{-i\xi[\mathbf{k} + \partial_{\mathbf{x}}\theta(\mathbf{x})]}$. When integrating over ξ , oscillations with different phases will cancel each other out. This cancellation is least pronounced in the vicinity of where the phase of the exponential is constant. The main contribution to the integral will therefore be from the *stationary phase* point satisfying:

$$\partial_{\xi}[-\xi \cdot (\mathbf{k} - \partial_{\mathbf{x}}\theta)] = \partial_{\mathbf{x}}\theta - \mathbf{k} = \mathbf{0}. \quad (4.18)$$

It therefore makes sense to expand \mathcal{D} from eq. (4.17) around the local wave vector satisfying the stationary phase condition of eq. (4.18):

$$\mathcal{D}[\mathbf{x}, \mathbf{k} + \partial_{\mathbf{x}}\theta(\mathbf{x})] = \mathcal{D}[\mathbf{x}, \partial_{\mathbf{x}}\theta(\mathbf{x})] + \mathbf{k} \cdot \partial_{\mathbf{k}}\mathcal{D}[\mathbf{x}, \partial_{\mathbf{x}}\theta(\mathbf{x})] + \frac{1}{2}\mathbf{k}\mathbf{k} : \partial_{\mathbf{k}}\partial_{\mathbf{k}}\mathcal{D}[\mathbf{x}, \partial_{\mathbf{x}}\theta(\mathbf{x})] + \dots \quad (4.19)$$

Now, let:

$$k \sim \partial_{\mathbf{x}}\theta, \quad 1/L \sim \partial_{\mathbf{x}}\phi, \quad (4.20)$$

be the characteristic scale of variation for the phase and the envelope respectively. In the eikonal approximation it is assumed that the envelope ϕ varies on a much longer length scale compared to the wavelength $\lambda = 2\pi/k$. In other words $1/k \ll L$ or expressed in the small eikonal parameter:

$$\epsilon := \frac{1}{kL} \ll 1, \quad (4.21)$$

The envelope variation reflects the inhomogeneity of the medium which the wave field travels through and interacts with. A medium satisfying the criterion for the eikonal approximation above is said to be weakly inhomogeneous. Though perhaps not entirely obvious, the expansion of \mathcal{D} in \mathbf{k} in eq. (4.19) can be seen as an effective expansion in ϵ (Ref. [4]). The reasoning for this is that the inverse Wigner transformation in step III) will map \mathbf{k} into the operator $\hat{\mathbf{k}}$. Since the (approximated) dispersion operator \hat{D}'' is applied to the envelope state in the wave equation eq. (4.10), $\hat{\mathbf{k}}$ will operate on the envelope $|\phi\rangle$. When the dust has settled after step III), an effective order of magnitude estimate therefore gives

$$\mathbf{k} \sim \langle \mathbf{x} | \hat{\mathbf{k}} | \phi \rangle \sim \partial_{\mathbf{x}}\phi(\mathbf{x}) \sim 1/L \quad (4.22)$$

Thereby $\mathbf{k} \cdot \partial_{\mathbf{k}} \sim \epsilon$ and the expansion in eq. (4.19) is really an expansion in ϵ . Another order of magnitude estimate, shows that the third order differential operator is $\mathcal{O}(\epsilon^2)$:

$$[\partial_{\mathbf{x}}\partial_{\mathbf{x}}][\partial_{\mathbf{x}}\theta(\mathbf{x})] : [\partial_{\mathbf{k}}\partial_{\mathbf{k}}\partial_{\mathbf{k}}] \sim \left[\frac{1}{L^2} \right] [k] \left[\frac{1}{k^3} \right] = \epsilon^2. \quad (4.23)$$

Keeping only $\mathcal{O}(\epsilon)$ terms, the approximated Weyl symbol therefore becomes:

$$\mathcal{D}''(\mathbf{z}) = \mathcal{D}[\mathbf{x}, \mathbf{k}(\mathbf{x})] - \mathbf{k} \cdot \mathbf{v}(\mathbf{x}) \quad (4.24)$$

where I define the local wave vector and local group velocity⁴ by:

$$\mathbf{k}(\mathbf{x}) := \partial_{\mathbf{x}}\theta(\mathbf{x}) \quad (4.25)$$

$$\mathbf{v}(\mathbf{x}) := -\partial_{\mathbf{k}}\mathcal{D}(\mathbf{x}, \mathbf{k}(\mathbf{x})). \quad (4.26)$$

So to be clear: \mathbf{k} is generally any wave vector, whereas $\mathbf{k}(\mathbf{x})$ is as a function of \mathbf{x} which I call the local wave vector. The two are not in general equal and unless explicitly noted I shall be consistent in writing the local wave vector with its' argument.

⁴Note that I define the group velocity with the same sign as in [5] but the opposite sign of [7, 4]. The sign ambiguity stems from the fact that both D and $-D$ are valid dispersion functions in the wave equation, eq. (4.5).

Step III)

The Weyl correspondence of eq. (3.54h) makes it easy to transform the approximated symbol of eq. (4.24) back into an operator:

$$\hat{D}' \approx \hat{D}'' := \mathbb{W}^{-1}[\mathcal{D}''(\mathbf{z})] = \hat{D}[\hat{\mathbf{x}}, \mathbf{k}(\hat{\mathbf{x}})] - \frac{\hat{\mathbf{k}} \cdot \mathbf{v}(\hat{\mathbf{x}}) + \mathbf{v}(\hat{\mathbf{x}}) \cdot \hat{\mathbf{k}}}{2}. \quad (4.27)$$

The equation can be further simplified by noticing:

$$\begin{aligned} \hat{\mathbf{k}} \cdot \mathbf{v}(\hat{\mathbf{x}}) |\psi\rangle &= \int d\mathbf{x}' |\mathbf{x}'\rangle (-i\partial_{\mathbf{x}'}) \cdot \langle \mathbf{x}' | \mathbf{v}(\hat{\mathbf{x}}) |\psi\rangle \\ &= \int d\mathbf{x}' |\mathbf{x}'\rangle (-i\partial_{\mathbf{x}'}) \cdot [\mathbf{v}(\mathbf{x}') \psi(\mathbf{x}')] \\ &= \left(\int d\mathbf{x}' |\mathbf{x}'\rangle (-i\partial_{\mathbf{x}'} \cdot \mathbf{v}(\mathbf{x}')) \langle \mathbf{x}' | + \int d\mathbf{x}' |\mathbf{x}'\rangle \mathbf{v}(\mathbf{x}') \cdot (-i\partial_{\mathbf{x}'}) \langle \mathbf{x}' | \right) |\psi\rangle \\ &= (-i\partial_{\mathbf{x}} \cdot \mathbf{v}(\hat{\mathbf{x}}) + \mathbf{v}(\hat{\mathbf{x}}) \cdot \hat{\mathbf{k}}) |\psi\rangle. \end{aligned}$$

Thereby, I end up with the wave equation result (Ref. [7, p. 10]):

$$\left(\mathcal{D}[\hat{\mathbf{x}}, \mathbf{k}(\hat{\mathbf{x}})] - \mathbf{v}(\hat{\mathbf{x}}) \cdot \hat{\mathbf{k}} + \frac{i}{2} \partial_{\mathbf{x}} \cdot \mathbf{v}(\hat{\mathbf{x}}) \right) |\phi\rangle = |0\rangle, \quad (4.28)$$

$$\hat{\mathbf{z}} := \begin{pmatrix} \hat{\mathbf{x}} \\ \hat{\mathbf{k}} \end{pmatrix}, \quad \mathcal{D}(\mathbf{z}) := \mathbb{W}[\hat{D}(\hat{\mathbf{z}})], \quad \mathbf{k}(\mathbf{x}) := \partial_{\mathbf{x}} \theta(\mathbf{x}), \quad \mathbf{v}(\mathbf{x}) := -\partial_{\mathbf{k}} \mathcal{D}(\mathbf{x}, \mathbf{k}) \Big|_{\mathbf{k}=\mathbf{k}(\mathbf{x})}. \quad (4.29)$$

The projection of the wave equation, eq. (4.28), onto position space gives:

$$\mathcal{D}[\mathbf{x}, \mathbf{k}(\mathbf{x})] \phi(\mathbf{x}) + i \left(\mathbf{v}(\mathbf{x}) \cdot \partial_{\mathbf{x}} + \frac{1}{2} \partial_{\mathbf{x}} \cdot \mathbf{v}(\mathbf{x}) \right) \phi(\mathbf{x}) = 0. \quad (4.30)$$

If I neglect dissipation, the original dispersion operator \hat{D} can be assumed to be hermitian and therefore its' Weyl symbol \mathcal{D} and its' derivative \mathbf{v} will both be real per eq. (3.43). Solving for the real and imaginary parts under this assumption gives the GO equations:

$$\mathcal{D}[\mathbf{x}, \mathbf{k}(\mathbf{x})] = 0. \quad (4.31a \text{ GO Disp.})$$

$$\mathbf{v}(\mathbf{x}) \cdot \partial_{\mathbf{x}} \phi(\mathbf{x}) + \frac{1}{2} [\partial_{\mathbf{x}} \cdot \mathbf{v}(\mathbf{x})] \phi(\mathbf{x}) = 0. \quad (4.31b \text{ GO Env.})$$

Equation (4.31a GO Disp.) is the local dispersion relation and eq. (4.31b GO Env.) is the envelope equation. The GO approximation of eq. (4.21) breaks down when the eikonal parameter $\epsilon = 1/(kL)$ is not small. This can typically happen at cutoffs where rays are reflected ($k \rightarrow 0$) or at focal points where rays converge ($L \rightarrow 0$) (Ref. [7]). Points where $kL \rightarrow 0$ and the eikonal approximation breaks down are in general called caustics. The goal of the MGO method studied in this thesis is to lift the eikonal restriction $\epsilon \ll 1$ and reinstate the validity of GO at caustics.

4.3 Ray Tracing

Let $\mathbf{z} = (\mathbf{x}, \mathbf{k})$ denote the $2N$ -dimensional phase space coordinates and define $\mathcal{D}(\mathbf{z}) := \mathcal{D}(\mathbf{x}, \mathbf{k})$. The condition $\mathcal{D}(\mathbf{z}) = 0$ is satisfied on a $2N - 1$ dimensional surface in phase space called the dispersion surface⁵. A conceptual drawing of the dispersion surface in phase space is shown in fig. 4.1 in orange.

⁵Formally, the dispersion surface $\mathbf{z}(\sigma)$ is a map $\mathbf{z} : U \rightarrow \mathbb{R}^{2N}$, where $U \subseteq \mathbb{R}^{2N-1}$ is an open, non-empty subset of a $2N - 1$ -dimensional parameter space and $\mathcal{D}[\mathbf{z}(\sigma)] = 0 \forall \sigma$. The dimension of a surface is the number of parameters $\sigma_1, \dots, \sigma_{2N-1}$ required to parameterize it. Ref. [20, p. 3].

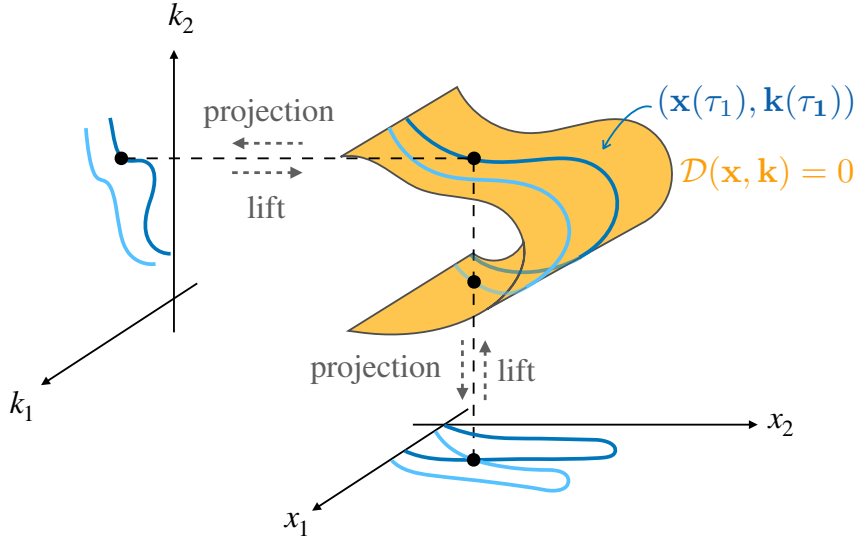


Figure 4.1: Conceptual illustration of the dispersion surface and two rays in phase space. In this example \mathbf{x} -space is two-dimensional and the four-dimensional phase space is conceptually visualized as a 3D space. The orange dispersion surface is really three-dimensional but since phase space is represented in 3D it is drawn as a 2D surface. The dark and light blue curves corresponds to two different paths which satisfy the dispersion relation and are therefore contained within the orange dispersion surface. The projection and lifting of the path to and from \mathbf{x} and \mathbf{k} space is also illustrated. The illustration is inspired by Figure 3.1 and Figure 3.2 in Ref. [5].

Now consider a path $\mathbf{x}(\tau_1)$ in position space parameterized by some $\tau_1 \in I \subset \mathbb{R}$ and define the corresponding local wave vector dictated by this parameterized path $\mathbf{k}(\tau_1) := \mathbf{k}[\mathbf{x}(\tau_1)]$. The mapping $\mathbf{x}(\tau_1) \mapsto (\mathbf{x}(\tau_1), \mathbf{k}[\mathbf{x}(\tau_1)])$ takes the path in position space to a path, $\mathbf{z}(\tau_1)$, in phase space. To be precise, the path in phase space is the set of points $\{\mathbf{z}(\tau_1) = (\mathbf{x}(\tau_1), \mathbf{k}[\mathbf{x}(\tau_1)])^T \mid \tau_1 \in I\}$ which is the graph of the local wave vector $\mathbf{k}(\mathbf{x})$ ⁶. The mapping $\mathbf{x}(\tau_1) \mapsto \mathbf{z}(\tau_1)$ is also called a *lift* and conversely, the original path in position space may be obtained by a *projection* of $\mathbf{z}(\tau_1)$ onto position space. Similarly, the path $\mathbf{k}(\tau_1)$ in momentum space is a projection of the phase space path down to momentum space. A conceptual drawing of two such paths in position, momentum and phase space is shown on fig. 4.1 in different shades of blue. To satisfy the local dispersion relation of eq. (4.31a GO Disp.) along the path, $\mathbf{z}(\tau_1)$ must lie on the dispersion surface as illustrated on fig. 4.1. A path like $\mathbf{z}(\tau_1)$ which satisfy eq. (4.31a GO Disp.) is called a *ray* and I shall soon derive how the ray trajectory can be determined by launching a ray with an initial position and momentum given by $\mathbf{z}(\tau_1 = 0)$.

Now, instead of single rays, consider an entire region of position space $\mathbf{x}(\boldsymbol{\tau})$ parameterized by some $\boldsymbol{\tau} \in U \subseteq \mathbb{R}^N$. Similar to the case for a single ray, the mapping $\mathbf{x}(\boldsymbol{\tau}) \mapsto (\mathbf{x}(\boldsymbol{\tau}), \mathbf{k}(\boldsymbol{\tau}))$ defines a lift of the spatial region. Since the lift is generated from the gradient of the phase function, i.e. $\mathbf{k}(\mathbf{x}) = \partial_{\mathbf{x}}\theta(\mathbf{x})$, it is actually an example of what is called a Lagrange manifold. The Lagrange manifold is N -dimensional since it can be

⁶The graph of a map $f : A \rightarrow B$ is the set of all pairs $(x, f(x)) \in A \times B$ where \times denotes the Cartesian product of set A and B , see Ref. [20]. In our case $f(x) \sim \mathbf{k}(\mathbf{x})$, $A \sim \mathbb{R}^N$, $B \sim \mathbb{R}^N$ and $A \times B$ is the phase space.

parameterized by $\boldsymbol{\tau} \in \mathbb{R}^N$. To satisfy the local dispersion relation, eq. (4.31a GO Disp.), the N -dimensional Lagrange manifold must be a subset of the $2N - 1$ dimensional dispersion surface. A coherent wave field satisfying a given boundary and initial condition will have a single well-defined phase function $\theta(\mathbf{x})$ and therefore an associated Lagrange manifold $\mathbf{z}(\boldsymbol{\tau})$. To construct the manifold explicitly, I can launch a family of rays that span the manifold. In practice, I will let τ_1 be a longitudinal time parameter and then launch a set of rays from the same x_1 -position. Then $\boldsymbol{\tau}_\perp = (\tau_2, \tau_3)^T = (x_2^{(0)}, x_3^{(0)})^T$ are the perpendicular starting coordinates for each ray. Together $\boldsymbol{\tau} = (\tau_1, \boldsymbol{\tau}_\perp)^T$ parameterize the ray manifold $\mathbf{z}(\boldsymbol{\tau})$. Numerically, I can of course only launch a finite set of rays and τ_1 will be calculated for discrete time points, so the numerical ray manifold $\mathbf{z}(\boldsymbol{\tau})$ is defined on a discrete $\boldsymbol{\tau}$ grid.

4.3.1 Hamilton's Ray Equations

With the conceptual discussion above I am now ready to derive the ray equations of motion. First, note that the local wave vector is necessarily irrotational:

$$\partial_{\mathbf{x}} \times \mathbf{k}(\mathbf{x}) = \partial_{\mathbf{x}} \times \partial_{\mathbf{x}} \theta(\mathbf{x}) = \mathbf{0}. \quad \text{or} \quad \partial_{x_i} k_j(\mathbf{x}) = \partial_{x_j} k_i(\mathbf{x}). \quad (4.32)$$

Since $\mathbf{k}(\tau_1) := \mathbf{k}[\mathbf{x}(\tau_1)]$ its' derivative is determined from the chain rule:

$$\partial_{\tau_1} \mathbf{k}(\tau_1) = d_{\tau_1} \mathbf{k}[\mathbf{x}(\tau_1)] = (\partial_{\tau_1} \mathbf{x}(\tau_1)) \cdot (\partial_{\mathbf{x}} \mathbf{k}(\mathbf{x})) = (\partial_{\mathbf{x}} \mathbf{k}(\mathbf{x})) \cdot (\partial_{\tau_1} \mathbf{x}(\tau_1)), \quad (4.33)$$

where I used the irrotationality of eq. (4.32) in the last step. Also, I use implicit outer products in the equations and d_{τ_1} denotes the total derivative. Please see eq. (A.7) and eq. (A.3) for clarifications on the notation. I assume that the local dispersion relation $\mathcal{D}[\mathbf{z}(\tau_1 = 0)] = 0$ is satisfied initially for $\tau_1 = 0$. To continue satisfying $\mathcal{D}[\mathbf{z}(\tau_1)] = 0$ along the ray, I must have:

$$d_{\mathbf{x}} \mathcal{D}[\mathbf{x}, \mathbf{k}(\mathbf{x})] := \partial_{\mathbf{x}} \mathcal{D}[\mathbf{x}, \mathbf{k}(\mathbf{x})] + (\partial_{\mathbf{x}} \mathbf{k}(\mathbf{x})) \cdot \partial_{\mathbf{k}} \mathcal{D}[\mathbf{x}, \mathbf{k}(\mathbf{x})] = 0. \quad (4.34)$$

Therefore, if I choose the ray to move with the group velocity in position space:

$$\partial_{\tau_1} \mathbf{x}(\tau_1) = \mathbf{v} = -\partial_{\mathbf{k}} \mathcal{D}[\mathbf{x}, \mathbf{k}(\mathbf{x})], \quad (4.35)$$

then eqs. (4.33) and (4.34) gives me:

$$\partial_{\tau_1} \mathbf{k}(\tau_1) = \partial_{\mathbf{x}} \mathcal{D}[\mathbf{x}, \mathbf{k}(\mathbf{x})]. \quad (4.36)$$

Finally, the phase θ along the ray can be determined by simply integrating $\partial_{\mathbf{x}} \theta$:

$$\theta(\mathbf{x}) = \theta(\mathbf{x}_0) + \int_{\mathbf{x}_0}^{\mathbf{x}} d\mathbf{x}' \cdot \partial_{\mathbf{x}} \theta(\mathbf{x}') = \theta(\mathbf{x}_0) + \int_{\mathbf{x}_0}^{\mathbf{x}} d\mathbf{x}' \cdot \mathbf{k}(\mathbf{x}') \quad (4.37)$$

$$\text{or} \quad \theta(\tau_1) = \theta_0 + \int_0^{\tau_1} d\tau_1 \partial_{\tau_1} \mathbf{x}(\tau_1) \cdot \mathbf{k}(\tau_1). \quad (4.38)$$

Putting everything together I have arrived at the ray equations:

$$\dot{\mathbf{x}} = -\partial_{\mathbf{k}} \mathcal{D} \quad (4.39a)$$

$$\dot{\mathbf{k}} = \partial_{\mathbf{x}} \mathcal{D} \quad (4.39b)$$

$$\theta(\mathbf{x}) = \theta(\mathbf{x}_0) + \int_{\mathbf{x}_0}^{\mathbf{x}} d\mathbf{x}' \cdot \mathbf{k}(\mathbf{x}') \quad \text{or} \quad \theta(\tau_1) = \theta_0 + \int_0^{\tau_1} d\tau_1 \dot{\mathbf{x}}(\tau_1) \cdot \mathbf{k}(\tau_1), \quad (4.40)$$

where I introduced Newton's dot notation for the temporal derivative, $\dot{\mathbf{x}} = \partial_{\tau_1} \mathbf{x}(\tau_1)$, and suppressed the arguments of the dispersion symbol \mathcal{D} and ray coordinates $\mathbf{z}(\tau_1) = (\mathbf{x}(\tau_1), \mathbf{k}(\tau_1))^T$. Remarkably, the ray equations in eq. (4.39) are Hamilton's equations known from classical mechanics⁷, but now with the local dispersion function \mathcal{D} in the role of the Hamiltonian. Note how Hamilton's ray equations have reduced the original PDE or integro-differential wave-equation to a much simpler IVP:

$$\dot{\mathbf{z}} = -\mathbf{J}_{2N} \partial_{\mathbf{z}} \mathcal{D}, \quad \mathbf{z}(\tau_1 = 0) = \mathbf{z}_0, \quad (4.41)$$

where \mathbf{J}_{2N} is the symplectic matrix defined in eq. (3.28). Since the right hand side (RHS) has no explicit dependence on τ_1 the ordinary differential equation (ODE) is autonomous. This guarantees that solutions are unique in the sense that rays with different initial conditions can never cross (see e.g. Ref. [21, p. 278]). While this is true for the rays in phase space, there is no such constraint for the rays projected onto \mathbf{x} or \mathbf{k} space. Figure 4.1 illustrates this conceptually where the two rays cross in position space even though they don't cross in phase space. Thus, when we project the rays onto position space we are not seeing the full picture. In a similar manner, even if a single ray does not cross itself in phase space, it might still cross itself when projected down to \mathbf{x} or \mathbf{k} space. In fact these symptoms expose a general problem with projecting the GO equations of eq. (4.31) onto position space. The problem is closely related to the breakdown of the eikonal approximation, $\epsilon \ll 1$, which happens at caustics.

4.3.2 Field Reconstruction

With Hamilton's ray equations in eq. (4.39) we can determine the ray path and thereafter the phase along that path using eq. (4.40), but to calculate the field we also need the envelope. For convenience, I repeat eq. (4.31b GO Env.) governing the envelope evolution:

$$\mathbf{v}(\mathbf{x}) \cdot \partial_{\mathbf{x}} \phi(\mathbf{x}) + \frac{1}{2} [\partial_{\mathbf{x}} \cdot \mathbf{v}(\mathbf{x})] \phi(\mathbf{x}) = 0.$$

The ray parameterization, $\mathbf{x}(\boldsymbol{\tau})$, determines $\phi(\boldsymbol{\tau}) := \phi(\mathbf{x}(\boldsymbol{\tau}))$. Due to the choice of parameterization in eq. (4.35), the first term in the envelope equation is simply the derivative of ϕ with respect to τ_1 :

$$\partial_{\tau_1} \phi(\boldsymbol{\tau}) = \partial_{\tau_1} \mathbf{x}(\boldsymbol{\tau}) \cdot \partial_{\mathbf{x}} \phi(\boldsymbol{\tau}) = \mathbf{v}(\mathbf{x}) \cdot \partial_{\mathbf{x}} \phi(\mathbf{x}). \quad (4.42)$$

Following Ref. [22, p. 22] and Ref. [7, p. 12] I can simplify the divergence $\partial_{\mathbf{x}} \cdot \mathbf{v}$ as:

$$\begin{aligned} \partial_{\mathbf{x}} \cdot \mathbf{v}(\mathbf{x}) &= \text{Tr}(\partial_{\mathbf{x}} \mathbf{v}(\mathbf{x})) = \text{Tr}([\partial_{\mathbf{x}} \boldsymbol{\tau}] [\partial_{\boldsymbol{\tau}} \mathbf{v}(\boldsymbol{\tau})]) = \text{Tr}\left([\partial_{\boldsymbol{\tau}} \mathbf{x}]^{-1} (\partial_{\boldsymbol{\tau}} \mathbf{v}(\boldsymbol{\tau}))\right) \\ &= \text{Tr}\left([\partial_{\boldsymbol{\tau}} \mathbf{x}]^{-1} (\partial_{\boldsymbol{\tau}} \partial_{\tau_1} \mathbf{x}(\boldsymbol{\tau}))\right) = \text{Tr}\left([\partial_{\boldsymbol{\tau}} \mathbf{x}]^{-1} \partial_{\tau_1} (\partial_{\boldsymbol{\tau}} \mathbf{x}(\boldsymbol{\tau}))\right), \end{aligned}$$

where I used the chain rule and inverse function theorem under the assumption that the mapping $\mathbf{x}(\boldsymbol{\tau})$ is bijective. I shall soon discuss when this assumption breaks down. Using Jacobi's formula (See Ref. [23]) this becomes:

$$\partial_{\mathbf{x}} \cdot \mathbf{v}(\mathbf{x}) = \frac{\partial_{\tau_1} \det[\partial_{\boldsymbol{\tau}} \mathbf{x}(\boldsymbol{\tau})]}{\det[\partial_{\boldsymbol{\tau}} \mathbf{x}(\boldsymbol{\tau})]} = \partial_{\tau_1} \log[j(\boldsymbol{\tau})],$$

where, as in Ref. [7], I defined the Jacobian determinant of the path in position space:

$$j(\boldsymbol{\tau}) := \det[\partial_{\boldsymbol{\tau}} \mathbf{x}(\boldsymbol{\tau})]. \quad (4.43)$$

⁷Historically it is in fact the other way around: Hamilton originally developed the phase space methods for optics and only subsequently Hamilton's equations became a valuable tool to study classical particle motion. Ref. [5, p. xiii].

With this the envelope equation becomes:

$$\partial_{\tau_1} \phi(\mathbf{x}) = -\frac{1}{2} [\partial_{\tau_1} \log j(\boldsymbol{\tau})] \phi(\boldsymbol{\tau}) \quad (4.44)$$

The solution is obtained from straight forward integration,

$$\phi(\boldsymbol{\tau}) = \phi(0, \boldsymbol{\tau}_\perp) e^{-\frac{1}{2} \int_0^{\tau_1} \partial_{\tau_1} \log j(\tau'_1, \boldsymbol{\tau}_\perp) d\tau'_1} = \phi(0, \boldsymbol{\tau}_\perp) e^{-\frac{1}{2} (\log j(\boldsymbol{\tau}) - \log j(0, \boldsymbol{\tau}_\perp))},$$

which gives the result:

$$\phi(\boldsymbol{\tau}) = \phi_0(\boldsymbol{\tau}_\perp) \sqrt{\frac{j_0(\boldsymbol{\tau}_\perp)}{j(\boldsymbol{\tau})}}, \quad (4.45)$$

where I defined $\phi_0(\boldsymbol{\tau}_\perp) := \phi(0, \boldsymbol{\tau}_\perp)$ and $j_0(\boldsymbol{\tau}_\perp) := j(0, \boldsymbol{\tau}_\perp)$ from the initial conditions (Ref. [7]). With this, we have the essential equations of the GO method. First, trace a ray manifold using eq. (4.39) to obtain $\mathbf{x}(\boldsymbol{\tau}), \mathbf{k}(\boldsymbol{\tau})$. Then, determine $\theta(\boldsymbol{\tau})$ from eq. (4.40) and $\phi(\boldsymbol{\tau})$ from eq. (4.45). The final field as a function of position is simply:

$$\psi(\mathbf{x}) = \psi[\boldsymbol{\tau}(\mathbf{x})] = \phi[\boldsymbol{\tau}(\mathbf{x})] e^{i\theta[\boldsymbol{\tau}(\mathbf{x})]}, \quad (4.46)$$

4.3.3 The Caustic Problem

For eq. (4.46) above to be meaningful, the map $\mathbf{x}(\boldsymbol{\tau})$ needs to have an inverse $\boldsymbol{\tau}(\mathbf{x})$. This breaks down if $\mathbf{x}(\boldsymbol{\tau})$ is not bijective. Geometrically, $\mathbf{x}(\boldsymbol{\tau})$ being bijective means that rays on the ray manifold do not cross in position space. On fig. 4.1 the interpretation would be, that the projection of the ray manifold⁸ onto position space cannot be many-to-one. This also highlights why caustics are typically reflection and focal points which in both cases cause rays to cross. The problem is seen even more clearly from eq. (4.45), which is not defined when the Jacobian $[\partial_{\boldsymbol{\tau}} \mathbf{x}(\boldsymbol{\tau})]^T$ becomes singular, i.e. when

$$j(\boldsymbol{\tau}) \rightarrow 0. \quad (4.47)$$

Note that $j(\boldsymbol{\tau}) = 0$ is exactly the condition that the local inverse map $\boldsymbol{\tau}(\mathbf{x})$ becomes ill-defined. To see the relevance that $j(\boldsymbol{\tau})$ has for the projection of the ray manifold onto \mathbf{x} -space, consider:

$$\det(\partial_{\mathbf{x}} \mathbf{k}(\boldsymbol{\tau})) = \det([\partial_{\boldsymbol{\tau}} \mathbf{x}]^{-1} [\partial_{\boldsymbol{\tau}} \mathbf{k}]) = \frac{\det \partial_{\boldsymbol{\tau}} \mathbf{k}}{j(\boldsymbol{\tau})}, \quad (4.48)$$

where again, I assumed that $\mathbf{x}(\boldsymbol{\tau})$ is invertible. As before, this assumption breaks down at $j(\boldsymbol{\tau}) = 0$ where

$$\det \partial_{\mathbf{x}} \mathbf{k}(\mathbf{x}) = \det \partial_{\mathbf{x}} \partial_{\mathbf{x}} \theta(\mathbf{x}) \rightarrow \infty. \quad (4.49)$$

In 1D, the interpretation of eq. (4.49) would be that the slope $\partial_x k(x)$ of the ray manifold goes to infinity and therefore the function $k(x)$ does not have an explicit representation at the caustic point. In general I shall speak of the points where $j(\boldsymbol{\tau}) = 0$ as projection singularities⁹, since the ray-manifold no longer has a well-defined one-to-one projection if the Jacobian becomes singular. In summary: Within the GO approximation the wave

⁸We may conceptually think of the orange surface on fig. 4.1 as the ray manifold, since it is drawn in a 3D space.

⁹Note that singular has multiple meanings: It refers both to the Jacobian matrix having 0 determinant and to the mapping $\partial_{\mathbf{x}} \mathbf{k}(\mathbf{x})$ being non-analytic at the caustic. Both meanings are unified in saying that the projection is singular, i.e. ill-behaved at the caustic.

field diverges exactly where the projection of the ray manifold becomes singular (Ref. [5, p. 147]).

Note however, that we can circumvent part of the problem by dividing the multi-valued $\tau(\mathbf{x})$ into single-valued branches $\tau_1(\mathbf{x}), \tau_2(\mathbf{x}), \dots, \tau_b(\mathbf{x})$. To be precise, a branch can be determined as a region in τ -space which has constant sign of $j(\tau)$. For a simple reflection, this would mean that the incoming and outgoing rays live on two separated branches. The final wave field is then obtained by summing over all branches:

$$\psi(\mathbf{x}) = \sum_{i=1}^b \phi[\tau_i(\mathbf{x})] e^{i\theta[\tau_i(\mathbf{x})]}. \quad (4.50)$$

An important detail to this approach is that anytime the rays parse through a caustic point, they incur a phase shift, such that instead of using eq. (4.40), one should calculate the phase through (see Ref. [5, p. 184, 195, 204, 421]):

$$\theta(\tau_1) = \theta_0 + \int_0^{\tau_1} d\tau_1 \dot{\mathbf{x}}(\tau_1) \cdot \mathbf{k}(\tau_1) + \sum_{\tau_*, \tau_* < \tau_1} \mu(\tau_*) \frac{\pi}{2}, \quad (4.51)$$

Here $\mu(\tau_*)$ is the so-called Keller-Maslov index of the caustic at $\tau_1 = \tau_*$ and the sum goes over all caustics encountered along the ray up until time τ_1 . The Keller-Maslov index¹⁰ depends only upon the local geometry at the caustic. Fortunately, in general there are only a limited number of caustic types to consider. Caustics can namely be analyzed as optical catastrophes and classified according to their codimension. That is, the minimum number of dimensions required to observe the caustic. The examples in this thesis are all of the fold caustic type which has $\mu(\tau_*) = 1$. A strong advantage of the MGO method, which is the main focus of this thesis, is that it is agnostic to the specific type of caustic. It is therefore not relevant for this project to dive deeper into the catastrophe theoretical categorization of caustics. The interested reader is referred to Ref. [7, 12] for further details.

By summing over branches in eq. (4.50) and accounting for the phase shift using eq. (4.51), it is no longer a problem that rays cross and the solution is now well-defined away from caustics. However, the solution still diverges when the projection of the ray manifold is singular, i.e. when $j(\tau) = 0$. In chapter 6 I shall introduce the MGO method which attempts to lift this projection singularity. But, before doing so I will show some results from a numerical implementation of the GO equations.

4.4 Numerical Details

My numerical implementation of the GO method is implemented in Python and the code is available at the GitHub Repository in Ref. [13]. The method follows the basic step outlined above: First trace a family of rays to obtain a ray manifold defined on a discrete $\tau = (\tau_1, x_2^{(0)}, x_3^{(0)})^T$ grid. From the ray manifold calculate the phase using eq. (4.40) and

¹⁰In general, the Keller-Maslov index is related to the focusing tensor defined as the Hessian matrix of the phase, $\partial_{\mathbf{x}} \partial_{\mathbf{x}} \theta(\mathbf{x})$. Away from caustics where the focusing tensor is non-singular, the Keller-Maslov index is defined as the signature of the focusing tensor. That is, the sum of the signs of the eigenvalues:

$$\mu := \text{sign}[\partial_{\mathbf{x}} \partial_{\mathbf{x}} \theta[\tau_1(\mathbf{x})]] = \text{sign}[\partial_{\mathbf{x}} \mathbf{k} \theta[\tau_1(\mathbf{x})]] = \sum_{n=1}^N \lambda_n \quad (4.52)$$

At the caustic, where the focusing tensor is singular, transformations of coordinates are needed to cast the caustic into normal form and analyze the structure of the caustic (see Ref. [5, Appendix C]).

the envelope using eq. (4.45). Then divide the manifold into branches and sum up the contributions from these branches to get the final wave field of eq. (4.50). In the following I give a little more details starting with how I calculate the derivatives.

4.4.1 Calculating Derivatives

When solving the GO ray equations of eq. (4.39) and later on when introducing and implementing the MGO framework I need to compute the derivatives of functions. Therefore, I think it is appropriate to quickly cover some of the different strategies that exist for differentiating functions. Say we have a function $f : \mathbb{R}^n \rightarrow \mathbb{R}$ which we wish to differentiate to determine its' gradient:

$$\partial_{\mathbf{x}} f = \begin{pmatrix} \partial_{x_1} f \\ \partial_{x_2} f \\ \vdots \\ \partial_{x_n} f \end{pmatrix}$$

For simplicity I have chosen f to be scalar valued, but the following discussion easily generalizes to a vector valued function. An important distinction is whether f is known as an analytic expression composed of elementary functions or whether f is only known as a discrete signal defined on a grid of N data points $\mathbf{x}_1, \dots, \mathbf{x}_N$ with N function values f_1, \dots, f_N . In the first case f is on a *symbolic* form while in the second case f is on a *numeric* form. I shall run into both scenarios in the algorithms developed in this thesis. If f is on symbolic form we may then differentiate it symbolically to obtain a new analytic expression for the derivative $\partial_{\mathbf{x}} f$. The symbolic expression may then be stored for later evaluation. Alternatively we may compute the derivative at a desired point \mathbf{x}_0 directly as a number. Finally, if f is numerical, then the most obvious option is to use finite differences to compute the derivative at a desired point \mathbf{x}_0 directly as a number. These approaches are respectively known as symbol-to-symbol, symbol-to-number and number-to-number differentiation [24, Ch. 6]. There exists three common strategies for performing the differentiation [25]:

1. Finite differencing
2. Automatic differentiation
3. Symbolic differentiation

Finite Differencing

Finite differencing takes advantage of Taylor's theorem to approximate derivatives as difference quotients. The technique is for instance covered in Refs. [25, 26]. A common scheme is the central difference formula which approximates $\partial_{x_i} f(\mathbf{x})$ as

$$\partial_{x_i} f(\mathbf{x}) \approx \frac{f(\mathbf{x} + h\check{\mathbf{e}}_i) - f(\mathbf{x} - h\check{\mathbf{e}}_i)}{2h}, \quad (4.53)$$

where $h > 0$ is a small positive scalar and $\check{\mathbf{e}}_i$ is the i 'th cartesian unit vector. From Taylor's theorem it is possible to show that the error of eq. (4.53) is $\mathcal{O}(h^2)$ [26]. Finite differencing is useful for both symbol-to-number and number-to-number differentiation. If f is symbolic the central difference is simply evaluated by choosing a small $h > 0$ and then plugging into eq. (4.53). As a rule of thumb, to limit roundoff error h should be chosen as \sqrt{u} , where u is the unit roundoff ($u \approx 1.1 \times 10^{-16}$ in double-precision floating point arithmetic) [25, p. 196]. If instead f is numeric, then eq. (4.53) is evaluated as the difference between f -values on grid points and h is taken as the distance between grid points. For the endpoints of the signal which has no neighbouring gridpoints, one may

use the left and right three-point difference which like eq. (4.53) also has an error of order $\mathcal{O}(h^2)$ [26]:

$$\partial_{x_i} f(\mathbf{x}) \approx \frac{1}{2h} [-3f(\mathbf{x}) + 4f(\mathbf{x} + h\check{\mathbf{e}}_i) - f(\mathbf{x} + 2h\check{\mathbf{e}}_i)] \quad (4.54a)$$

$$\partial_{x_i} f(\mathbf{x}) \approx \frac{1}{2h} [f(\mathbf{x} - 2h\check{\mathbf{e}}_i) - 4f(\mathbf{x} - h\check{\mathbf{e}}_i) + 3f(\mathbf{x})]. \quad (4.54b)$$

For the purpose of this thesis, I developed my own simple module using eqs. (4.53) and (4.54) capable of performing number-to-number finite differencing on general vector valued functions $\mathbf{f} \rightarrow \mathbb{R}^n \rightarrow \mathbb{R}^m$. The module can be found in the `finite_diff.py` file on the GitHub repository, Ref. [13].

Automatic Differentiation

Automatic differentiation is a scheme which is used in a variety of fields including constrained optimization [25, Ch. 8] and machine learning [24, Ch. 6]. It can take both a symbol-to-symbol and symbol-to-number approach. The core idea is to recognize that any function can be decomposed into a set of sequentially applied elementary functions of either 1 variable (e.g. sin, exp, log, x^2 , etc.) or 2 variables ($x+y$, $x \times y$, x/y , x^y , etc.). Then the chain rule of differentiation may be used in sequence on these elementary functions to arrive at a total derivative. A function f may be represented by its' computational graph. This is best illustrated by some examples. First, consider the function $f(x) = \sin^2(2x)$. We may write

$$f(x) = f_3(f_2(f_1(x))) = f_3(f_2(y)) = f_3(z), \quad \text{where}$$

$$y = f_1(x) = 2x, \quad z = f_2(y) = \sin y, \quad f = f_3(z) = z^2.$$

This can be represented in a computational graph of f as shown in fig. 4.2 (a).

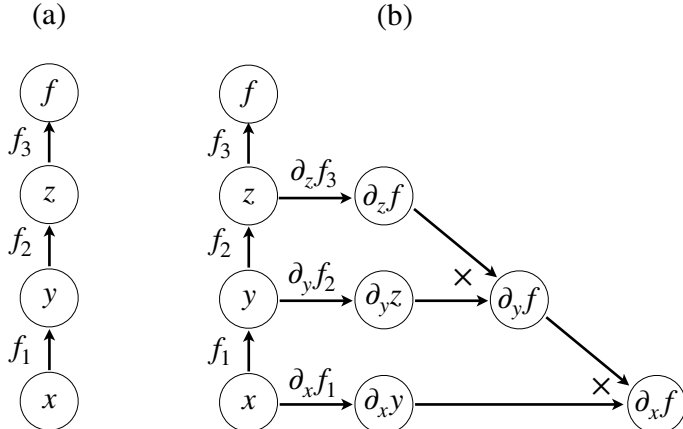


Figure 4.2: A simple illustration of the reverse mode (also known as back-propagation) for automatic differentiation. (a) Computational graph of the function $f(x) = f_3(f_2(f_1(x)))$. The function is evaluated by forward propagating x through the graph. (b) Computational graph after back-propagation algorithm instructing how to differentiate f with respect to x .

The computational graph on fig. 4.2 is an instruction to evaluate f by propagating x through the intermediate functions. When the computation in this manner flows with the arrows it is called forward propagation [24]. The chain rule makes it straightforward to calculate the derivative:

$$f(x) = \frac{\partial f}{\partial z} \frac{\partial z}{\partial y} \frac{\partial y}{\partial x}. \quad (4.55)$$

In our specific example this is:

$$\partial_x f(x_0) = 2z \Big|_{z=\sin y, y=2x_0} \cos(y) \Big|_{y=2x_0} = 4 \sin(2x_0) \cos(2x_0)$$

In a symbol-to-symbol approach to automatic differentiation, the chain rule is constructed by the back-propagation algorithm also known as reverse mode. The technique adds nodes to the graph corresponding to the intermediate derivatives as shown on fig. 4.3 (b). This step is called back propagation or reverse mode. The computational graph including derivative nodes need not be evaluated immediately, but can be stored as a symbolic expression of the derivative [24, Ch. 6]. This is the approach taken by libraries such as Theano [27] and TensorFlow [28].

In a symbol-to-number approach, instead of storing the graph with its' derivatives, the back-propagated derivative is evaluated immediately at each input value of interest. For instance, in our example the input $x_0 = 0.393 \approx \pi/4$ would give the value

$$\partial_x f(0.393) = 1.999\dots$$

This is the approach taken by PyTorch [29] where, unless explicitly specified by the user, the graph of derivatives is not retained in memory. Of cause, the approach of automatic

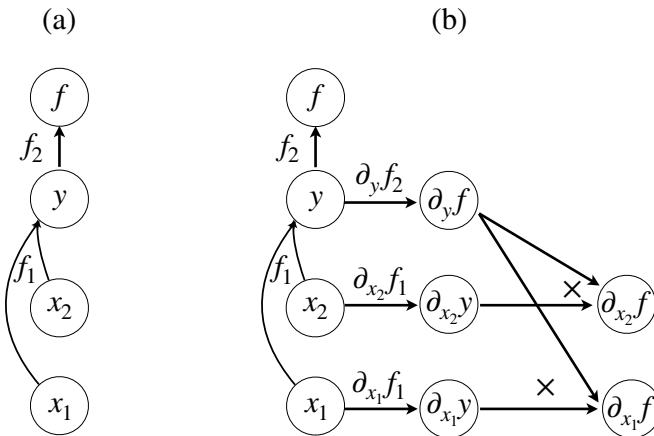


Figure 4.3: A simple illustration of the reverse mode (also known as back-propagation) for automatic differentiation of a function of two variables. (a) Computational graph of the function $f(x) = f_2(f_1(x_1, x_2))$. The function is evaluated by forward propagating (x_1, x_2) through the graph. (b) Computational graph after back-propagation algorithm instructing how to differentiate f with respect to x_1 and x_2 .

differentiation generalizes to functions of more variables. As an example consider,

$$f(x_1, x_2) = e^{x_1+x_2} = f_2(f_1(x_1, x_2)) = f_2(y) \quad \text{where}$$

$$y = f_1(x_1, x_2) = x_1 + x_2, \quad f = f_2(y) = e^y.$$

Its' computational graph is shown in fig. 4.3 (a). The graph after applying the reverse mode algorithm is shown on fig. 4.3 (b) and it contains the instructions to calculate $\partial_{x_1} f, \partial_{x_2} f$ which make up the gradient $\partial_x f$. The procedure also generalized to vector-valued and tensor functions. For more literature on specific algorithms to perform back propagation, please see [25, Ch. 8] and [24, Ch. 6].

In this thesis, I used PyTorch [29] to calculate the gradients needed to solve the ray equations, eq. (4.39). Two minor technical details when working with PyTorch together

with NumPy is how to elegantly cast datatypes back and forth from NumPy arrays to Torch tensor and how to correctly shape arrays (Torch tensors) representing respectively vectors and scalars. To solve these problems, I developed a small module with a python decorator and some helper functions. The module makes it simple to define a dispersion relation $D(\mathbf{x}, \mathbf{k}, \omega)$ which can be automatically differentiated and efficiently evaluated on a grid of datapoints. Documentation of this can be seen in my `torch_helper.py` module on GitHub [13].

Symbolic Differentiation

Symbolic differentiation is similar to the symbol-to-symbol approach of automatic differentiation, but the focus here is on achieving a simple closed-form expression of the derivatives rather than calculating derivatives as efficiently as possible. Most computer algebra systems such as Mathematica [30], Maple [31] and the Sympy python package [32] supports some version of symbolic differentiation [25]. I have not used symbolic differentiation in the algorithms in this thesis, but it is of course a valuable aid when checking the validity of the obtained solutions.

4.4.2 Solving Hamilton's Ray Equations

I solved the ray equations of eq. (4.39) using the IVP solver from the SciPy library which uses the Runge-Kutta method of order 5(4), see Ref. [33]. I calculated the derivatives needed for the RHS of eq. (4.39) with automatic differentiation.

4.4.3 Constructing the Field

After having traced a family of rays, I have my parameterized dispersion manifold containing all necessary information to determine the wave field. To calculate both the phase of eq. (4.40) and envelope of eq. (4.45) I used finite differencing for calculating the derivatives. As mentioned in section 4.3.2 the final wave field is obtained from eq. (4.50) by summing up the contributions from different branches. To determine the branches, I used a flood fill image segmentation algorithm (See Ref. [34]) with the sign of $j(\boldsymbol{\tau})$ as a 3 channel image array (each channel corresponds to a dimension of $\boldsymbol{\tau}$). The flood fill algorithm selects areas of an image with the same color (it is the same algorithm used for the paint bucket tool in image editors). With this I get a set of branches $\boldsymbol{\tau}_1, \dots, \boldsymbol{\tau}_b$, where all points in each branch have the same sign of $j(\boldsymbol{\tau})$.

It is not trivial to sum the branches however, since the \mathbf{x} -positions on each branch are not the same. My solution to this was to interpolate the wave field onto an equidistant N -dimensional grid using SciPy's ND linear interpolation method (Ref. [35]). The interpolation thereby gives a mapping $\mathbf{x} \rightarrow \phi_i(\mathbf{x})$ for each branch i . The final wave field is then the sum of the interpolations:

$$\psi(\mathbf{x}) = \sum_i \phi_i(\mathbf{x}). \quad (4.56)$$

Note, that this worked perfectly in 1D, but in 2D and 3D the ND-interpolation method used is quite computationally expensive and scales badly with the grid resolution (it took 1 minute for a $100 \times 100 \times 3$ grid on my 2019 MacBook Pro and judging from a few numerical experiments the performance appears to scale roughly linearly with the number of grid points). Another non-trivial problem related to the interpolation is that the rays may span out a concave hull in position space as is for instance the case in the example on fig. 5.10 which I introduce in the next chapter. In other words, sometimes the interpolation may extend to a shadow region where there in fact is no field within the GO approximation. My current solution to this problem is to make an N -dimensional histogram of the ray positions and use this to generate a domain window function, such that I only evaluate the

interpolated field in regions where the smeared out density of ray positions is sufficiently high¹¹.

Having covered the details of my numerical GO implementation, I present in the next chapter the results.

¹¹Another approach which I have not investigated could be to use the caustic surface where $j(\tau) = 0$ as part of the domain boundary.

5 Examples of Geometrical Optics

In this chapter I will apply the GO method derived in chapter 4 to three examples:

1. Airy's equation in 1D
2. Weber's equation in 1D
3. Perpendicular O-mode in 2D

The first two examples are chosen, because they are two of the five different case studies that N. A. Lopez demonstrates the MGO method for analytically in Ref. [7]. The 2D example is inspired by Ref. [5] and is well suited for illustrating the ray manifold in more dimensions. For each example I will show the results both of the ray tracing and the field reconstruction. In chapter 7 I shall revisit the Airy and Weber examples with the automated MGO approach. But, before diving into the field reconstruction examples, I will show the results of ray-tracing for the O- and X-mode in a cold plasma using the AAH dispersion relation, eq. (2.20 AAH).

5.1 Traces of O and X mode in cold plasma

On figs. 5.1 to 5.4, I have plotted the results of solving the AAH dispersion relation, eq. (2.20 AAH) with different angles to the magnetic field, $\theta = 0^\circ, 10^\circ, 30^\circ, 90^\circ$. For each figure, I have shown both the exact solution in dashed colored lines as well as the approximated ray trajectories within the GO approximation in solid colored lines. To produce each Figure, I created plasma density profile linear in one direction $n_e(x) = x$. I then launched an O-mode and an X-mode with $k_x > 0$ from outside the plasma ($x = 0$ where $n_e(x) = 0$) as well as an X-mode with $k_x < 0$ from inside the plasma at an initial position close to the L-cutoff. The initial wave number was found from the initial position by choosing a \mathbf{k} -direction and solving the Appleton-Hartree dispersion for the amplitude of \mathbf{k} .

Besides the solution in $N^2, \omega_{pe}^2/\omega^2$ space I also show on figs. 5.1 to 5.4 (c) the CMA diagram introduced in section 2.3.3. It should be noted that the UH resonance $\omega = \tilde{\omega}_{UH}$ which I have plotted on figs. 5.1 to 5.3 indicates the actual resonance of the X-mode from eq. (2.26). This is slightly different from the conventional definition of the UH frequency, $\omega_{UH} := \sqrt{\omega_{ce}^2 + \omega_{pe}^2}$ which does not depend on the angle to the B -field (see eq. (2.27)). At $\theta = 90^\circ$, the two definitions agree: $\tilde{\omega}_{UH} = \omega_{UH}$. From figs. 5.1 to 5.4 I can see how the UH resonance moves closer to the plasma frequency as the angle decreases before finally merging at $\theta = 0^\circ$. The ray traces on CMA diagrams, figs. 5.1 to 5.4 (c) are all horizontal, since the B -field was held constant.

For $\theta > 0^\circ$ the O-mode is reflected at its' cutoff where $\omega = \omega_p$. Similarly the X-mode launched from outside the plasma is reflected at the R-cutoff. Finally, the X-mode launched from inside the plasma decelerates at the UH resonance. Within the eikonal approximation of GO no rays can propagate in the evanescent regions. This is also reflected in my ray tracing results on figs. 5.1 to 5.4 where no rays reach the grey evanescent area. It is therefore an intrinsic limitation in the currently presented formulation of the GO approximation that it is not capable of reconstructing the evanescent field.

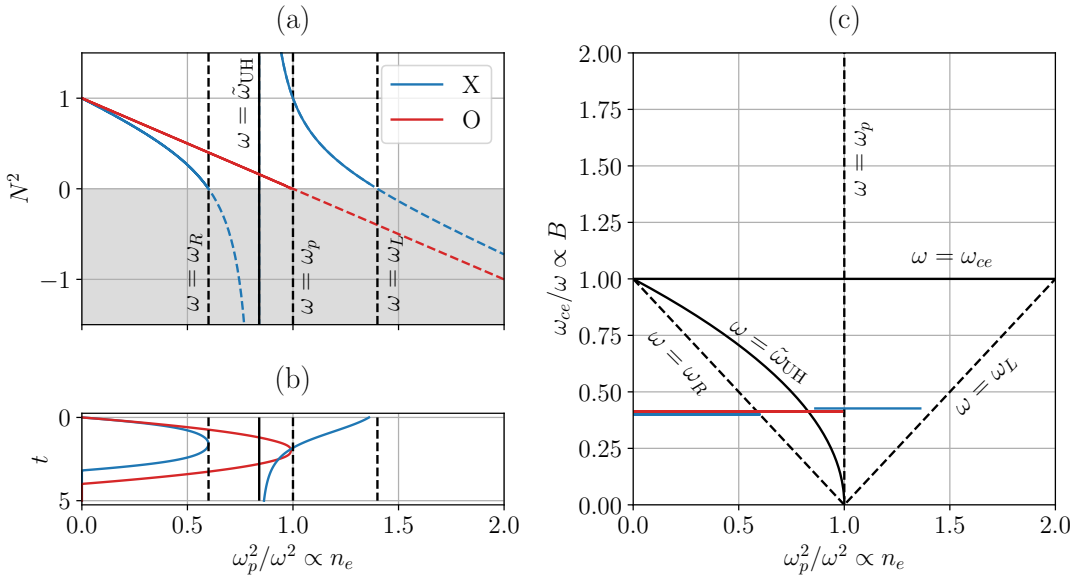


Figure 5.1: $\theta = 90^\circ$. Results from ray tracing using the cold plasma dispersion relation, eq. (2.20 AAH), with an angle of 90° to a constant magnetic field. (a) Plot of $N^2 = c^2 k^2 / \omega^2$ vs. ω_p^2 / ω^2 , (b) ray traces as a function of time, (c) CMA diagram with traces. Red curves represent the O-mode and blue curves the X-mode. The colored dashed curves are the exact result of solving the dispersion relation eq. (2.20 AAH), while the colored solid curves are results of ray tracing. Dashed black lines indicate cutoffs and solid black lines resonances. The gray background indicates the evanescent region.

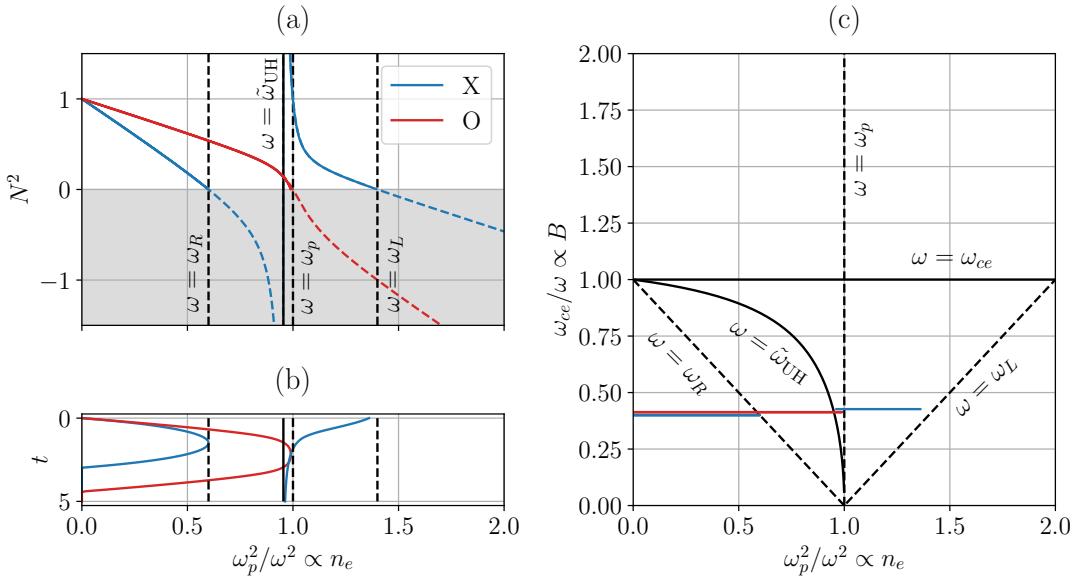


Figure 5.2: $\theta = 30^\circ$. Results from ray tracing using the cold plasma dispersion relation, eq. (2.20 AAH), with an angle of 30° to a constant magnetic field. See caption to Fig. 5.1.

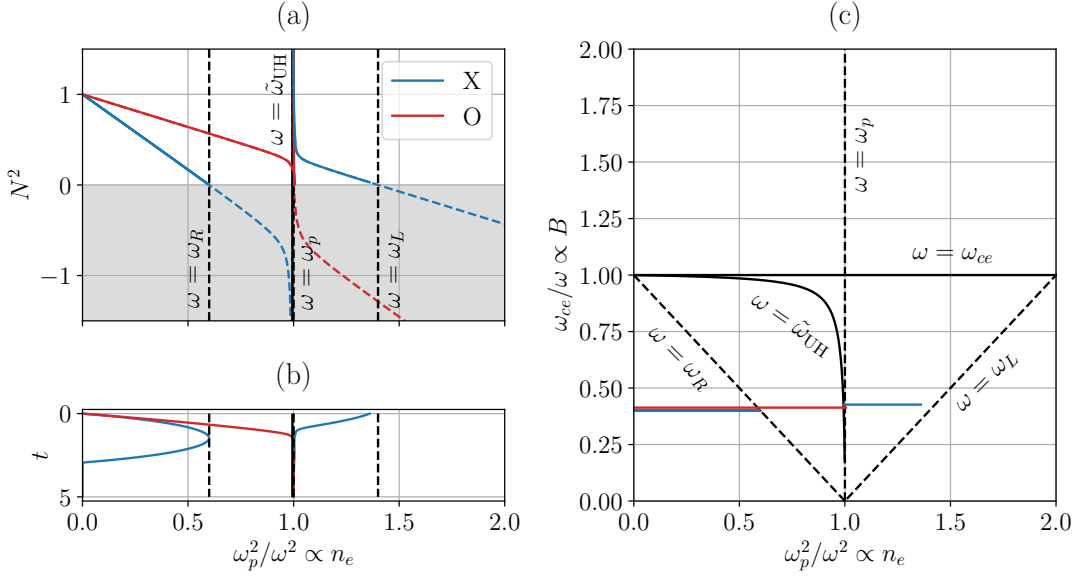


Figure 5.3: $\theta = 10^\circ$. Results from ray tracing using the cold plasma dispersion relation, eq. (2.20 AAH), with an angle of 10° to a constant magnetic field. See caption to Fig. 5.1.

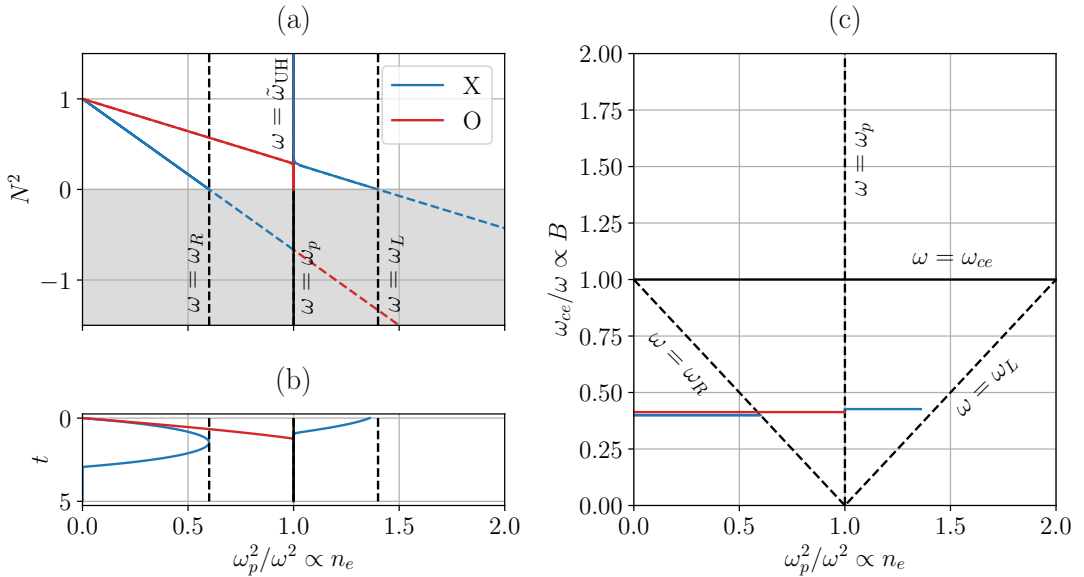


Figure 5.4: $\theta = 0^\circ$. Results from ray tracing using the cold plasma dispersion relation, eq. (2.20 AAH), with an angle of 0° to a constant magnetic field. See caption to Fig. 5.1.

5.2 Airy's Equation (O-mode perpendicular to \mathbf{B}_0)

In one dimension, the simple case depicted on fig. 5.1 of an electromagnetic O-mode wave propagating perpendicularly to \mathbf{B}_0 has the simple wave equation in ω -space (see e.g. Ref. [5, p. 29] and compare with eq. (2.29b)):

$$\left[1 - \frac{n_e(x')}{n_c} + \frac{c^2}{\omega^2} \partial_{x'}^2\right] E(x', \omega) = 0 \quad (5.1)$$

where x' is the position and $n_c = \epsilon_0 m_e \omega^2 / (e^2)$ is the critical density (i.e. the density where the plasma frequency ω_p equals the frequency ω of the electromagnetic (EM) wave). The O-mode has a cutoff where $n_e(x') = n_c$ such that the dispersion relation must have $k \rightarrow 0$ to be satisfied. As I showed on fig. 5.1 such a cutoff is a reflection point. Since the eikonal parameter from eq. (4.21) goes to infinity when $k \rightarrow 0$ this is a classic example of a caustic where the GO approximation breaks down. This type of caustic is called a fold caustic [5, 7]. Assuming the density reaches the critical density at $x' = x_c$, I may approximate the density profile close to the caustic linearly:

$$n_e(x') \approx n_c \left[1 + \frac{x' - x_c}{L} \right], \quad \text{where } L := \frac{n_c}{\partial_{x'} n_e(x_c)}, \quad n_e(x_c) = n_c. \quad (5.2)$$

To non-dimensionalize the problem define $x := (x' - x_c)/\ell$ and use $\partial_{x'} = \ell^{-1} \partial_x$. Similar to Ref. [12], I then obtain the scaled and translated non-dimensionalized position:

$$x := \frac{x' - x_c}{\ell}, \quad \text{where } \ell := \left(\frac{c^2 L}{\omega^2} \right)^{1/3} \quad (5.3)$$

The wave equation is then:

$$\partial_x^2 E(x) - x E(x) = 0, \quad (5.4 \text{ Ai})$$

where I suppressed the frequency-dependence. This is the Airy equation, which occur naturally in many physics problems. For instance in quantum mechanics, where the GO approximation is more commonly known as WKB, a fold caustic of exactly the same structure as the O-mode cutoff is sometimes spoken of as a "turning point" between the classical and non-classical region of a potential barrier (see Ref. [6, Ch. 9]). Note, with the variable transformation the caustic has been translated to $x = 0$. Since eq. (5.4 Ai) is a second-order differential equation it has two linearly independent basis solutions: $\text{Ai}(x), \text{Bi}(x)$. Both are special cases of the modified Bessel functions which are part of the larger family of hypergeometric functions (Ref. [36]). The solution to eq. (5.4 Ai) is a linear combination of these two, but since $\text{Bi}(x)$ diverges for $x \rightarrow \infty$ the solution I am interested in is the Airy function of the first kind. Up to a normalization constant, the solution therefore is:

$$E(x) = \text{Ai}(x). \quad (5.5)$$

Numerous methods exists for evaluating $\text{Ai}(x)$ in different regimes: Power series for small $|x|$, asymptotic expansions for large $|x|$ and steepest descent contour integrals for intermediate values, see Refs. [36] and [37, Appendix A.3]). These methods are implemented in many standard libraries such as SciPy's Special functions library in Ref. [38] which is the one I used to show the exact solution on fig. 5.5 (b). For this reason, the problem is a good benchmark for ray tracing methods (see Refs. [11, 12, 5]).

5.2.1 Integral Representation and Asymptotic Approximation

It is possible to get an integral representation of $\text{Ai}(x)$ by Fourier transforming the Airy equation, but one should be careful with the underlying assumptions when doing so. Assume $E(x)$ can be represented as an inverse Fourier transform with the definition in (3.21 FT):

$$E(x) = \int_{\mathcal{C}_0} \frac{dk}{2\pi} \tilde{E}(k) e^{ikx} \quad (5.6)$$

Note that I have deformed the integral over the real axis to a yet undetermined complex contour. With this, I obtain

$$\partial_x^2 E(x) = \int_{\mathcal{C}_0} \frac{dk}{2\pi} \tilde{E}(k) \partial_x^2 e^{ikx} = -k^2 \int_{\mathcal{C}_0} \frac{dk}{2\pi} \tilde{E}(k) e^{ikx}, \quad (5.7)$$

$$-xE(x) = - \int_{\mathcal{C}_0} \frac{dk}{2\pi} x \tilde{E}(k) e^{ikx} = [i\tilde{E}(k) e^{ikx}] \Big|_{\partial\mathcal{C}_0} - i \int_{\mathcal{C}_0} \frac{dk}{2\pi} e^{ikx} \partial_k \tilde{E}(k), \quad (5.8)$$

where $\partial\mathcal{C}_0$ is the boundary of the contour at $|k| \rightarrow \infty$. Assuming that I can choose the contour such that the boundary contribution of the partial integration vanishes, the Airy equation is simplified to an algebraic equation in k -space which is easily solved:

$$\int_{\mathcal{C}_0} \frac{dk}{2\pi} e^{ikx} [-k^2 - i\partial_k] \tilde{E}(k) = 0 \Leftrightarrow \tilde{E}(k) = \tilde{E}_0 e^{\frac{i}{3}k^3}. \quad (5.9)$$

An integral representation of the Airy function therefore is:

$$\text{Ai}(x) = \frac{1}{2\pi} dk \int_{\mathcal{C}_0} e^{i(kx + \frac{1}{3}k^3)}. \quad (5.10)$$

It should be noted that depending on the contour, \mathcal{C}_0 , the integral above may actually evaluate to either $\text{Ai}(x)$, $\text{Bi}(x)$ or a linear combination of these. Since the integrand is analytic, the contour deformation is valid if the boundary term vanishes. For this to happen I must have $\text{Im}\{k^3\} > 0$ which is satisfied in three regions of the complex plane where $\sin(3\arg[k]) > 0$ or $\arg[k] \in [0, \frac{\pi}{3}], [\frac{2\pi}{3}, \frac{3\pi}{3}]$ or $[\frac{4\pi}{3}, \frac{5\pi}{3}]$. Therefore the complex contour should exit the complex plane in these regions. An asymptotic approximation to the integral is obtained with the stationary phase method which assumes that the main contribution comes from the saddle points $k_* = \pm\sqrt{-x}$ where the phase is stationary, i.e. $\partial_k(kx + \frac{1}{3}k^3) \Big|_{k_*} = 0$. I will not go into further details with this, but simply state the asymptotic results (see Ref [37, sec. A.3], Ref. [5, p. 415] or Ref. [36]):

$$\text{In limit } x \ll -1 \quad \text{Ai}(x) \approx \pi^{-1/2} |x|^{-1/4} \sin\left(\frac{2}{3}|x|^{3/2} + \frac{\pi}{4}\right). \quad (5.11)$$

$$\text{In limit } x \gg 1 \quad \text{Ai}(x) \approx \frac{1}{2}\pi^{-1/2} x^{-1/4} e^{-2/3x^{3/2}}. \quad (5.12)$$

Evidently, the above approximations diverge when $x \rightarrow 0$ and therefore has the same problem as the eikonal approximation. In fact it can be shown that the asymptotic forms are exactly the solutions within the eikonal approximation [6, 12]. I shall now show this eikonal result numerically with the GO method. Note however that the ray tracing equations, eq. (4.39) only give solutions within the non-evanescent/classical region.

5.2.2 Ray Tracing Airy's Equation

Before presenting the numerical result of tracing Airy's Equation I will quickly derive the ray trajectory analytically as is also done in e.g. [7, p. 153]. From eq. (5.4 Ai) I obtain the dispersion symbol¹

$$\mathcal{D}(x, k) = -k^2 - x. \quad (5.13)$$

This gives the ray equations:

$$\partial_\tau x = -\partial_k \mathcal{D} = 2k, \quad \partial_\tau k = \partial_x \mathcal{D} = -1.$$

The solution of this ODE system is:

$$\mathbf{z}(\tau) = \begin{pmatrix} x(\tau) \\ k(\tau) \end{pmatrix} = \begin{pmatrix} -(k_0 - \tau)^2 \\ k_0 - \tau \end{pmatrix}, \quad (5.14)$$

where $k_0 = \sqrt{-x_0}$ is determined by the initial value of $x_0 < 0$. Thus, the solution is a parabola in phase space.

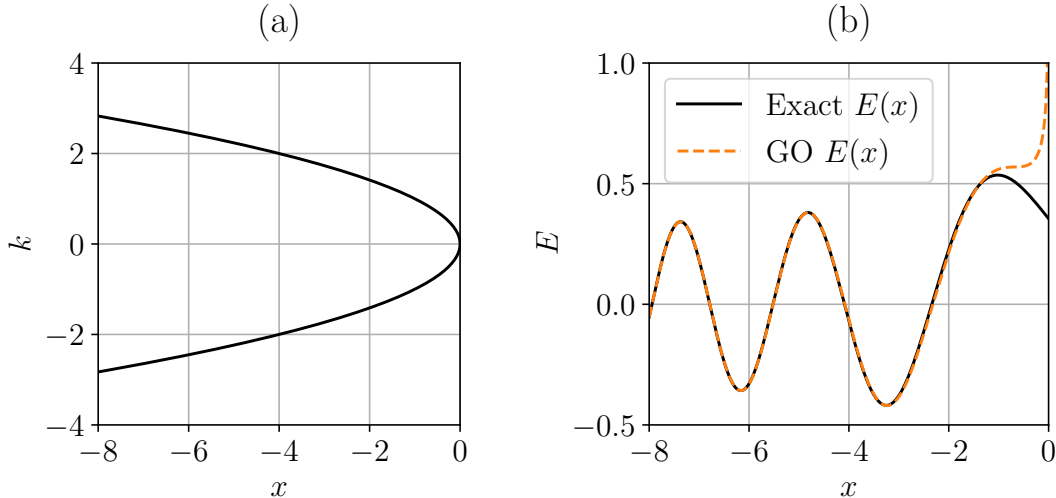


Figure 5.5: Solutions to Airy's Equation, eq. (5.4 Ai), here interpreted as an O-mode being reflected on a linear plasma density. (a) Ray path in phase space which in this 1D example constitutes the ray manifold. The ray starts at $x_0 = -8$ and $k = \sqrt{8}$ and is reflected at the caustic, and the ray tracing was automatically stopped when returning to the starting position. (b) Reconstructed wave field in position space within the eikonal approximation of GO. For comparison, I have also included the exact wave function solution given by Airy's function.

5.2.3 Numerical Results within GO for Airy's Equation

On fig. 5.5 I have shown the result from applying GO to the Airy problem. The coordinates are non-dimensionalized according to eq. (5.3) such that the plasma density is linearly increasing for increasing x and $x = 0$ is the location of the critical density where $\omega = \omega_p$. On fig. 5.5 (a) I have shown the ray trajectory in (x, k) space. Since the problem is one

¹My sign on \mathcal{D} is reversed compared to [7], but so is also the sign in my ray equations eq. (4.39). Reversing the sign in only one of these equations corresponds to a time reversal.

dimensional, the phase space is two dimensional. On fig. 5.5 (a) we see how the ray starts with positive k at $x = -8$, whereafter it propagates forward until k vanishes at the critical density at $x = 0$. As is also the case on fig. 5.1 the O-mode is then reflected after which the ray propagates back to the initial position. The ray tracing was automatically stopped when the ray returned to the initial position. On fig. 5.5 (b) I have shown the exact Airy function together with the approximate solution obtained from eq. (4.50) within GO. The GO approximation gives accurate results away from the cutoff, but unfortunately it clearly diverges at $x = 0$. The divergence is problematic from a physical viewpoint since it gives an infinite energy of the electromagnetic wave which of course is unrealistic. As discussed in section 4.3.2 the culprit behind the diverging wave field can be found on fig. 5.5 (a). The ray manifold plotted on fig. 5.5 (a) (i.e. the ray trajectory) has an infinite slope $\partial_x k = \dot{k}/\dot{x} \rightarrow \infty$ at $x = 0$ and therefore the projection of the manifold becomes singular at this point (here a dot indicates differentiation with respect to the time parameter τ_1). This is also reflected in the Jacobian $j = \dot{x}$ which vanishes at $x = 0$ and therefore causes the envelope of eq. (4.45) to diverge.

5.3 Weber's Equation (Quantum harmonic oscillator (QHO))

This next example is the equation governing the QHO. As is well-known in introductory quantum mechanics, a particle trapped in a one-dimensional harmonic potential will obey the Schrödinger equation [6]:

$$\hat{H} |\psi\rangle = \frac{1}{2m} \left[\hat{p}^2 + (m\omega \hat{q})^2 \right] |\psi\rangle = \varepsilon |\psi\rangle, \quad (5.15)$$

where m is the particle mass, ω the oscillation frequency, ε the eigenenergy, \hat{q} is the position operator and

$$\hat{p} = -i\hbar \int dq |q\rangle \partial_q \langle q|$$

is the momentum operator. As is customary (see e.g. Ref. [6, p. 48] or Ref. [14, p. 18]) I non-dimensionalize the problem by introducing the harmonic oscillator length, ℓ , the corresponding non-dimensionalized position operator, \hat{x} , momentum operator, \hat{k} , and non-dimensionalized energy E :

$$\ell := \sqrt{\frac{\hbar}{m\omega}}, \quad \hat{x} := \frac{\hat{q}}{\ell}, \quad \hat{k} := \frac{\hat{p}}{\hbar/\ell}, \quad E := \frac{\varepsilon}{\hbar\omega}$$

Thereby, Schrödinger's equation, eq. (5.15), becomes:

$$(2E - \hat{k}^2 - \hat{x}^2) |\psi\rangle = |0\rangle \quad (5.16 \text{ We})$$

Equation (5.16 We) is known as Weber's equation (Ref. [7]). With a suitable dimensionialization, Weber's equation may also describe an EM O-mode wave trapped in a 1D parabolic plasma density profile. The exact solution can be found e.g. algebraically in second quantization by using creation/annihilation operators or analytically through the power series method and the solution can be expressed in Hermite polynomials [6, p. 52]:

$$\psi_\nu(x) := \langle x | \psi_\nu \rangle = \pi^{-1/4} \frac{1}{\sqrt{2^\nu \ell^\nu \nu!}} H_\nu(x) e^{-x^2/2}, \quad \nu \in \mathbb{N}_0. \quad (5.17)$$

Here the wave function has been normalized with respect to the usual L^2 inner product in q -space, eq. (3.2 $\|\cdot\|_{L^2}$). As indicated, the solutions are quantized with $\nu \in \mathbb{N}_0$ which

can be derived as a result of the normalization requirement. The corresponding quantized energies are given by:

$$E = \nu + \frac{1}{2}, \quad \text{or} \quad \varepsilon = \hbar\omega \left(\nu + \frac{1}{2} \right). \quad (5.18)$$

5.3.1 Ray Tracing Weber's Equation

From Weber's Equation, eq. (5.16 We), we have the dispersion symbol:

$$\mathcal{D}(x, k) = -k^2 - x^2 + 2E. \quad (5.19)$$

Clearly, $\mathcal{D}(x, k) = 0$ is satisfied on a circle of radius $\sqrt{2E}$ in (x, k) -space. This can also be seen from the ray equations eq. (4.39):

$$\partial_\tau x = -\partial_k \mathcal{D} = 2k, \quad \partial_\tau k = \partial_x \mathcal{D} = -2x$$

With the initial condition $x(0) = \sqrt{2E}$, the solution to the ray equations is:

$$\mathbf{z}(\tau) = \begin{pmatrix} x(\tau) \\ k(\tau) \end{pmatrix} = \sqrt{2E} \begin{pmatrix} \cos 2\tau \\ -\sin 2\tau \end{pmatrix}. \quad (5.20)$$

It is indeed a periodic circle motion in phase space as one would also expect classically from a harmonic oscillator.

5.3.2 Numerical Results within GO for Weber's Equation

On fig. 5.6 I show the results from ray tracing and field reconstruction for Weber's equation, eq. (5.16 We) within the GO approximation. As was also the case for the Airy problem, the ray tracing only gives solutions in the classical (non-evanescent) region. I have shown the solutions for the ground state and first three excited states of the QHO. The ray trace results are shown on the left side of fig. 5.6. As expected from eq. (5.20) the ray phase space trajectory is period. The ray tracing was stopped automatically after reaching one cycle. The different energy levels corresponds to different harmonics. As the energy E is increased, the particle gets higher up in the harmonic potential well and we therefore see an increase in the radius $R = \sqrt{2E}$ of the phase space trajectory. In the GO solution we can identify the familiar properties of the exact solutions to the QHO: The wave functions are alternately even and odd and as the energy is increased, the number of nodes increments by 1. The GO solution matches well with the exact result away from the turning points, but clearly the GO field diverges at the caustics, where the projection of the ray manifold to x -space becomes singular. This is clearly not realistic. From a quantum mechanics perspective, this means that the wave functions cannot be normalized and from a plasma physics perspective it implies that the energy of the electric field is not finite.

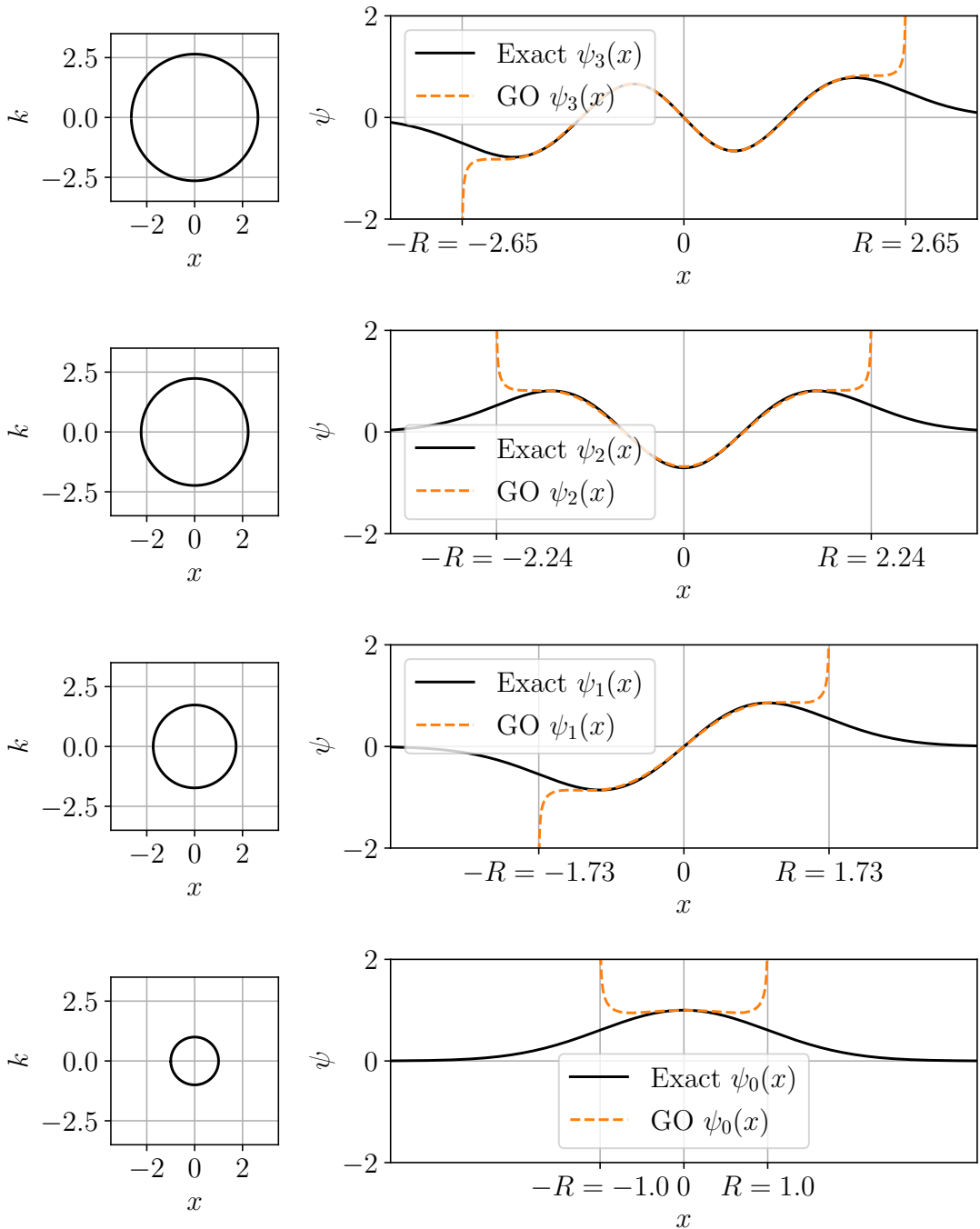


Figure 5.6: Numerical Solutions to Weber's Equation, eq. (5.16 We), for first four orders $\nu = 0, 1, 2, 3$. In quantum mechanics, the orders corresponds to the ground state and first 3 excited states of the QHO. On the left we see the ray paths in phase space which in this 1D example constitutes the ray manifold. The ray path is seen to be periodic in phase space, and the ray tracing was automatically stopped after 1 cycle. On the right, we see the reconstructed wave field in position space within the eikonal approximation of GO. For comparison, I have also included the exact wave function solution given by eq. (5.17) with $\ell = 1$. $R = \sqrt{2E}$ denotes the radius of the phase space trajectory.

5.4 Two-dimensional plasma

Now that I have presented some 1D examples of ray tracing and field reconstruction in the GO approximation, I believe it is time to show a 2D example. The following example is similar, but not identical, to Ref. [5, Ch. 4]. The example is well-suited to showcase GO in more dimensions and presents core ideas from Ref. [5, Ch. 4] on how to visualize the dispersion surface and ray manifold when the phase space is more than two dimensional. In my example, I considered an O-mode launched from vacuum onto a plasma blob with the "circular" density profile plotted on fig. 5.7. The shown density profile is an azimuthally symmetric Gaussian given by the equation

$$n_e(\mathbf{x}) = n_c \exp\left(-\frac{1}{20}(x_1^2 + x_2^2 - 5^2)\right)$$

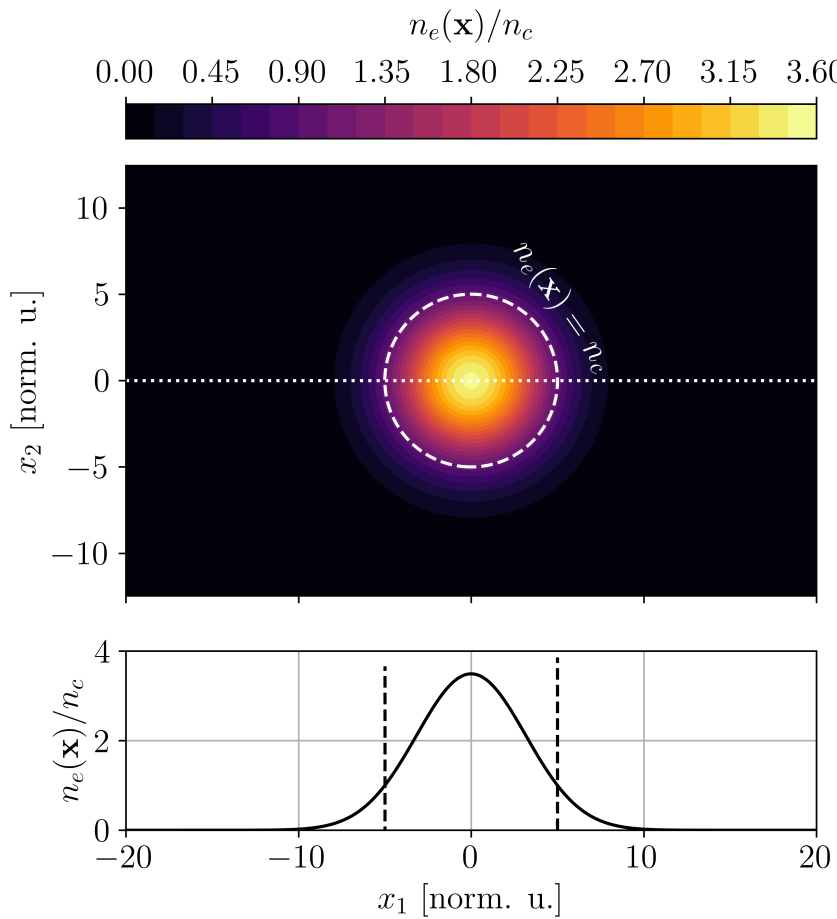


Figure 5.7: Illustration of azimuthally symmetric density profile. The density is normalised with the critical density. The dashed circle indicates the cutoff (where the density equals the critical density). The dotted line indicates a cross section along which the 1D density profile is shown in the bottom row of the figure. The cutoff position is also indicated on this cross section density profile by dashed vertical lines.

The critical density is reached on a circle of radius 5 as indicated by the white dashed line on fig. 5.7. Since, we have more than one dimension, instead of launching a single ray, I now launch a family of rays with a range of different transverse initial coordinates, x_2^0 .

All rays were launched from a starting plane in vacuum with initial coordinate $x_1^0 = -20$. The ray family was initialised with the simple boundary condition: $\phi(-20, \mathbf{x}_\perp^0) = 1$. As a side note: In my numerical implementation, I actually treated the problem as three dimensional (so n_e was made invariant in the x_3 -direction and one may therefore think of the density profile contours as cylinders rather than circles). Thus, I carried out the ray tracing and field reconstruction in three dimensions, but since the symmetry renders the x_3 -direction irrelevant, I only launched rays with initial coordinate $x_3^0 = 0$ (i.e. the ray family did not "scan" the x_3 -direction). In the following analysis, I will however treat the problem as two-dimensional (as it is) and ignore the third dimension. The trajectories of some of the rays are shown on top of the density profile in position space on fig. 5.8. As a first sanity check I can see that the "top" and "bottom" rays with $|x_2^0| \gtrsim 13$ never change direction, since the density far away from the plasma blob is practically zero and therefore the rays continue unaffected. Meanwhile the ray at the center with $x_2^0 = 0$ is reflected directly backwards exactly at the critical density just like I found in 1D in figs. 5.1 and 5.5. The intermediate rays meet the perturbation at an angle and are therefore partly refracted (away from the density gradient) instead of being perfectly reflected. A classical analogy would be rolling balls changing direction after hitting a circular symmetric bump.

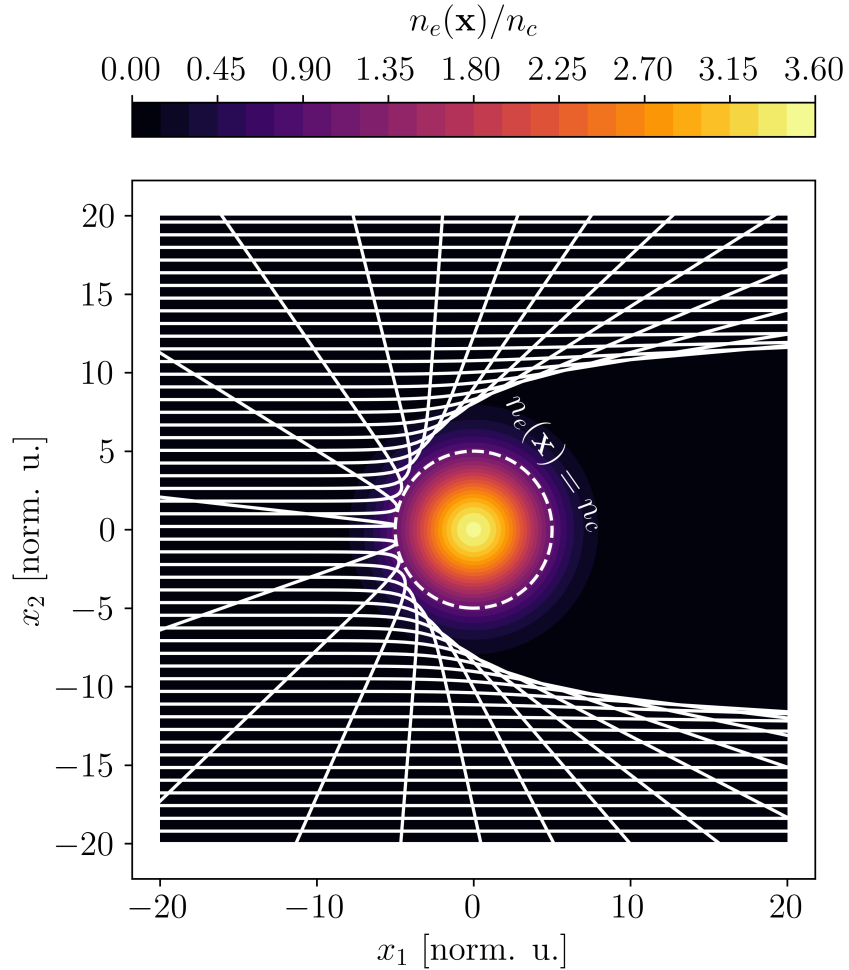


Figure 5.8: Azimuthally symmetric density profile overlapped with ray trajectories in the $(x_1, x_2, x_3 = 0)$ plane. The example is similar to Ref. [5, Figure 4.2, p. 160].

Even though the rays never cross in phase space, they may cross in position space as they clearly do on fig. 5.8. This is unfortunate since the crossing of rays indicates that the projection of the ray manifold is singular somewhere as discussed in section 4.2. To visualize the rays without crossings I should really have shown the trajectories in phase space, which in a 2D problem like this is 4D. Of course, the problem is that I have no means of visualizing a four-dimensional space. Fortunately, I do not need to consider the entire phase space to get a global view of the problem; Since the dispersion symbol is a function of 4 variables, its' level set $\mathcal{D}(\mathbf{x}, \mathbf{k}) = 0$ is three-dimensional. This level set is the dispersion surface and all rays must live within it. Furthermore, the ray manifold is only two-dimensional meaning it can be parametrized by two coordinates $\tau = (\tau_1, \tau_2)$. Here, I let the first coordinate be the "time parameter" τ_1 , whereas the second coordinate is the initial transverse position: $\tau_2 = x_2^0$. I can thereby obtain a *rendering* of the ray manifold² by drawing a grid spanned by (τ_1, τ_2) -coordinates. In fig. 5.9 I show the ray manifold rendered in this way in the 3D space of coordinates (x_1, x_2, k_1) . The black lines on the ray manifold grid have constant τ_1 -value and the grey lines have constant τ_2 value and together they make a coordinate web spanning part of the manifold.

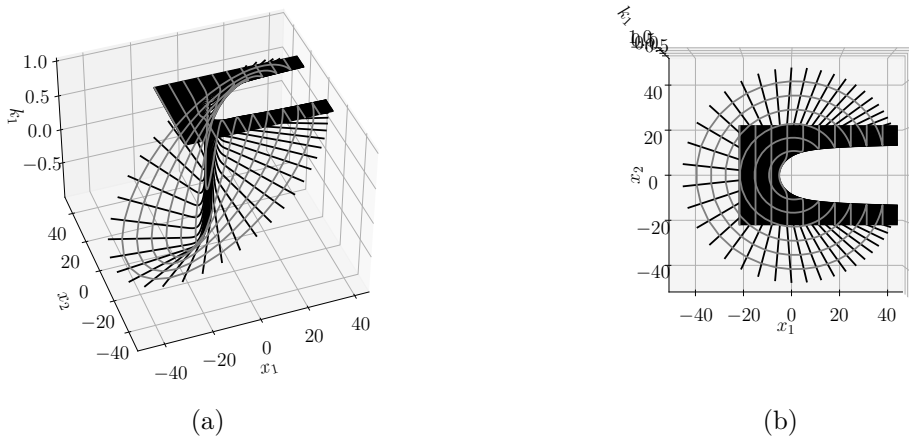


Figure 5.9: Two views from different angles of the ray manifold in (x_1, x_2, k_1) -space from the example in figs. 5.7 and 5.8. Each solid black line is a trajectory of a ray launched with a unique $\tau_2 = x_2^0$ position and $x_1^0 = -20$. The transverse grey lines are "equi-temporal" lines (i.e. lines of equal time parameter τ_1). In the vacuum region the equi-temporal lines correspond to "lines of constant phase of the electric field". The illustration is inspired by Ref. [5, Figure 4.3, Ch. 4].

On fig. 5.9 we see that the ray manifold no longer crosses itself when it is plotted in the (x_1, x_2, k_1) space. In Tracy et al.'s nomenclature, the mapping of the ray manifold onto (x_1, x_2, k_1) is called a *faithful rendering* if it preserves the fact that no rays cross. In other words a *faithful rendering* needs to be injective. As a contra example, a rendering in (x_1, x_2, k_2) space would not be faithful, since all rays have the same k_2 coordinate initially. Furthermore, a three-dimensional space such as (x_1, x_2, k_1) which allows a faithful rendering is called a *room*, (see Ref. [5, p. 163]).

It is actually a clever coincidence following from the choice of initial conditions and geometry of the problem, that (x_1, x_2, k_1) space constitutes a room in this case. Tracy et al. gives more details on how to find the room in general, but for our purpose, I'm satisfied

²The term *rendering* is borrowed from Tracy et al., see footnote [5, p. 158].

with using the room provided in fig. 5.9. In any case, it is clear that fig. 5.9 provides a nice global overview of the problem. At the top plane rays are coming in from vacuum with $k_1 > 0$. The rays far away from the plasma continue unaffected in vacuum. For the rays meeting the plasma, k_1 is reduced as the rays meet the plasma density blob. Some, but not all rays, obtain negative k_1 values such that they propagate backwards in the $-x_1$ -direction after the partial reflection. For each point on the ray manifold, the remaining k_2 coordinate is uniquely given by the constraint of the dispersion relation $\mathcal{D}(\mathbf{x}, \mathbf{k}) = 0$. The fact that $\mathcal{D}(\mathbf{x}, \mathbf{k}) = 0$ has one and only one solution for each point follows from the properties of a room [5].

In the 1D case of Airy's Equation, fig. 5.5, I found the wavefield to diverge when the Jacobian determinant of the ray manifold vanished and the projection of the manifold onto position space thereby became singular. Exactly the same happens here in this 2D example. On fig. 5.9 it is seen how the ray manifold gets an infinite gradient $\|\partial_{\mathbf{x}} \mathbf{k}\| \rightarrow \infty$ at the caustic (i.e. the manifold looks "vertical" in (x_1, x_2, k_1) space). As opposed to the 1D Airy problem, the Jacobian determinant, $j(\boldsymbol{\tau}) = \det \partial_{\boldsymbol{\tau}} \mathbf{x}(\boldsymbol{\tau})$ now depends on two coordinates, τ_1 and τ_2 , and $j = 0$ exactly at the caustic where the envelope approximation of eq. (4.45) therefore diverges.

Finally, on fig. 5.10 I present the electric field obtained from the ray manifold and boundary condition $\phi(-20, \mathbf{x}_\perp^0) = 1$ using eq. (4.50). For good measure I stress, that the GO algorithm only needs information of the ray family trajectories and the transverse boundary condition to approximate the field in the entire domain. In this particular example the ray manifold only has an incoming and outgoing branch separated by the caustic curve where $j = 0$. To construct the electric field I superposed the contributions from both branches as described in section 4.4.3. The contributions are both seen on fig. 5.10. fig. 5.10a shows the incoming field, fig. 5.10b the outgoing field, and fig. 5.10c the sum of the two contributions. The reason for the "pixelation" of the boundary between the illuminated and shadow region is to be found in my method of interpolation where I, as explained in section 4.4.3, apply a window function to avoid interpolating the electric field across the shadow region. Within GO, the field behaves reasonable away from the caustic. On fig. 5.10a I see the expected incoming plane waves propagating towards the plasma from vacuum. When the waves meet the plasma they are scattered in close to perfect circles from the obstacle, reminiscent of the Huygens-Fresnel principle [39, p. 115]. As expected, the electric field clearly diverges close to the caustic where the Jacobian determinant $j = 0$. On fig. 5.10d I have plotted the electric field along $x_2 = 0$ and I observe the same divergence problem as for the Airy function on fig. 5.5. There is no loss mechanism in the current formulation of GO which I used to generate fig. 5.10. Therefore it may be surprising that the outgoing field seems to be weaker in amplitude than the ingoing. My current hypothesis is that this is also due to the divergence of the caustic which "steal" some of the total energy to produce the high E -field amplitude at the caustic curve.

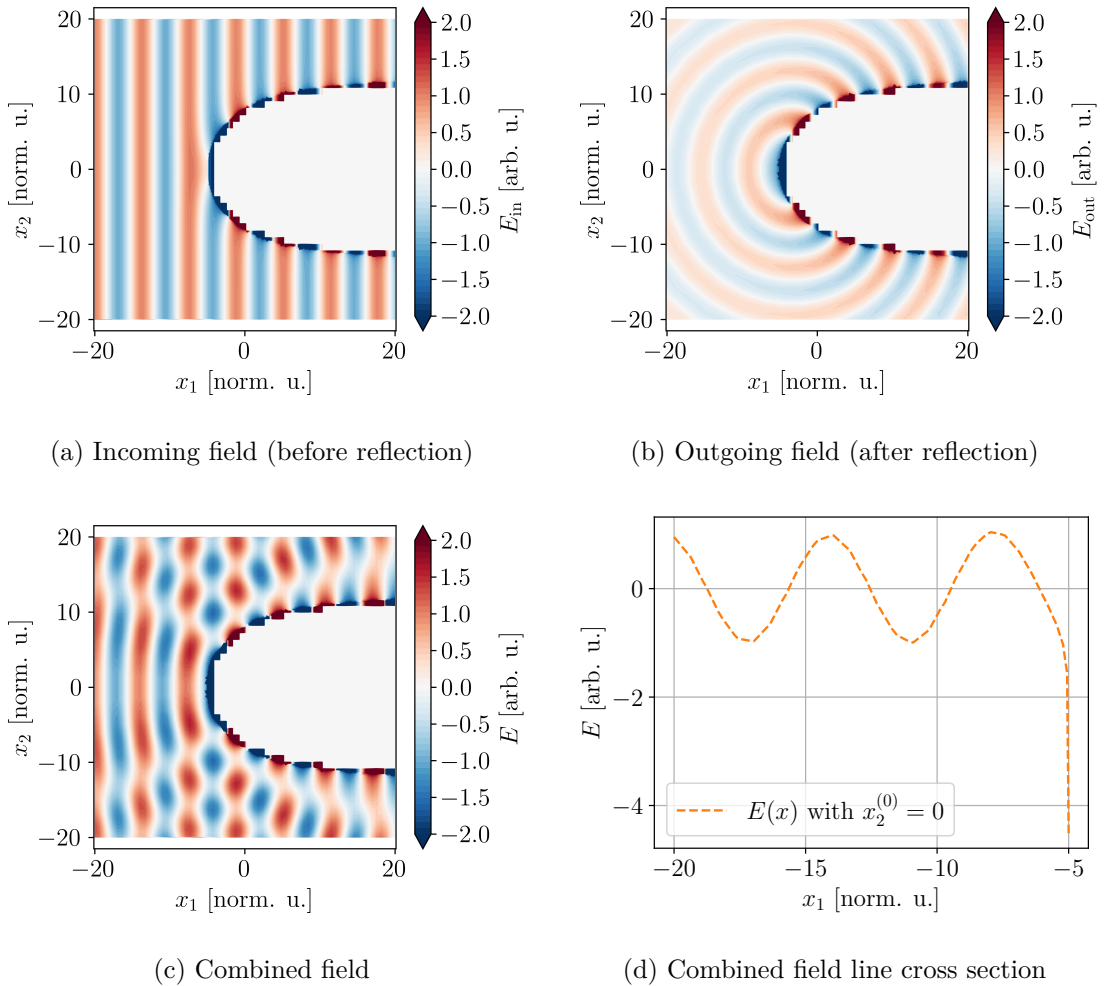


Figure 5.10: Field reconstruction in the example with a circular density profile (see Fig. 5.7) with an incoming plane wave O-mode.

6 Metaplectic Geometrical Optics

Whether you can observe a thing or not depends on the theory which you use. It is the theory which decides what can be observed.

Albert Einstein, 1926

By now, with the examples covered in chapter 5 and the discussion of caustics in chapter 4 it should be evident that a systematic approach for dealing with caustics is seriously needed. Such a systematic theory for reinstating the validity of the GO approximation in caustic regions has recently been developed and presented in Refs. [10, 11, 12, 7, 8] in the form of the MGO model. In this chapter I shall reiterate parts of the derivation of the MGO method based on these references, in particular Refs. [7, 11].

6.1 Fourier Transformation as a Strategy for Treating Caustics

The fact that the eikonal approximation breaks down at caustics has of course been recognized from the get go of the development of the WKB theory. Therefore it should come as no surprise that several schemes had already been invented to attempt dealing with caustics in a systematic manner previous to the MGO framework. A widely used strategy is that of Maslov's method developed by Kelle and Maslov among others (see Refs. [5, p. 185], [11, 9] who points to the original Refs. [40, 41]). Before explaining the theory of MGO I shall briefly explain the core idea of this method.

In section 4.2 I discussed how caustics are due to the projection of the ray manifold onto \mathbf{x} -space being ill-defined at points where the Jacobian is singular:

$$j(\tau) = \det \partial_\tau \mathbf{x}(\tau) \rightarrow 0 \quad \text{or} \quad \det \partial_{\mathbf{x}} \mathbf{k}(\mathbf{x}) = \det \partial_{\mathbf{x}} \partial_{\mathbf{x}} \theta(\mathbf{x}) \rightarrow \infty. \quad (6.1)$$

To avoid this problem we need to represent the wave field in a basis that does not have the projection singularity. The interpretation of the Fourier transform, given in section 3.1.2, as the projection of the wave state vector onto the momentum basis might therefore give a hint to resolving the caustic problem. The core idea is to Fourier transform the eikonal wave field when the ray is close to a caustic, evolve the Fourier transformed field in the caustic region and then transform the field back when exiting the caustic region.

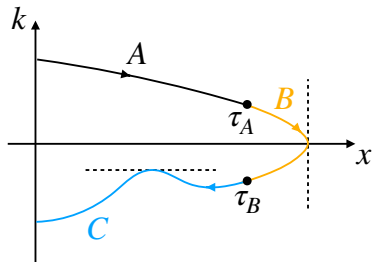


Figure 6.1: Conceptual illustration of ray manifold with a cutoff in region B in x -space and a cutoff in region C in k -space. In Maslov's method the wave field is Fourier transformed at $\tau = \tau_A$, evolved through region B and then inverse Fourier transformed at $\tau = \tau_B$ to avoid the k -space caustic in region C . The dash lines at the cutoffs are the tangent planes, which shows that the slope of the ray manifold goes to infinity in the x - and k -representation respectively.

As a conceptual illustration similar to [11, Figure 2] and [5, Figure 5.3], consider the 1D ray manifold on fig. 6.1. The manifold has a caustic in the B-region at the reflection point where the slope of $k(x)$ goes to ∞ . Let $\psi(x), \tilde{\psi}(k)$ denote the eikonal field representation in position and momentum space respectively. Though $\psi(x)$ is not globally well-behaved, it is valid in regions A and C, since there are no singularities when projecting the ray manifold down to x -space in these region. Meanwhile the Fourier transformed field $\tilde{\psi}(k)$ will be well-defined in region B. However, just like $\psi(x)$ diverges when there are projection singularities onto x -space, so $\tilde{\psi}(k)$ will misbehave when the k -space projection of the ray manifold is ill-defined. Therefore $\tilde{\psi}(k)$ will not be defined closed to the k -space caustic in region C. As I shall soon show, the GO equations can be formulated in momentum space, and $\tilde{\psi}(k)$ may therefore be evolved through region B with equations similar to eqs. (4.39), (4.45) and (4.51). The overall strategy in Maslov's method would therefore in this case be:

1. Evolve an incoming eikonal field matching the boundary condition (BC) through region A using the GO equations, eqs. (4.39), (4.45) and (4.51).
2. At some τ_A , when the ray is close to a caustic in x -space (where $\dot{x} = 0$), raise the "caustic alarm" and Fourier transform $\psi[x(\tau_A)]$ using the stationary phase approximation (SPA) to obtain $\tilde{\psi}[k(\tau_A)]$.
3. Starting from the BC given by $\tilde{\psi}[k(\tau_A)]$, evolve $\tilde{\psi}(k)$ through region B using GO equations similar to eqs. (4.39), (4.45) and (4.51), but formulated in k -space.
4. At τ_B , when the ray is close to a caustic in k -space (where $\dot{k} = 0$), raise the "caustic alarm" and inverse Fourier transform the field back to $\psi[x(\tau_B)]$ using the SPA.
5. Evolve $\psi(x)$ through region C matching $\psi[x(\tau_B)]$.

The Fourier transformed field is determined from eq. (3.21 FT):

$$\tilde{\psi}(k) = \int dx \phi(x) e^{i(\theta(x) - kx)} \quad (6.2)$$

The SPA assumes that the biggest contribution to this integral comes close the point where the phase, $\theta(x) - kx$, of the exponential has a saddle point x_* . That is:

$$\partial_x(\theta(x) - kx) \Big|_{x=x_*} = 0 \Leftrightarrow k(x_*) = \partial_x \theta(x_*) \quad (6.3)$$

Since, this is the same assumption that lies behind the GO approximation (see eq. (4.18)), the stationary phase criterion is exactly satisfied for points on the ray manifold. Thus, if there exists a τ such that $k = k(\tau)$ then $x_* = x(\tau)$. It can be shown, that the Fourier transformed field within the SPA is (see Ref. [5, eq. (5.20a) and Appendix C.12] and Ref. [11]):

$$\tilde{\psi}[k(\tau)] \approx \tilde{\phi}[k(\tau)] e^{i\tilde{\theta}[k(\tau)]}, \quad \text{where} \quad (6.4)$$

$$\tilde{\phi}[k(\tau)] := \left(\frac{2\pi}{|\partial_x k[x(\tau)]|} \right)^{1/2} \phi[x(\tau)] e^{-i\frac{\pi}{4}\mu(\tau)}, \quad \tilde{\theta}[k(\tau)] := \theta[x(\tau)] - k(\tau)x(\tau). \quad (6.5)$$

Thus, within the SPA the Fourier transformed field is itself eikonal. Note, $\mu(\tau) = \text{sign}(\partial_x k[x(\tau)])$ is the Keller-Maslov index which in 1D is just the sign of the slope $\partial_x k$. Importantly, the SPA has changed the Fourier transformation from an integral transform into a local mapping, $\psi[x(\tau)] \rightarrow \tilde{\psi}[k(\tau)]$ (Ref. [11]). The same happens for the

inverse transform, $\tilde{\psi}[k(\tau)] \rightarrow \psi[x(\tau)]$. These facts are crucial for Maslov's method. The SPA result of eq. (6.4) breaks down at the caustic where $\partial_x k \rightarrow \infty$. The caustic alarms τ_A, τ_B, \dots should therefore be chosen sufficiently far from the caustics such that the SPA is well-defined.

From the $\psi_A, \tilde{\psi}_B, \psi_C$ fields, Maslov's method can reconstruct $\psi(x)$ throughout the entire domain, but in general it requires further analysis to find the so-called normal forms that yields locally valid approximations near the caustic (see Ref. [5]). The method has been important for the theoretical understanding of caustics and it is for instance implemented in the ray tracing algorithm in the MATLAB framework RAYCON developed by Jaun, Tracy, and Kaufman, see Ref. [42]. Nevertheless, Maslov's method is suboptimal, since it is complicated to implement in a manner that does not require external supervision from the user (Ref. [5, p. 187]). Furthermore, there is an arbitrariness in how one should choose the caustic alarm points τ_A, τ_B, \dots to yield accurate results. Finally, in more dimensions, it is not obvious which variables should be Fourier transformed to get rid of the projection singularities (Ref. [7]).

6.2 Symplectic Phase Space Rotations

The Fourier transformation used in Maslov's method can be thought of as being associated with a 90° rotation in phase space. In fact, Fourier transforms are special cases of a larger class of transforms known as metaplectic transforms which are associated with more general transformations of phase space coordinates (x, k) . From this perspective, Maslov's method works because it removes the projection singularity locally by representing the ray manifold in a new rotated phase space: $(X, K) = (k, -x)$. The core idea of the MGO method is to take this geometric solution strategy fully serious: Instead of rotating the phase space coordinates sometimes, MGO proposes to rotate the phase space continually along the ray. Thereby, one can ensure that there are never any local projection singularities in the rotated phase space representation (Ref. [11]). To show how this works in practice, I first need to introduce the theory of symplectic phase space rotations.

Consider linear transformations of phase space coordinates on the general form:

$$\mathbf{z} = \begin{pmatrix} \mathbf{x} \\ \mathbf{k} \end{pmatrix} := \mathbf{S} \mathbf{z} = \begin{pmatrix} \mathbf{A} & \mathbf{B} \\ \mathbf{C} & \mathbf{D} \end{pmatrix} \begin{pmatrix} \mathbf{x} \\ \mathbf{k} \end{pmatrix} = \begin{pmatrix} \mathbf{Ax} + \mathbf{Bk} \\ \mathbf{Cx} + \mathbf{Dk} \end{pmatrix}. \quad (6.6)$$

Here $\mathbf{S} \in \mathbb{R}^{2N \times 2N}$ is a linear transformation matrix written on a block matrix form with $\mathbf{A}, \mathbf{B}, \mathbf{C}, \mathbf{D} \in \mathbb{R}^{N \times N}$. $\mathbf{x}, \mathbf{k} \in \mathbb{R}^N$ are the new transformed phase space coordinates. Only the subset of all linear transformations which preserve Hamilton's equations are worth considering. These are called symplectic or canonical transformations¹ (Ref. [43, 5, 7]). Recall, that Hamilton's ray equations, eq. (4.39), can be written:

$$\dot{\mathbf{z}} = -\mathbf{J}_{2N} \partial_{\mathbf{z}} \mathcal{D}, \quad \mathbf{J}_{2N} := \begin{pmatrix} \mathbf{o}_N & \mathbf{I}_N \\ -\mathbf{I}_N & \mathbf{o}_N \end{pmatrix} \quad (6.7)$$

where the dot is the ∂_{τ_1} derivative, \mathbf{J}_{2N} is the symplectic matrix introduced in eq. (3.28) and the local dispersion symbol \mathcal{D} acts as the Hamiltonian of the system. Note that in my notation (see appendix A.1) I have

$$[\partial_{\mathbf{z}} \mathbf{Z}] = \mathbf{S}^T, \quad \partial_{\mathbf{z}} \mathcal{D} = (\partial_{\mathbf{z}} \mathbf{Z}) \cdot \partial_{\mathbf{z}} \mathcal{D} = \mathbf{S}^T \partial_{\mathbf{z}} \mathcal{D}. \quad (6.8)$$

¹To be precise, the linear symplectic transformations which I consider are a subset of all canonical transformations (Ref. [43]).

Therefore the ray equation in \mathbf{Z} is:

$$\dot{\mathbf{Z}} = \mathbf{S} \dot{\mathbf{z}} = -\mathbf{S} \mathbf{J}_{2N} \mathbf{S}^T \partial_{\mathbf{Z}} \mathcal{D}. \quad (6.9)$$

If the transformation is to be symplectic, the old Hamiltonian \mathcal{D} expressed in the new variables should serve as the new Hamiltonian (Ref. [43, p. 383]). Therefore, comparison with eq. (6.7) shows, that the linear transformation is symplectic if²:

$$\mathbf{S} \mathbf{J}_{2N} \mathbf{S}^T = \mathbf{J}_{2N}. \quad (6.10)$$

Equation (6.10) can be taken as the definition of symplecticity. It is a necessary and sufficient condition for preservation of the equations of motion under the coordinate transformation (Ref. [43]). Numerous properties follow quickly from eq. (6.10):

1. The identity matrix \mathbf{I}_{2N} is symplectic.

2. A symplectic transformation is invertible, since:

$$\det [\mathbf{S} \mathbf{J}_{2N} \mathbf{S}^T] = \det \mathbf{J}_{2N} = 1 \Rightarrow (\det \mathbf{S})^2 = 1. \quad (6.11)$$

3. The inverse of \mathbf{S} is (use that $\mathbf{J}_{2N}^{-1} = -\mathbf{J}_{2N} = \mathbf{J}_{2N}^T$):

$$\mathbf{S}(-\mathbf{J}_{2N} \mathbf{S}^T \mathbf{J}_{2N}) = \mathbf{I}_{2N} \Leftrightarrow \mathbf{S}^{-1} = -\mathbf{J}_{2N} \mathbf{S}^T \mathbf{J}_{2N}. \quad (6.12)$$

4. If \mathbf{S} is symplectic, so is its' inverse \mathbf{S}^{-1} (prove it e.g. by inserting eq. (6.12)):

$$\mathbf{S} \mathbf{J}_{2N} \mathbf{S}^T = \mathbf{J}_{2N} \Rightarrow \mathbf{S}^{-1} \mathbf{J}_{2N} \mathbf{S}^{-T} = \mathbf{J}_{2N}. \quad (6.13)$$

5. The product of two symplectic matrices $\mathbf{S}_1 \mathbf{S}_2$ is also symplectic:

$$\mathbf{S}_1 \mathbf{S}_2 \mathbf{J}_{2N} \mathbf{S}_2^T \mathbf{S}_1^T = \mathbf{S}_1 \mathbf{J}_{2N} \mathbf{S}_1^T = \mathbf{J}_{2N} \quad (6.14)$$

6. If \mathbf{S} is symplectic, so is \mathbf{S}^T :

$$\begin{aligned} \mathbf{S} \mathbf{J}_{2N} \mathbf{S}^T = \mathbf{J}_{2N} \Rightarrow \mathbf{S} \mathbf{J}_{2N} = \mathbf{J}_{2N} \mathbf{S}^{-T} \Rightarrow -\mathbf{J}_{2N} \mathbf{S} \mathbf{J}_{2N} \mathbf{J}_{2N} = -\mathbf{J}_{2N} \mathbf{J}_{2N} \mathbf{S}^{-T} \mathbf{J}_{2N} \Rightarrow \\ \mathbf{S}^T \mathbf{J}_{2N} \mathbf{S} = \mathbf{J}_{2N}. \end{aligned} \quad (6.15)$$

The first five properties show that the set of all linear symplectic transformations form a group (with matrix multiplication as the associative group product operation).

6.2.1 Orthosymplectic Transformations

Now, in this thesis, the transformations I am interested in are rotations. Rotations are characterized by \mathbf{S} being orthonormal, i.e.:

$$\mathbf{S}^T = \mathbf{S}^{-1}. \quad (6.16)$$

A linear transformation where \mathbf{S} is both orthonormal and symplectic is called *orthosymplectic* (Ref. [7]). From eqs. (6.12) and (6.16), orthosymplectic matrices must be on the block form:

$$\begin{aligned} \begin{pmatrix} \mathbf{A}^T & \mathbf{C}^T \\ \mathbf{B}^T & \mathbf{D}^T \end{pmatrix} &= \begin{pmatrix} \mathbf{D}^T & -\mathbf{B}^T \\ -\mathbf{C}^T & \mathbf{A}^T \end{pmatrix} \Leftrightarrow \\ \mathbf{S} &= \begin{pmatrix} \mathbf{A} & \mathbf{B} \\ -\mathbf{B} & \mathbf{A} \end{pmatrix}. \end{aligned} \quad (6.17)$$

²I could have arrived at the same result by demanding that Poisson brackets are invariant under the transformation, see Refs. [43, 5].

From this point and forward, I shall implicitly assume that any \mathbf{S} -matrix I introduce is orthosymplectic and has the block form of eq. (6.17).

The symplecticity of \mathbf{S} , eq. (6.10) and of \mathbf{S}^{-1} gives the following relations for orthosymplectic matrices (Ref. [7]):

$$\mathbf{AB}^T = \mathbf{BA}^T, \quad \mathbf{B}^T \mathbf{A} = \mathbf{A}^T \mathbf{B}, \quad \mathbf{AA}^T + \mathbf{BB}^T = \mathbf{I}_N, \quad \mathbf{A}^T \mathbf{A} + \mathbf{B}^T \mathbf{B} = \mathbf{I}_N \quad (6.18)$$

The relations can be called the orthosymplectic *Luneberg relations* (Ref. [7]).

6.2.2 Generator Formalism

There exists another way of treating symplectic transformations; namely the generator formalism. In this approach the transformation $\mathbf{z} \mapsto \mathbf{Z}$ is represented implicitly by a generating function. Assuming that \mathbf{B} is invertible, the transformation can be represented by the first generating function given by (Ref. [5, Appendix E]):

$$F_1(\mathbf{X}, \mathbf{x}) = -\frac{1}{2}(\mathbf{X}^T \mathbf{AB}^{-1} \mathbf{X} - 2\mathbf{x}^T \mathbf{B}^{-1} \mathbf{X} + \mathbf{x} \mathbf{B}^{-1} \mathbf{Ax}). \quad (6.19)$$

$F_1(\mathbf{X}, \mathbf{x})$ is defined to generate the coordinate transformation via:

$$\partial_{\mathbf{x}} F_1 = \mathbf{k}, \quad \partial_{\mathbf{X}} F_1 = -\mathbf{K}. \quad (6.20)$$

To check that eq. (6.19) satisfies eq. (6.20), the reader may use the following results which follow directly from the orthosymplectic Luneberg relations, eq. (6.18):

$$\mathbf{B}^{-1} = \mathbf{B}^T + \mathbf{B}^{-1} \mathbf{AA}^T, \quad \mathbf{B}^{-T} = \mathbf{B} + \mathbf{AB}^{-1} \mathbf{A}, \quad (\mathbf{AB}^{-1})^T = \mathbf{AB}^{-1}, \quad (\mathbf{B}^{-1} \mathbf{A})^T = \mathbf{B}^{-1} \mathbf{A}.$$

Using this, isolation of \mathbf{k}, \mathbf{K} in the orthosymplectic transformation gives:

$$\mathbf{k} = \mathbf{B}^{-1} \mathbf{X} - \mathbf{B}^{-1} \mathbf{Ax}, \quad (6.21a)$$

$$\mathbf{K} = -\mathbf{Bx} + \mathbf{Ak} = \mathbf{AB}^{-1} \mathbf{X} - (\mathbf{B} + \mathbf{AB}^{-1} \mathbf{A}) \mathbf{x} = \mathbf{AB}^{-1} \mathbf{X} - \mathbf{B}^{-T} \mathbf{x}. \quad (6.21b)$$

Differentiation of F_1 with these relations shows that eq. (6.20) is indeed satisfied. Note, that there exists corresponding mixed variable generators $F_2(\mathbf{K}, \mathbf{x}), F_3(\mathbf{X}, \mathbf{k}), F_3(\mathbf{K}, \mathbf{k})$ for the other set of variable pairs (see Ref. [43, ch. 9]). Also, pay attention to the assumption I made that \mathbf{B} should be invertible for the first generating function to be useful. This assumption turns out to give some difficulties in formulating MGO and it for instance breaks down for the case of the identity transformation.

6.2.3 Orthosymplectic Transformation For Singular \mathbf{B}

In the case where \mathbf{B} is not invertible it is advantageous instead to consider the matrix projection of \mathbf{A} onto the diagonalizing basis of \mathbf{B} . If \mathbf{B} has rank ρ and corank $\varsigma = N - \rho$, it may be decomposed through singular value decomposition (SVD) (Ref. [25, 7]):

$$\mathbf{B} = \mathbf{L}_S \tilde{\mathbf{B}} \mathbf{R}_S^T, \quad \text{where} \quad (6.22)$$

$$\tilde{\mathbf{B}} = \begin{pmatrix} \Lambda_{\rho\rho} & \mathbf{0}_{\rho\varsigma} \\ \mathbf{0}_{\varsigma\rho} & \mathbf{0}_{\varsigma\varsigma} \end{pmatrix}, \quad (6.23)$$

$$\mathbf{L}_S^T \mathbf{L}_S = \mathbf{I}, \quad \mathbf{R}_S^T \mathbf{R}_S = \mathbf{I}. \quad (6.24)$$

where the columns of \mathbf{L}_S and \mathbf{R}_S are the left and right singular vectors and \mathbf{L}_S and \mathbf{R}_S are orthonormal. $\Lambda_{\rho\rho}$ is a diagonal matrix. The index $\cdot_{\mu\nu}$ denotes that the matrix is of

size $\mu \times \nu$. Using the orthosymplectic Luneberg relations it is possible to show that the matrix projection of \mathbf{A} onto the singular vectors is diagonal (Ref. [7]):

$$\tilde{\mathbf{A}} := \mathbf{L}_S^T \mathbf{A} \mathbf{R}_S = \begin{pmatrix} \mathbf{a}_{\rho\rho} & \mathbf{0}_{\rho\varsigma} \\ \mathbf{0}_{\varsigma\rho} & \mathbf{a}_{\varsigma\varsigma} \end{pmatrix}. \quad (6.25)$$

It is possible to say more on the symmetries which $\mathbf{a}_{\varsigma\varsigma}, \mathbf{a}_{\rho\rho}$ satisfies (Ref. [7, p. 44]). However for our purposes, the definitions in eq. (6.23) and eq. (6.25) are sufficient.

6.3 Metaplectic Transforms

For each orthosymplectic transformation $\mathbf{Z} = \mathbf{S}\mathbf{z}$ of phase space coordinates there exists a corresponding transformation of the coordinate operators:

$$\hat{\mathbf{Z}} = \begin{pmatrix} \hat{\mathbf{X}} \\ \hat{\mathbf{K}} \end{pmatrix} = \mathbf{S}\hat{\mathbf{z}} = \begin{pmatrix} \mathbf{A}\hat{\mathbf{x}} + \mathbf{B}\hat{\mathbf{k}} \\ -\mathbf{B}\hat{\mathbf{x}} + \mathbf{A}\hat{\mathbf{k}} \end{pmatrix} \quad (6.26)$$

The transformations of operators can also be facilitated by unitary operators $\hat{M}(\mathbf{S})$ known as metaplectic operators. The unitary requirement means that:

$$\hat{M}(\mathbf{S})\hat{M}^\dagger(\mathbf{S}) = \hat{M}^\dagger(\mathbf{S})\hat{M}(\mathbf{S}) = \hat{1}. \quad (6.27)$$

The metaplectic operator corresponding to the orthosymplectic transformation \mathbf{S} can be defined by the requirement (Ref. [7]):

$$\hat{\mathbf{Z}} = \hat{M}^\dagger(\mathbf{S})\hat{\mathbf{z}}\hat{M}(\mathbf{S}) = \mathbf{S}\hat{\mathbf{z}} \quad (6.28)$$

Written more explicitly this says:

$$\hat{\mathbf{X}} = \hat{M}^\dagger(\mathbf{S})\hat{\mathbf{x}}\hat{M}(\mathbf{S}) = \mathbf{A}\hat{\mathbf{x}} + \mathbf{B}\hat{\mathbf{k}} \quad (6.29a)$$

$$\hat{\mathbf{K}} = \hat{M}^\dagger(\mathbf{S})\hat{\mathbf{k}}\hat{M}(\mathbf{S}) = -\mathbf{B}\hat{\mathbf{x}} + \mathbf{A}\hat{\mathbf{k}}. \quad (6.29b)$$

It can be shown that the metaplectic operators satisfy (Ref. [5, appendix E]):

$$\hat{M}(\mathbf{S}_2)\hat{M}(\mathbf{S}_1) = \hat{M}(\mathbf{S}_2)\hat{M}(\mathbf{S}_1) \quad (6.30)$$

From a group theoretical perspective this shows that the metaplectic operators preserve the group product operation and therefore forms a representation of the symplectic group with all linear symplectic transformations.

The new position and momentum operator of course have corresponding eigenstates. As is done in Ref. [7], I shall temporarily introduce the notation $|\mathbf{x}(\mathbf{y})\rangle$ to denote the eigenstate of $\hat{\mathbf{x}}$ with eigenvalue \mathbf{y} , i.e. $\hat{\mathbf{x}}|\mathbf{x}(\mathbf{y})\rangle$. Similarly, I let $|\mathbf{X}(\mathbf{y})\rangle$ denote the eigenstate of $\hat{\mathbf{X}}$ with eigenvalue \mathbf{y} , i.e. $\hat{\mathbf{X}}|\mathbf{X}(\mathbf{y})\rangle = \mathbf{y}|\mathbf{X}(\mathbf{y})\rangle$. Note, that there in general exists two views on transformations such as those we consider: The *active view* in which the states $|\psi\rangle$ are transformed with respect to fixed coordinates (i.e. fixed projection states $|\mathbf{x}(\mathbf{y})\rangle$) and the *passive view* in which states $|\psi\rangle$ are kept fixed, and the projection states are transformed (see Ref. [43, ch. 9, p. 400] and Ref. [17, ch. 3 and p. 176]):

$$\begin{array}{ccc} \text{active view} & & \text{passive view} \\ |\Psi\rangle = \hat{M}(\mathbf{S})|\psi\rangle & \longleftrightarrow & |\Psi\rangle = |\psi\rangle \\ |\mathbf{X}(\mathbf{y})\rangle = |\mathbf{x}(\mathbf{y})\rangle & & |\mathbf{X}(\mathbf{y})\rangle = \hat{M}^\dagger(\mathbf{S})|\mathbf{x}(\mathbf{y})\rangle \end{array} \quad (6.31)$$

As in Ref. [7] I shall take the passive view. With the projection states I can therefore define the old and new representation of the state $|\psi\rangle$ as:

$$\psi(\mathbf{y}) := \langle \mathbf{x}(\mathbf{y}) | \psi \rangle \quad \text{and} \quad (6.32\text{a})$$

$$\Psi(\mathbf{Y}) := \langle \mathbf{X}(\mathbf{Y}) | \psi \rangle = \langle \mathbf{x}(\mathbf{Y}) | \hat{M}(\mathbf{S}) | \psi \rangle. \quad (6.32\text{b})$$

By inserting the identity $\int d\mathbf{y} |\mathbf{x}(\mathbf{y})\rangle \langle \mathbf{x}(\mathbf{y})|$ (eq. (3.20e)) I get an expression for the transformed representation:

$$\Psi(\mathbf{Y}) = \int d\mathbf{y} U(\mathbf{Y}, \mathbf{y}) \psi(\mathbf{y}), \quad (6.33)$$

where I defined the kernel function $U(\mathbf{Y}, \mathbf{y}) := \langle \mathbf{X}(\mathbf{Y}) | \mathbf{x}(\mathbf{y}) \rangle$. As in Ref. [7], I can obtain a differential equation for U by first noticing that:

$$\begin{aligned} \langle \mathbf{X}(\mathbf{Y}) | \hat{k} | \mathbf{x}(\mathbf{y}) \rangle &= \langle \mathbf{x}(\mathbf{y}) | \hat{k} | \mathbf{X}(\mathbf{Y}) \rangle^* = \left[\langle \mathbf{x}(\mathbf{y}) | \int d\mathbf{y}' |\mathbf{x}(\mathbf{y}')\rangle (-i\partial_{\mathbf{y}'}) \langle \mathbf{x}(\mathbf{y}') | \mathbf{X}(\mathbf{Y}) \rangle \right]^* \\ &= [-i\partial_{\mathbf{y}} U^*(\mathbf{Y}, \mathbf{y})]^* = i\partial_{\mathbf{y}} U(\mathbf{Y}, \mathbf{y}) \end{aligned}$$

Using eq. (6.29a) I therefore have:

$$\begin{aligned} \langle \mathbf{X}(\mathbf{Y}) | \hat{\mathbf{X}} | \mathbf{x}(\mathbf{y}) \rangle &= \langle \mathbf{X}(\mathbf{Y}) | \mathbf{A}\hat{\mathbf{x}} + \mathbf{B}\hat{\mathbf{k}} | \mathbf{x}(\mathbf{y}) \rangle \Leftrightarrow \\ \mathbf{Y} U(\mathbf{Y}, \mathbf{y}) &= (\mathbf{A}\mathbf{y} + i\mathbf{B}\partial_{\mathbf{y}}) U(\mathbf{Y}, \mathbf{y}). \end{aligned} \quad (6.34)$$

Similarly using eq. (6.29b) I get

$$\begin{aligned} \langle \mathbf{X}(\mathbf{Y}) | \hat{\mathbf{K}} | \mathbf{x}(\mathbf{y}) \rangle &= \langle \mathbf{X}(\mathbf{Y}) | -\mathbf{B}\hat{\mathbf{x}} + \mathbf{A}\hat{\mathbf{k}} | \mathbf{x}(\mathbf{y}) \rangle \Leftrightarrow \\ -i\partial_{\mathbf{Y}} U(\mathbf{Y}, \mathbf{y}) &= (-\mathbf{B}\mathbf{y} + i\mathbf{A}\partial_{\mathbf{y}}) U(\mathbf{Y}, \mathbf{y}). \end{aligned} \quad (6.35)$$

I will assume that U can be written as $U(\mathbf{Y}, \mathbf{y}) = e^{-iF(\mathbf{Y}, \mathbf{y})}$ where $F(\mathbf{Y}, \mathbf{y})$ is some unspecified generating function. Then eqs. (6.34) and (6.35) and subsequent comparison with eq. (6.21) gives the following differential equations for F :

$$\partial_{\mathbf{y}} F = \mathbf{B}^{-1} \mathbf{Y} - \mathbf{B}^{-1} \mathbf{A}\mathbf{y} = \mathbf{k} \quad (6.36)$$

$$\partial_{\mathbf{Y}} F = \mathbf{B}\mathbf{y} - A\partial_{\mathbf{y}} F = -\mathbf{K}. \quad (6.37)$$

Thus, up to a constant the kernel U is generated by the first generating function such that $F = F_1(\mathbf{Y}, \mathbf{y}) + \alpha, \alpha \in \mathbb{C}$. The representation of the metaplectic transform of $\psi(\mathbf{x})$ in \mathbf{X} -space therefore is:

$$\Psi(\mathbf{X}) = e^{-i\alpha} \int d\mathbf{x} e^{-iF_1(\mathbf{X}, \mathbf{x})} \psi(\mathbf{x}), \quad (6.38)$$

where I switched back to the old notation instead of using \mathbf{y} and \mathbf{Y} . Requiring that the transformation is unitary such that $\|\Psi(\mathbf{X})\|_{L_2} = \|\psi(\mathbf{x})\|_{L_2}$ determines α up to a constant phase (Refs. [7, p. 47], [5, p. 470]). However, even after normalization I am left with an overall ambiguity in the phase which means that the correspondence between symplectic transforms and metaplectic operators is not one-to-one (Ref. [5, p. 470]). Rather, for each symplectic transformation \mathbf{S} there are two metaplectic transformations $\pm \hat{M}(\mathbf{S})$ differing by a phase of π (see Ref. [7, p. 47-48] for a detailed discussion). The final integral form of the metaplectic transform of $\psi(\mathbf{x})$ therefore is (Ref. [7]):

$$\Psi(\mathbf{X}) = \pm \frac{\exp\left(\frac{i}{2} \mathbf{X}^T \mathbf{A} \mathbf{B}^{-1} \mathbf{X}\right)}{(2\pi i)^{N/2} \sqrt{\det \mathbf{B}}} \int d\mathbf{x} \exp\left(\frac{i}{2} \mathbf{x} \mathbf{B}^{-1} \mathbf{A} \mathbf{x} - i \mathbf{x}^T \mathbf{B}^{-1} \mathbf{X}\right) \psi(\mathbf{x}) \quad (6.39)$$

Using the unitarity of the metaplectic transform, the inverse metaplectic transform can be shown to be (Ref. [7]):

$$\psi(\mathbf{x}) = \pm \frac{\exp(-\frac{i}{2}\mathbf{x}\mathbf{B}^{-1}\mathbf{A}\mathbf{x})}{(-2\pi i)^{N/2}\sqrt{\det \mathbf{B}}} \int d\mathbf{X} \exp\left(\frac{i}{2}\mathbf{X}^T \mathbf{A}\mathbf{B}^{-1}\mathbf{X} + i\mathbf{x}^T \mathbf{B}^{-1}\mathbf{X}\right) \Psi(\mathbf{X}) \quad (6.40)$$

The sign ambiguity of the metaplectic transform becomes relevant later when I consider a sequence of transformations evaluated along a ray. For the final solution of the wave field to be continuous, the overall phase of $\pm(\det \mathbf{B})^{-1/2}$ should be monotonically increasing (or monotonically decreasing) along a ray. My practical solution to ensuring this is described in section 6.6.

Note, in the special case where $\mathbf{A} = \mathbf{o}_N$ and $\mathbf{B} = \mathbf{I}_N$, I have $\mathbf{k} = \mathbf{X}$. In this case, the metaplectic transform of eq. (6.39) reduces to the Fourier transform of eq. (3.21 FT) (up to a normalization constant). This shows how the Fourier transform can be interpreted as the metaplectic transformation corresponding to the rotation in phase space that maps $(\mathbf{x}, \mathbf{k}) \mapsto (\mathbf{X}, \mathbf{K}) = (\mathbf{k}, -\mathbf{x})$. In 1D this is a 90° rotation of phase space.

6.4 Geometrical Optics in Rotated Phase Space

Say that I have now rotated the phase space coordinates with some symplectic transformation matrix such that $\hat{\mathbf{Z}} = \mathbf{S}\hat{\mathbf{z}}$. What is then the appropriate representation of the GO equations, eq. (4.31), in the rotated coordinate system? Fortunately, it can be shown that the GO equations have the exact same form when projected onto the new \mathbf{X} -space as the equations already derived in usual \mathbf{x} -space. I shall not derive this in detail, but simply state the main steps of the derivation taken from Ref. [7, ch. 6]. Similar to eq. (4.8), the envelope state in rotated phase space is defined as:

$$|\Phi\rangle := e^{-i\Theta(\hat{\mathbf{X}})} |\psi\rangle \quad (6.41)$$

This gives the wave equation:

$$e^{-i\Theta(\hat{\mathbf{X}})} \hat{D}(\hat{\mathbf{z}}) e^{i\Theta(\hat{\mathbf{X}})} |\Phi\rangle = |0\rangle \Leftrightarrow e^{-i\Theta(\hat{\mathbf{X}})} \left[\hat{M}(\mathbf{S}) \hat{M}^\dagger(\mathbf{S}) \hat{D}(\hat{\mathbf{z}}) \hat{M}(\mathbf{S}) \hat{M}^\dagger(\mathbf{S}) \right] e^{i\Theta(\hat{\mathbf{X}})} |\Phi\rangle = |0\rangle ,$$

where I squeezed in some metaplectic operators using the unitary property, eq. (6.27). At this point, Ref. [7] uses that the Weyl symbol of an operator is symplectic covariant. That is, it satisfies:

$$\mathbb{W}_{\mathbf{z}} \left[\hat{M}^\dagger(\mathbf{S}) \hat{D} \hat{M}(\mathbf{S}) \right] = \mathcal{D}(\mathbf{S}\mathbf{z}) = \mathcal{D}(\mathbf{Z}), \quad \text{and} \quad (6.42)$$

$$\mathbb{W}_{\mathbf{Z}} \left[\hat{M}(\mathbf{S}) \hat{M}^\dagger(\mathbf{S}) \hat{D}(\hat{\mathbf{z}}) \hat{M}(\mathbf{S}) \hat{M}^\dagger(\mathbf{S}) \right] = \mathcal{D}(\mathbf{S}^{-1}\mathbf{Z}) = \mathcal{D}(\mathbf{z}). \quad (6.43)$$

Thus, if two coordinate representations are connected via a symplectic transformation it does not change the value of the dispersion symbol evaluated in phase space. Ref. [7] then follows the procedure outlined in eq. (4.11) to approximate the wave equation eq. (6.42) in the GO limit. The result in the lowest order, $\mathcal{O}(\epsilon)$, is:

$$\left[\mathcal{D} \left[\mathbf{S}^{-1}\mathbf{Z}(\hat{\mathbf{X}}) \right] - \mathbf{V}(\hat{\mathbf{X}}) \cdot \hat{\mathbf{K}} + \frac{i}{2} \partial_{\mathbf{X}} \cdot \mathbf{V}(\hat{\mathbf{X}}) \right] |\Phi\rangle = |0\rangle , \quad \text{where} \quad (6.44)$$

$$\mathbf{K}(\mathbf{X}) := \partial_{\mathbf{X}} \Theta(\mathbf{X}), \quad \mathbf{V}(\mathbf{X}) := -\partial_{\mathbf{K}} \mathcal{D}(\mathbf{S}^{-1}\mathbf{Z}) \Big|_{\mathbf{K}=\mathbf{K}(\mathbf{X})} . \quad (6.45)$$

Projecting this down onto $|\mathbf{X}\rangle$ then gives the familiar equations (Ref. [7]):

$$\mathcal{D}[\mathbf{S}^{-1}\mathbf{Z}(\mathbf{X})] = 0 \quad (6.46a)$$

$$\mathbf{V}(\mathbf{X}) \cdot \partial_{\mathbf{X}}\Phi(\mathbf{X}) + \frac{1}{2}[\partial_{\mathbf{X}} \cdot \mathbf{V}(\mathbf{X})]\Phi(\mathbf{X}) = 0. \quad (6.46b)$$

As in eq. (4.45) the envelope equatino may to solved to give:

$$\Phi(\boldsymbol{\tau}) = \phi_0(\boldsymbol{\tau}_{\perp}) \sqrt{\frac{J(0, \boldsymbol{\tau}_{\perp})}{J(\boldsymbol{\tau})}}, \quad (6.47)$$

where $J(\boldsymbol{\tau}) := \det \partial_{\boldsymbol{\tau}}\mathbf{X}(\boldsymbol{\tau})$ is of course the Jacobian in rotated phase space. Of course one derive the Hamilton's equations in rotated phase space also:

$$\partial_{\tau_1}\mathbf{Z}(\boldsymbol{\tau}) = -\mathbf{J}_{2N}\mathcal{D}[\mathbf{S}^{-1}\mathbf{Z}(\boldsymbol{\tau})].$$

However it is impractical if we have to retrace the rays at each time step where we tilt the ray manifold. Fortunately, we don't need to. Ref. [7] shows this using the symplecticity of \mathbf{S}^{-1} (eq. (6.13)) and the chain rule:

$$\begin{aligned} \partial_{\tau_1}\mathbf{Z}(\boldsymbol{\tau}) &= -\mathbf{J}_{2N}\partial_{\mathbf{Z}}(\mathbf{S}^{-1}\mathbf{Z}(\boldsymbol{\tau}))\partial_{\mathbf{z}}\mathcal{D}(\mathbf{z}) \Big|_{\mathbf{z}=\mathbf{S}^{-1}\mathbf{Z}(\boldsymbol{\tau})} = -\mathbf{J}_{2N}\mathbf{S}^{-T}\partial_{\mathbf{z}}\mathcal{D}(\mathbf{z}) \Big|_{\mathbf{z}=\mathbf{S}^{-1}\mathbf{Z}(\boldsymbol{\tau})} \Leftrightarrow \\ \partial_{\tau_1}[\mathbf{S}^{-1}\mathbf{Z}(\boldsymbol{\tau})] &= -\mathbf{J}_{2N}\partial_{\mathbf{z}}\mathcal{D}(\mathbf{z}) \Big|_{\mathbf{z}=\mathbf{S}^{-1}\mathbf{Z}(\boldsymbol{\tau})} \end{aligned}$$

Comparison with eq. (6.7) shows that:

$$\mathbf{Z}(\boldsymbol{\tau}) = \mathbf{S}\mathbf{z}(\boldsymbol{\tau}). \quad (6.48)$$

Thus, the manifold in rotated phase space, $\mathbf{Z}(\boldsymbol{\tau})$, is simply obtained by rotating the original manifold $\mathbf{z}(\boldsymbol{\tau})$. As before the phase is obtained by integrating \mathbf{K} :

$$\Theta(\mathbf{X}) = \Theta(\mathbf{X}_0) + \int_{\mathbf{X}_0}^{\mathbf{X}} d\mathbf{X}' \cdot \mathbf{K}(\mathbf{X}') \quad \text{or} \quad \Theta(\tau_1) = \Theta_0 + \int_0^{\tau_1} d\tau_1 \dot{\mathbf{X}}(\tau_1) \cdot \mathbf{K}(\tau_1). \quad (6.49)$$

The wave field in the rotated plane is:

$$\Psi(\mathbf{X}) = \Phi(\mathbf{X})e^{i\Theta(\mathbf{X})}. \quad (6.50)$$

6.5 The MGO Recipe

I have now introduced the orthosymplectic transforms which rotates \mathbf{z} into \mathbf{Z} as well as their metaplectic counterparts which maps the representations of $\psi(\mathbf{x})$ into $\Psi(\mathbf{X})$. Furthermore Ref. [7] derived the GO equations when projected down to \mathbf{X} -space which I have presented in eq. (6.46a). Thereby I am ready to explain the main idea of MGO. Assume we are given a boundary condition at $x_1 = 0$ for the incoming electric field

$$\psi_{\text{in}}(\mathbf{x}_{\perp}) = \phi_0(\mathbf{x}_{\perp})e^{i\theta_0(\mathbf{x}_{\perp})} \quad (6.51)$$

The method then consists of the following six steps:

1. Trace a set of rays using eq. (4.39) to obtain $\mathbf{z}(\boldsymbol{\tau})$. Note that $\mathbf{z}(\boldsymbol{\tau})$ together with the boundary condition, eq. (6.51), contains all information for reconstructing the field.

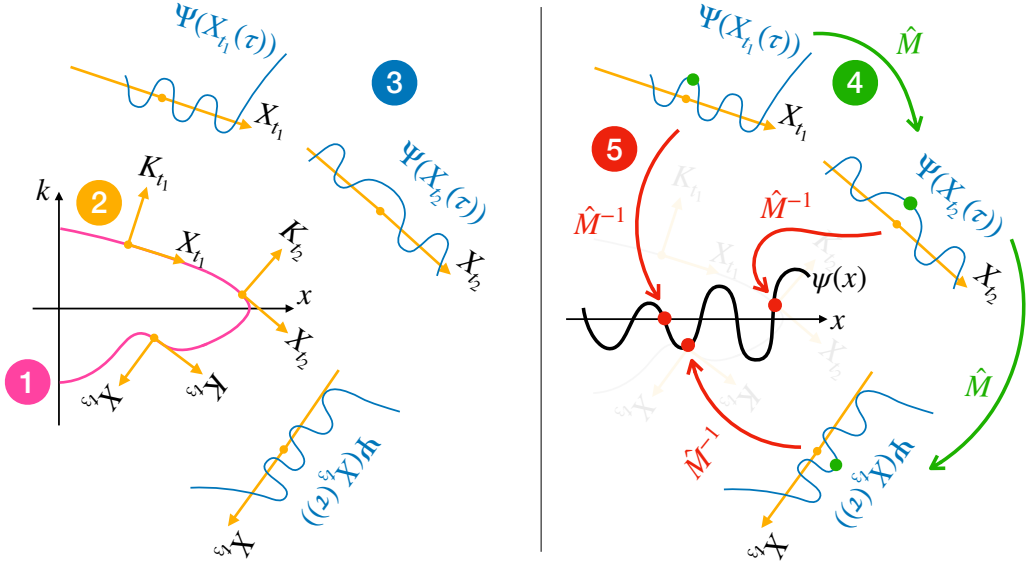


Figure 6.2: Illustration of the 5 steps of MGO. 1) Trace rays, 2) determine symplectic transformation S_t , 3) Solve GO in rotated phase space, 4) link the solutions together using metaplectic transforms such that the final solution is continuous 5) Inverse metaplectic transform the fields and add up the solutions from different branches.

2. For each point $\mathbf{t} \in \tau$ on the ray manifold determine a symplectic transformation S_t which maps $\mathbf{x}(\tau)$ to the tangent plane $\mathbf{X}_t(\tau)$ of the ray manifold at $\mathbf{z}(t)$.
3. For each point $\mathbf{t} \in \tau$ on the ray manifold, solve the GO phase and envelope equations in $\mathbf{X}_t, \mathbf{K}_t$ space to obtain $\Psi[\mathbf{X}_t(\tau)]$.
4. Ensure continuity of the solution by using a near-identity metaplectic transform to glue the initial conditions of the fields in rotated phase spaces together.
5. For each point $\mathbf{t} \in \tau$ on the ray manifold, inverse transform $\Psi[\mathbf{X}_t(\tau)]$ to obtain $\psi(\mathbf{x}(t))$. Sum up the field contributions from all branches of the ray manifold.

The five steps are illustrated on fig. 6.2. Note that there is a new transformation for each $\mathbf{t} \in \tau$ and this makes the notation slightly more tricky. For instance $\mathbf{X}_t(\tau)$ is a function of τ for a given fixed t , while $\mathbf{X}_t(t)$ is this function evaluated at $\tau = t$. Also note how the inverse metaplectic transform maps the function $\Psi[\mathbf{X}_t(\tau)]$ defined on the entire $\mathbf{X}_t(\tau)$ domain onto a single point. In the following I will present the theory from Refs. [7, 11] on how to perform the five steps. The first step, I have already discussed in chapter 4.

6.5.1 Determining orthosymplectic matrix S_t

The tangent plane of the ray manifold at $\mathbf{z}(t)$ is spanned by a set of unit tangent vectors $\check{\mathbf{T}}_1(\mathbf{t}), \dots, \check{\mathbf{T}}_N(\mathbf{t})$. The tangent vectors can be obtained from the Jacobian matrix of $\mathbf{z}(\tau)$:

$$[\partial_\tau \mathbf{z}]^T = \begin{pmatrix} \uparrow & & \uparrow \\ \partial_{\tau_1} \mathbf{z} & \dots & \partial_{\tau_N} \mathbf{z} \\ \downarrow & & \downarrow \end{pmatrix}. \quad (6.52)$$

An orthonormal basis for the tangent plane can be obtained by first defining:

$$\check{\mathbf{T}}_1(\mathbf{t}) := \partial_{\tau_1} \mathbf{z}(\mathbf{t}) / \|\partial_{\tau_1} \mathbf{z}(\mathbf{t})\|, \quad (6.53)$$

and then obtaining $\check{\mathbf{T}}_2(\mathbf{t}), \dots, \check{\mathbf{T}}_N(\mathbf{t})$ by Gram-Schmidt orthogonalization of the Jacobian matrix (Ref. [11]). This was the approach I took in my implementation, where I implemented a simple Gram-Schmidt orthogonalizer. From the set of tangent vectors one can also define the symplectically dual set of normal vectors:

$$\check{\mathbf{N}}_j(\mathbf{t}) = -\mathbf{J}_{2N} \check{\mathbf{T}}_j(\mathbf{t}). \quad (6.54)$$

Thereby the symplectic transformation which maps \mathbf{x} to the tangent plane is determined by:

$$\mathbf{S}^{-1} = \begin{pmatrix} \uparrow & \uparrow & \uparrow & \uparrow \\ \check{\mathbf{T}}_1(\mathbf{t}) & \dots & \check{\mathbf{T}}_N(\mathbf{t}) & \check{\mathbf{N}}_1(\mathbf{t}) & \dots & \check{\mathbf{N}}_N(\mathbf{t}) \\ \downarrow & \downarrow & \downarrow & \downarrow \end{pmatrix}. \quad (6.55)$$

Note, that it is the inverse matrix which is spanned by the tangent and normal vectors. This is because there is in general an inverse relationship between transformation of coordinates and coordinate axes. The coordinates are transformed by \mathbf{S} , but the axes are transformed by \mathbf{S}^{-1} (see Ref. [11]). Since this an orthonormal matrix, $\mathbf{S}_t = (\mathbf{S}^{-1})^T$.

However, in Ref. [7], N. A. Lopez presents a more direct way of obtaining the orthosymplectic matrix, namely through QR decomposition:

$$[\partial_{\tau} \mathbf{z}]^T = \mathbf{Q}_t \mathbf{R}_t \quad (6.56)$$

By construction, \mathbf{Q}_t is an orthonormal basis of the columns of the tangent space and therefore the matrix \mathbf{S} is simply defined by:

$$\mathbf{Q}_t = \begin{pmatrix} \mathbf{A}_t^T \\ \mathbf{B}_t^T \end{pmatrix}. \quad (6.57)$$

Note, for this to work it requires that \mathbf{R}_t has strictly positive diagonal elements (Ref. [7]) in order for the QR decomposition to be unique. I found that standard QR decomposition algorithms in Python do not honor this requirement, which is why I went for the self-made solution instead.

6.5.2 Obtaining the Wave Field in Rotated Phase Space

For the next step in MGO I need to determine the wave field in rotated phase space. This is straightforward due to the simplicity of GO equations in the transformed projection plane. From eq. (6.48) I get the rotated manifold:

$$\mathbf{Z}_t(\tau) = \mathbf{S}_t \mathbf{z}(\tau) \quad (6.58)$$

However for the phase an envelope, I need an initial condition. Here Ref. [7] makes the smart choice of normalizing $\Psi_t(\mathbf{X}_t(\mathbf{t}))$ to 1. This is done with the requirements (Ref. [7, p. 122]):

$$\Psi_t(\mathbf{X}_t) = \alpha_t \phi_t(\mathbf{X}_t) \exp[i\Theta_t(\mathbf{X}_t)], \quad \alpha_t := \Psi_t[\mathbf{X}_t(\mathbf{t})] \quad (6.59)$$

$$\Phi_t[\mathbf{X}_t(\mathbf{t})] = 1, \quad \Theta_t[\mathbf{X}_t(\mathbf{t})] = 0. \quad (6.60)$$

This choice is smart, since it means we can solve the GO equation without worrying about the initial condition until later in step 4) where α is determined. The phase and envelope are then be determined by eqs. (6.47) and (6.49):

$$\Theta_{\mathbf{t}}(\boldsymbol{\tau}) = \int_t^{\tau_1} d\xi \dot{\mathbf{X}}_{\mathbf{t}}(\xi, \boldsymbol{\tau}_{\perp}) \cdot \mathbf{K}_{\mathbf{t}}(\xi, \boldsymbol{\tau}_{\perp}) \quad (6.61)$$

$$\Phi_{\mathbf{t}}[\mathbf{X}_{\mathbf{t}}(\boldsymbol{\tau})] = \Phi_{\mathbf{t}}[\mathbf{X}_{\mathbf{t}}(t_1, \boldsymbol{\tau}_{\perp})] \sqrt{\frac{J_{\mathbf{t}}(t_1, \boldsymbol{\tau}_{\perp})}{J_{\mathbf{t}}(\boldsymbol{\tau})}}. \quad (6.62)$$

6.5.3 Linking Solutions with Near-Identity Metaplectic Transform

With the normalization choice of eq. (6.59), the function $\alpha_{\mathbf{t}}$ is crucial to glue the solutions together to make the final wave field continuous. This step is perhaps the least obvious to derive. Say we have two neighboring manifold coordinates \mathbf{t} and $\mathbf{t} + \mathbf{h}$. Lopez proposes determining $\alpha_{\mathbf{t}+\mathbf{h}} = \Psi_{\mathbf{t}+\mathbf{h}}[\mathbf{X}_{\mathbf{t}+\mathbf{h}}(\mathbf{t} + \mathbf{h})]$ by projecting the neighboring wave field $\Psi_{\mathbf{t}}(\mathbf{X}_{\mathbf{t}}(\mathbf{t}))$ onto the tangent plane at $\boldsymbol{\tau} = \mathbf{t} + \mathbf{h}$ (Ref. [7, p. 123]). This can be done by:

$$\alpha_{\mathbf{t}+\mathbf{h}} = \alpha_{\mathbf{t}} \mathbb{N}_{S_{\mathbf{t}+\mathbf{h}} S_{\mathbf{t}}^{-1}} \left\{ \Phi_{\mathbf{t}}(\mathbf{X}_{\mathbf{t}}) \exp[i\Theta(\mathbf{X}_{\mathbf{t}})] \Big|_{\mathbf{X}_{\mathbf{t}+\mathbf{h}}(\mathbf{t}+\mathbf{h})} \right\}, \quad (6.63)$$

where \mathbb{N}_S is the metaplectic transform in the near identity limit, aptly named the near identity metaplectic transform (NIMT). N. A. Lopez has developed an efficient algorithm for evaluating the NIMT, but from the work in Ref. [7] $\alpha_{\mathbf{t}}$ also has a simple analytic form which is combined into a simple prefactor in the final equation. I shall state the final result instead of going into the lengthy calculations.

6.5.4 Obtaining Final Solution in the Original Space

Finally, when I have determined the wave field in the tangent space and calculated the NIMT linking function all that remains is to perform an inverse metaplectic transform to project the wave fields back onto \mathbf{x} space. This is facilitated by the inverse metaplectic transform:

$$\alpha_{\mathbf{t}} \int d\mathbf{X}_{\mathbf{t}} U_{\mathbf{t}}^{-1}(\mathbf{x}, \mathbf{X}_{\mathbf{t}}) \Psi_{\mathbf{t}}(\mathbf{X}_{\mathbf{t}}), \quad (6.64)$$

where $U_{\mathbf{t}}^{-1}(\mathbf{x}, \mathbf{X}_{\mathbf{t}})$ is the kernel of the inverse transform at $\boldsymbol{\tau} = \mathbf{t}$ given by eq. (6.40). However, care should be taking when evaluating the integral, since we are only interested in the contribution close to $\mathbf{X}_{\mathbf{t}}(\mathbf{t})$. To make the integral well-behaved it should be evaluated using the method of steepest descent. In this method the contour passes through a saddle point of the phase of the integrand and follows lines where the real part of the phase is constant. The interested reader may consult [18, 36] for more information. By integrating through the steepest descent contour that goes through $\mathbf{X}_{\mathbf{t}} = \mathbf{X}_{\mathbf{t}}(\mathbf{t})$ we only get the relevant saddle point contributions (Ref. [7, p. 129]). Therefore, defining $\boldsymbol{\epsilon} := \mathbf{X}_{\mathbf{t}} - \mathbf{X}_{\mathbf{t}}(\mathbf{t})$, the inverse metaplectic transform becomes (Ref. [7, p. 129]):

$$\psi_{\mathbf{t}}(\mathbf{x}) = \psi[\mathbf{t}(\mathbf{x})] = \alpha_{\mathbf{t}} \int_{C_0} d\boldsymbol{\epsilon} U_{\mathbf{t}}^{-1}[\mathbf{x}, \boldsymbol{\epsilon} + \mathbf{X}_{\mathbf{t}}(\mathbf{t})] \Psi_{\mathbf{t}}[\boldsymbol{\epsilon} + \mathbf{X}_{\mathbf{t}}(\mathbf{t})], \quad (6.65)$$

where C_0 is the steepest descent contour through $\boldsymbol{\epsilon} = \mathbf{0}$.

Finally the total wave field is calculated by summing up all contributions from the different branches $\boldsymbol{\tau}_1(\mathbf{x}), \boldsymbol{\tau}_2(\mathbf{x}), \dots, \boldsymbol{\tau}_b(\mathbf{x})$ (see also sections 4.3.3 and 4.4.3):

$$\psi(\mathbf{x}) = \sum_{i=1}^b \psi[\boldsymbol{\tau}_i(\mathbf{x})]. \quad (6.66)$$

6.5.5 Analytic Continuation using Function Fits

As suggested in Ref. [12], in my numerical implementation I evaluate the integral of eq. (6.65) along the steepest descent contour using Gauss-Freud quadrature. I give a short introduction to the Gauss-quadrature method in appendix B. However, to evaluate the integrand along the steepest descent contour, I also need to know the integrand's function values in the complex domain. This is no problem in an analytic implementation of MGO, but in a numerical treatment one only knows the function values of $\Psi_t[\epsilon + \mathbf{X}_t(t)]$ on the real domain after having calculated the phase and envelope using eqs. (6.47) and (6.49). That is, in 1D we only know $\Psi_t(\epsilon)$ on $\text{Re}\{\epsilon\}$. To solve this problem, I have implemented a rational function fitting module. Rational function fits, also known as Type II Padé approximants [44] assume a regression model on the form

$$f_{L/M}(z) := \frac{p_L(z)}{p_M(z)}, \quad (6.67)$$

where p_L is an L 'th degree polynomial and p_M is an M 'th degree polynomial. My module also works for higher dimensions, but the MGO examples I present are all 1D. The idea with the fit is of course that I may approximate the numerical $\Psi_t(\epsilon)$ on the real line with a rational function fit and then extend this function to the complex plane afterwards. Generally pade approximants can be highly flexible and even with low degrees it is possible to fit many functions [44]. I used a least square regression method to fit the functions to the numerical data as suggested in Ref. [45]. This has the advantage of being computationally fast, but it may also give spurious results such as singularities in the middle of the domain of interest. For this reason, I find that the method is quite sensitive to the choice of nominator-denominator degree. So an improvement in this approach is definitely needed. I will return to this discussion.

6.6 Summary of MGO

I will end this chapter with a summary of the MGO method. The simple end results are derived in Ref. [7]. Though the examples I show in the next chapter are 1D I will present the full results valid in N dimensions here.

Let $\mathbf{x}_\perp = (x_2, x_3)^T$ and assume that the incoming wave field is defined on the boundary of $x_1 = 0$:

$$\psi_{\text{in}}(\mathbf{x}_\perp) = \phi_0(\mathbf{x}_\perp) e^{i\theta_0(\mathbf{x}_\perp)}. \quad (6.68)$$

Furthermore, assume that we have an initial \mathbf{z}_0 satisfying the local dispersion relation, i.e. $\mathcal{D}(\mathbf{z}_0) = 0$. The procedure is then as follows.

First, evolve the rays using eq. (4.39) to obtain $\mathbf{z}(\tau)$. For all ray manifold coordinates \mathbf{t} : Determine the Jacobian (see section 4.4.1) and determine its QR decomposition:

$$[\partial_\tau \mathbf{z}]^T = \mathbf{Q}_t \mathbf{R}_t, \quad \mathbf{Q}_t = \begin{pmatrix} \mathbf{A}_t^T \\ \mathbf{B}_t^T \end{pmatrix}. \quad (6.69)$$

The symplectic transformation matrix then is:

$$\mathbf{S}_t = \begin{pmatrix} \mathbf{A}_t & \mathbf{B}_t \\ -\mathbf{B}_t & \mathbf{A}_t \end{pmatrix}. \quad (6.70)$$

The rotated phase space coordinates are calculated from the symplectic transformation matrix:

$$\mathbf{Z}_t(\tau) = \begin{pmatrix} \mathbf{X}_t(\tau) \\ \mathbf{K}_t(\tau) \end{pmatrix} := S_t \mathbf{z}(\tau) \quad (6.71)$$

The inverse metaplectic transform, eqs. (6.40) and (6.65), and the α_t factor from the NIMT give rise to a simple "MGO prefactor" \mathcal{N}_t which may be evaluated independently from the integral (Ref. [7]):

$$\mathcal{N}_t = \frac{\psi_{in}(\tau_\perp) \sqrt{\dot{x}_1(0, \mathbf{t}_\perp)} \exp\left[i \int_0^{t_1} d\xi \mathbf{k}^T(\xi, \tau_\perp) \dot{\mathbf{x}}(\xi, \tau_\perp)\right]}{(-2\pi i)^{\rho/2} e^{i\varphi/2} \sqrt{\det \Lambda_{\rho\rho} \det \mathbf{a}_{\varsigma\varsigma} \det \mathbf{R}_t}}, \quad \text{where} \quad (6.72a)$$

$$\varphi(t) := \arg B_t \text{ must be monotonically increasing} \quad (6.72b)$$

Here dot is differentiation with respect to the first coordinate and $\Lambda_{\rho\rho}, \mathbf{a}_{\varsigma\varsigma}$ are defined in eqs. (6.23) and (6.25). Please note that my definition of \mathcal{N}_t is formulated slightly different from [7]. First, I have defined $\varphi(t)$ as the argument of B_t . Since $B_t \in \mathbb{R}$, $\varphi(t) \in \{n\pi \mid n \in \mathbb{Z}\}$. By construction φ must be monotonically increasing as a function of t to avoid crossing branch cuts in the square root $\sqrt{\text{sign } B_t} := e^{i\varphi/2}$. Second, as opposed to [7] I define the non-zero singular values in $\Lambda_{\rho\rho}$ to always be positive since this is a customary convention for SVD [25, p. 604]. Note also, that \mathbf{R}_t is the upper triangular matrix from the QR decomposition. This is not to be confused with the \mathbf{R}_s from the SVD of \mathbf{B}_t .

The envelope in the rotated phase space is calculated as

$$\Phi_t[\mathbf{X}_t(\tau)] = \sqrt{\frac{J_t(t_1, \tau_\perp)}{J_t(\tau_1, \tau_\perp)}}, \quad (6.73)$$

where $J_t(\tau)$ is the Jacobian determinant in the rotated phase space:

$$J_t(\tau) = \det[\partial_\tau \mathbf{X}_t(\tau)]. \quad (6.74)$$

And the phase is obtained from:

$$\Theta_t[\mathbf{X}_t(\tau)] = \int_{\mathbf{X}_t(t)}^{\mathbf{X}_t(\tau)} d\mathbf{X}_t^T \mathbf{K}_t(\mathbf{X}_t) = \int_{t_1}^{\tau_1} d\xi \dot{\mathbf{X}}_t^T(\xi, \tau_\perp) \mathbf{K}_t(\xi, \tau_\perp). \quad (6.75)$$

Together these compose the eikonal solution in the rotated phase space:

$$\Psi_t(\tau) = \Phi_t(\tau) \exp[i\Theta_t(\tau)]. \quad (6.76)$$

Apart from the constants absorbed by the MGO prefactor, the inverse metaplectic transform gives:

$$\Upsilon_t = \int_{C_0} d\epsilon \Psi_t[\mathbf{X}_t(t) + \epsilon] \exp\left[-\frac{i}{2} \epsilon^T \mathbf{A}_t \mathbf{B}_t^{-1} \epsilon - i\epsilon^T \mathbf{K}_t(t)\right] \quad (6.77)$$

Alternatively this may also be written:

$$\Upsilon_t = \int_{C_0} d\epsilon \Phi_t(\epsilon) \exp[i f_t(\epsilon)] \quad (6.78a)$$

where

$$\Phi_t(\epsilon) := \Phi_t[\mathbf{X}_t(t) + \epsilon], \quad f_t(\epsilon) := \Theta[\mathbf{X}_t(t) + \epsilon] - \frac{1}{2} \epsilon^T \mathbf{A}_t \mathbf{B}_t^{-1} \epsilon - \epsilon^T \mathbf{K}_t(t). \quad (6.78b)$$

If $\det \mathbf{B}_t = 0$, we should instead use the form:

$$\Upsilon_t = \int_{C_0} d\epsilon_\rho \Psi_t \left[\mathbf{L}_s \begin{pmatrix} \mathbf{X}_t^\rho(\mathbf{t}) + \epsilon_\rho \\ \mathbf{a}_{\varsigma\varsigma} \mathbf{x}_\varsigma(\mathbf{t}) \end{pmatrix} \right] \exp \left[-\frac{i}{2} \epsilon_\rho^T \mathbf{a}_{\rho\rho} \mathbf{A}_{\rho\rho}^{-1} \epsilon_\rho - i \epsilon_\rho^T \mathbf{K}_t^\rho(\mathbf{t}) \right] \quad (6.79)$$

The final solution to the wave field is obtained by summing up the contributions from all branches:

$$\psi(\mathbf{x}) = \sum_{i=1}^b \psi(\boldsymbol{\tau}_i(\mathbf{x})), \quad \text{where} \quad \psi[\boldsymbol{\tau}_i(\mathbf{x})] = \mathcal{N}_{\boldsymbol{\tau}_i} \Upsilon_{\boldsymbol{\tau}_i}. \quad (6.80)$$

7 Results from Numerical MGO Algorithm

7.1 Airy's Equation

As a first showcase of the numerical implementation of the MGO algorithm, I revisit the Airy Equation example, eq. (5.4 Ai) from section 5.2:

$$\partial_x^2 \psi(x) - x\psi(x) = 0. \quad (7.1)$$

7.1.1 Analytic Derivation of MGO Solution to Airy's Equation

In Ref. [7], Nicolas Alexander Lopez presents a detailed analytic walk-through of using MGO on the Airy Equation example. For convenience I will repeat his analytic calculation here such that I can compare my numerical results with the analytic ones. Hopefully, it is also instructive for the reader to see the MGO algorithm carried out analytically before I turn to the numerical results.

In section 5.2, eqs. (5.13) and (5.14) I found the dispersion symbol of Airy's equation and resulting ray trace path to be given by:

$$\mathcal{D}(x, k) = -k^2 - x. \quad (7.2)$$

$$\mathbf{z}(\tau) = \begin{pmatrix} x(\tau) \\ k(\tau) \end{pmatrix} = \begin{pmatrix} -(k_0 - \tau)^2 \\ k_0 - \tau \end{pmatrix}, \quad (7.3)$$

where $k_0 = \sqrt{-x_0}$ was determined from the initial position $x_0 < 0$. The derivative of \mathbf{z} with respect to τ therefore is:

$$\partial_\tau \mathbf{z} = \begin{bmatrix} 2k(\tau) \\ -1 \end{bmatrix}.$$

And the QR decomposition of $\partial_\tau \mathbf{z}(t)$ then gives the symplectic transformation matrix:

$$Q_t = \frac{1}{\vartheta_t} \begin{bmatrix} 2k(t) \\ -1 \end{bmatrix} = \begin{bmatrix} A_t \\ B_t \end{bmatrix}, \quad R_t = \vartheta_t, \quad \text{where} \\ \vartheta_t := \sqrt{1 + 4k^2(t)}.$$

The symplectic transformation matrix at time $\tau = t$ is:

$$\mathbf{S}_t = \begin{bmatrix} A_t & B_t \\ -B_t & A_t \end{bmatrix} = \frac{1}{\vartheta_t} \begin{bmatrix} 2k(t) & -1 \\ 1 & 2k(t) \end{bmatrix}.$$

The prefactor, \mathcal{N}_t , is calculated from (6.72):

$$\mathcal{N}_t = c_0 \frac{\exp \left[i \int_0^t d\xi k(\xi) \dot{x}(\xi) \right]}{(-2\pi i)^{\rho/2} \sqrt{A_{\rho\rho} R_t \det a_{\varsigma\varsigma}}}$$

In this case, B_t , is of full rank ($\rho = 1, \varsigma = 0$) and therefore the SVD is particularly simple. We have¹ $\Lambda_{\rho\rho} = -B_t = \vartheta_t^{-1}$. $a_{\varsigma\varsigma}$ is empty and, following the convention in [7], its' determinant is therefore 1: $\det[a_{\varsigma\varsigma}] = 1$. This gives: $\Lambda_{\rho\rho} R_t \det[a_{\varsigma\varsigma}] = 1$. Since B_t does not change sign, we need not worry about its' argument φ to make the square root function continuous. \mathcal{N}_t therefore becomes:

$$\mathcal{N}_t = \left(\frac{c_0}{\sqrt{-2\pi i}} \right) \exp \left[i \left(2k_0^2 t - 2k_0 t^2 + \frac{2t^3}{3} \right) \right]. \quad (7.4)$$

Having calculated \mathcal{N}_t , we continue on to Υ_t . Since $\det[B_t] \neq 0$ we can use eq. (6.78):

$$\Upsilon_t = \int_{C_0} d\epsilon \Phi_t(\epsilon) \exp[i f_t(\epsilon)] \quad (7.5a)$$

where

$$\Phi_t(\epsilon) := \Phi_t[X_t(t) + \epsilon], \quad f_t(\epsilon) := \Theta[X_t(t) + \epsilon] - \frac{1}{2} \frac{A_t}{B_t} \epsilon^2 - K_t(t)\epsilon. \quad (7.5b)$$

The transformed phase space coordinates are calculated from eq. (6.71):

$$\mathbf{Z}_t(\tau) = \mathbf{S}_t \mathbf{z}(\tau) = \begin{pmatrix} X_t(\tau) \\ K_t(\tau) \end{pmatrix} = \frac{1}{\vartheta_t} \begin{pmatrix} -k(\tau) - 2k(t)k^2(\tau) \\ 2k(t)k(\tau) - k^2(\tau) \end{pmatrix} \quad (7.6)$$

This gives the Jacobian from eq. (6.74):

$$J_t(\tau) := \dot{X}_t(\tau) := \partial_\tau X_t(\tau) = \frac{4k(t)k(\tau) + 1}{\vartheta_t}. \quad (7.7)$$

The envelope is then determined from eq. (6.73):

$$\Phi_t[X_t(\tau)] = \sqrt{\frac{J_t(t)}{J_t(\tau)}} = \sqrt{\frac{4k^2(t) + 1}{4k(t)k(\tau) + 1}} = \frac{\vartheta_t}{\sqrt{4k(t)k(\tau) + 1}}.$$

To move on, we need to isolate τ as a function of X_t in eq. (7.6) and substitute this into $k(\tau)$ and thereafter $K_t(\tau)$. This yields [7, p. 154]:

$$\tau(X_t) = k_0 - \frac{-1 \pm \sqrt{1 - 8k(t)\vartheta_t X_t}}{4k(t)}, \quad (7.8)$$

$$k[X_t(\tau)] = \frac{-1 \pm \sqrt{1 - 8k(t)\vartheta_t X_t}}{4k(t)} \Rightarrow 4k(t)k[X_t(\tau)] = -1 \pm \sqrt{1 - 8k(t)\vartheta_t X_t} \quad (7.9)$$

$$K_t(X_t) := K_t[\tau(X_t)] = \frac{4k(t)X_t + \vartheta_t \left[-1 \pm \sqrt{1 - 8k(t)\vartheta_t X_t} \right]}{8k^2(t)} \quad (7.10)$$

The two signs reflect that there are two branches. As explained in [7, p. 155] we need to choose the plus sign (in all three equations) to ensure that $K_t[X_t(t)] = K_t(t)$ and thereby pick the correct branch. To simplify the expression further, note that

$$1 - 8k(t)\vartheta_t X_t = 1 - 8k(t)\vartheta_t X_t(t) - 8k(t)\vartheta_t \epsilon. \quad (7.11)$$

¹In Ref. [7] $\Lambda_{\rho\rho}$ has the opposite sign, i.e. $\Lambda_{\rho\rho} = B_t$, but I obtain this sign if I follow the convention that singular values are positive (see e.g. Ref. [25, p. 604]). Since it anyway is constant, it does not change the final solution.

Equation (7.6) gives $X_t(t) = -k(t)(1+2k^2(t))/\vartheta_t$ which simplifies eq. (7.11) above, giving:

$$1 - 8k(t)\vartheta_t X_t = \vartheta_t^4 - 8k(t)\vartheta_t \epsilon.$$

Thus, the envelope in the rotated phase space is:

$$\Phi_t[X_t(\tau)] = \frac{\vartheta_t}{(\vartheta_t^4 - 8k(t)\vartheta_t \epsilon)^{1/4}}. \quad (7.12)$$

The phase is determined from eq. (6.75) with the help of eqs. (7.6) and (7.10) (Ref. [7, p. 155]):

$$\begin{aligned} \Theta_t[X_t(t) + \epsilon] &= \int_{X_t(t)}^{X_t(t)+\epsilon} dX_t K_t(X_t) \\ &= \frac{8k^4(t) - \vartheta_t^4}{8k^2(t)\vartheta_t} \epsilon + \frac{1}{4k(t)} \epsilon^2 + \frac{\vartheta_t^6 - [\vartheta_t^4 - 8k(t)\vartheta_t \epsilon]^{3/2}}{96k^3(t)}. \end{aligned} \quad (7.13)$$

The field in the rotated phase space thereby is

$$\Psi_t[X_t(t) + \epsilon] = \frac{\vartheta_t}{\sqrt{4k(t)k(\tau) + 1}} \exp \left[i \left(\frac{8k^4(t) - \vartheta_t^4}{8k^2(t)\vartheta_t} \epsilon + \frac{1}{4k(t)} \epsilon^2 + \frac{\vartheta_t^6 - [\vartheta_t^4 - 8k(t)\vartheta_t \epsilon]^{3/2}}{96k^3(t)} \right) \right] \quad (7.14)$$

Finally, for the "phase factor", f , from eq. (7.5) we need to evaluate:

$$-\frac{1}{2} \frac{A_t}{B_t} \epsilon^2 - K_t(t) \epsilon = k(t) \epsilon^2 - (-B_t x(t) + A_t k(t)) \epsilon = k(t) \epsilon^2 - \frac{k^2(t)}{\vartheta_t} \epsilon.$$

Thereby, the phase factor f becomes:

$$f_t(\epsilon) = -\frac{\vartheta_t^3}{8k^2(t)} \epsilon + \frac{\vartheta_t}{4k(t)} \epsilon^2 + \frac{\vartheta_t^6 - [\vartheta_t^4 - 8k(t)\vartheta_t \epsilon]^{3/2}}{96k^3(t)}. \quad (7.15)$$

To obtain the final solution, one needs to carry out the integral of eq. (7.5) and sum up the contributions from the two branches with $j \geq 0$ and $j < 0$ respectively. However, all of the above and the integration itself is of course automated in the numerical implementation, and the equations derived so far are sufficient for comparing the numerical and analytic results. Therefore, I will now continue on to present the numerical results.

7.1.2 Numerical Results for Airy's Equation

Before presenting the numerical results, I would like to stress that all numerical results presented in this chapter were generated without supervision (except for the choice of fitting parameters in the analytic continuation) by my automated numerical implementation of the MGO algorithm. The analytic results above are included solely for benchmarking and pedagogical purposes. On fig. 7.1 I present snapshots from the numerical MGO algorithm at five different time points on the traced ray of Airy's Equation.

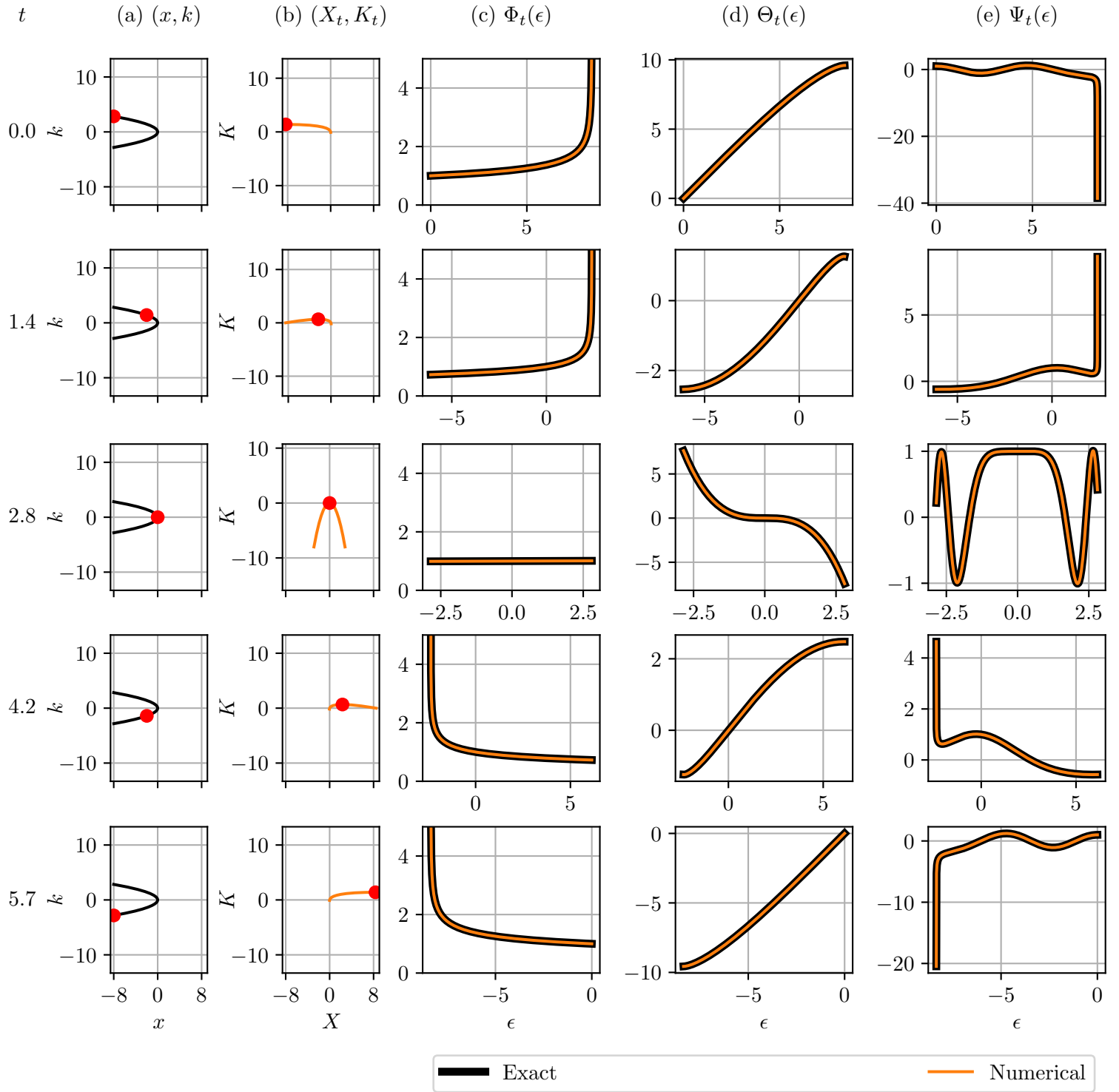


Figure 7.1: Illustration of the MGO algorithm at different time points for the Airy equation example. (a) Ray manifold with red dot indicating phase space location at time t , (b) Current branch of symplectically transformed ray manifold, (c)-(e) Metaplectically transformed fields as functions of $\epsilon = X_t(\tau) - X_t(t)$ corresponding to symplectic transformation at time t : (c) eikonal envelope, (d) eikonal phase, (e) eikonal wave field. For (c)-(e) I have shown both the exact closed-form MGO result from eqs. (7.12) to (7.14) and the result from my numerical implementation. The ray tracing started at $x(0) = -8$ and was automatically stopped when returning to its' starting position.

Figure 7.1 (a) shows the ray trace which is a parabola as predicted by eq. (7.3) and as we have seen previously on e.g. fig. 5.5 (a). The current time point is indicated with a red dot. In the numerical implementation the time started at $t = 0$ at initial position $x(0) = -8$ and initial wave number $k(0) = \sqrt{8}$. I did not convert the time into the true physical time in seconds (see [5, Eq. (3.26), p. 87]), so it is instead the "parameter time" of the ray equations eq. (4.39) which I refer to. The caustic is met halfway in the ray trace at about $t = 2.8$. On Figure 7.1 (b) I show the ray manifold in the rotated phase space coordinate system corresponding to eq. (7.6). Per construction, the new X_t -axis is always tangential to the ray manifold at the current point $X_t(t)$. On fig. 7.1 (c)-(e) I show the metaplectically transformed envelope, phase and wave field respectively as a function of $\epsilon = X_t - X_t(t)$. At the caustic, $t = 2.8$, the ray manifold is rotated 90° and the metaplectic transform is therefore a Fourier Transform. On fig. 7.1 (c)-(e) I have compared the numerical results (orange thin line) with the analytic results (black thick line) of eqs. (7.12) to (7.14). The numerical results clearly agree with the analytic results. By inspection of fig. 7.1 (c) it is clear that the caustic in rotated phase space, where $\Phi_t(\epsilon)$ diverge, is always a good distance away from $\epsilon = 0$ as we had hoped for. Therefore the integral eq. (7.5) should be finite. At $t = 2.8$ there is no caustic at all, since there is no longer any singularity when projecting the rotated ray manifold onto the X_t -axis.

Having assured that the numerical fields match the analytic results, the next step is to perform the integration of eq. (7.5). The integral is carried out along the contours of steepest descent of $-\text{Im } f_t(\epsilon)$ using Gauss-Freud quadrature. To find the steepest descent and perform the integration, we need to analytically continue the amplitude $\Phi_t(\epsilon)$ and phase function $f_t(\epsilon)$. As discussed in section 6.5.5 I have proposed solving this by making a rational function fit to the values of $\Phi_t(\epsilon), f_t(\epsilon)$ along the real line and then extrapolate the rational function to the complex plane. On fig. 7.2 I present these rational function fits of $\Phi_t(\epsilon), f_t(\epsilon)$ for the same five different time points as seen on fig. 7.1. Just like on fig. 7.1, fig. 7.2 (a) shows the ray manifold with the current position indicated with a red dot. Figure 7.2 (b) shows the numerical amplitude Φ_t as a function of $\epsilon = X_t - X_t(t)$ together with a rational function fit with (nominator, denominator)-degrees $(L_\Phi, M_\Phi) = (4, 3)$. The rational function appears to fit the numerical data with high accuracy. Continuing, on fig. 7.2 (c) I show the numerical values of $f_t(\epsilon)$ together with a rational fit with degrees $(L_f, M_f) = (6, 3)$. Again the rational functions fit the data accurately. On fig. 7.2 (d) I show a filled contour plot of the exact negative imaginary value of $f_t(\epsilon)$ in the complex plain using the analytic expression of eq. (7.15). The contour plot in fig. 7.2 (d) is to be compared to the numerical result in fig. 7.2 (e) which is the result of extending the rational function fit to the complex plane. All contour plots on fig. 7.2 have the same colour scale such that the plots can be mutually compared. From visual inspection, the analytic continuation of the numerical values of $f_t(\epsilon)$ in fig. 7.2 (d) fits very well with the exact result in fig. 7.2 (e). Similar to [12], on fig. 7.2 (d)-(e) I have also shown the nodes of the Gauss-Freud quadrature along the approximated steepest descent contour. The approximated straight line contour might deviate slightly from the true curved steepest descent path.

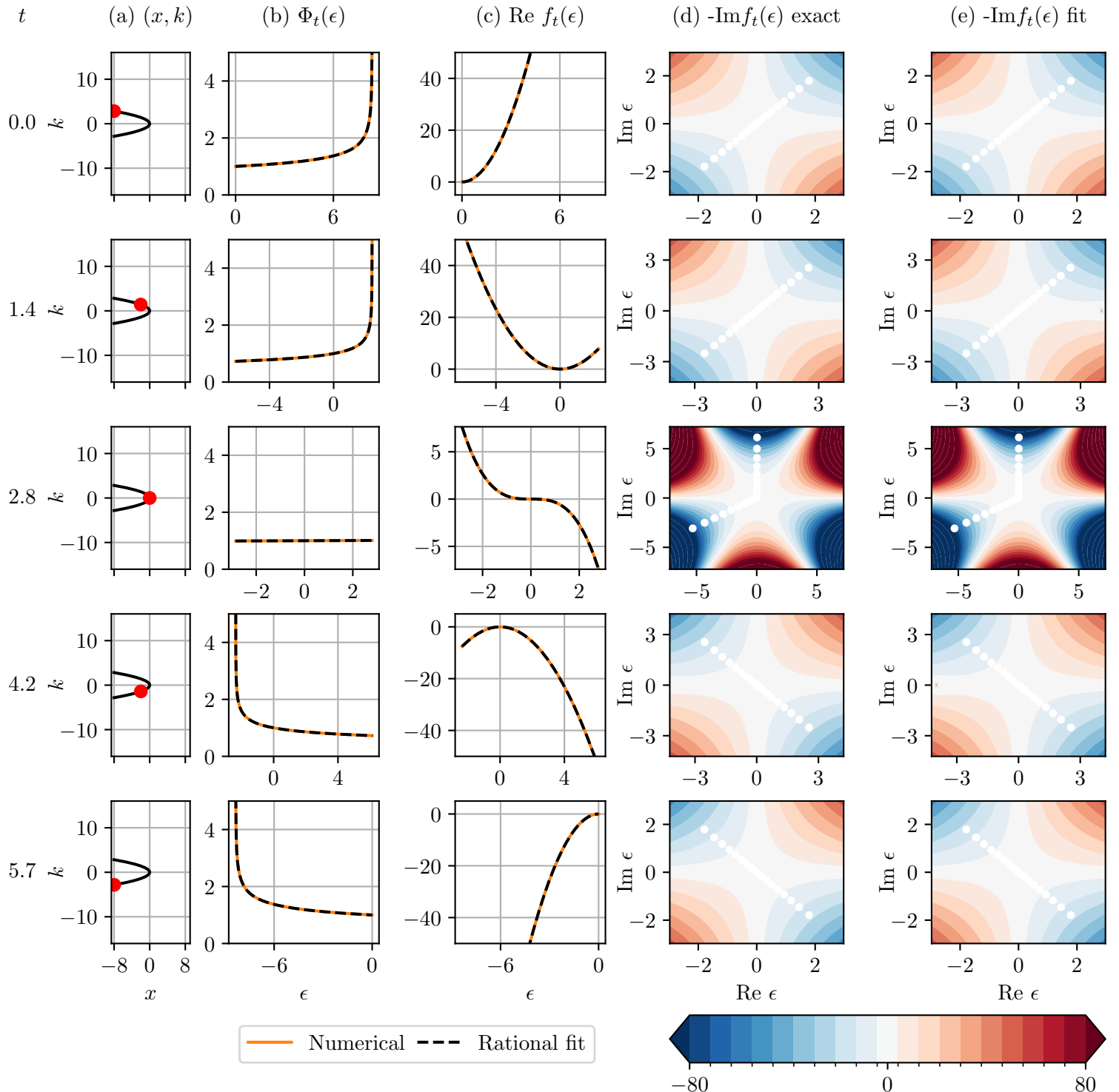


Figure 7.2: Inspection of fits needed for the analytic continuation in order to evaluate the steepest descent integral as part of the inverse metaplectic transform step for the Airy equation example. (a) Ray manifold with red dot indicating phase space location at time t , (b)-(c) Metaplectically transformed envelope, g , and phase factor, f , as functions of $\epsilon = X_t - X_t(t) \in \mathbb{R}$, (d) exact “-Im” part of the analytically continued phase factor from eq. (7.15) evaluated on $\epsilon \in \mathbb{C}$, (e) fit of f evaluated on $\epsilon \in \mathbb{C}$. For both (b) and (c) I have included the numerical result (which in Figure 7.1 was found to agree with the exact result along $\text{Re } \epsilon$), and the rational function fit with (nominator, denominator)-degrees: $(L_f, M_f) = (6, 3)$ and $(L_\Phi, M_\Phi) = (4, 3)$. For (d) and (e) I have also shown the the gauss quadrature node loci along the steepest descent contour used to evaluate the integral of the inverse metaplectic transform.

Finally, the wave field solution in x -space is obtained by performing the Gauss-Freud quadrature integration of eq. (7.5), multiplying with the prefactor of eq. (7.4) and summing up the contribution from both branches of the ray manifold as instructed by eq. (6.80). The final result is shown in fig. 7.3. For comparison I have shown both the exact solution given by the Airy function $E(x) = \text{Ai}(x)$, the GO solution also seen on fig. 5.5 and the MGO solution. While the GO solution clearly diverges at the caustic, the MGO solution stays finite and matches the true solution accurately even close to the caustic. The Gauss-Freud quadrature integration was carried out using $n = 10$ nodes. The amplitude of the MGO solution was determined after interpolating and superposing the contributions from the ingoing and outgoing branch by demanding that the summed interpolated field should equal the exact Airy function at the boundary, I.e. $E_{\text{MGO}}(x = -8) = \text{Ai}(-8)$. In conclusion, the numerical MGO algorithm successfully reconstructed the exact field as was done analytically in Refs. [11, 12, 7].

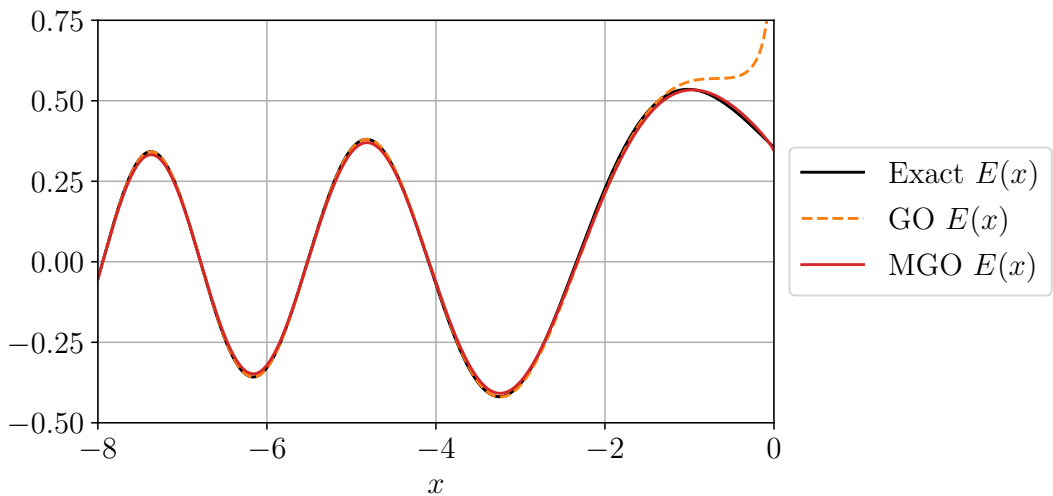


Figure 7.3: MGO solutions to Airy's Equation, eq. (7.1). I have shown both the exact wave function, $E(x) = \text{Ai}(x)$, the GO approximation, and the solution from applying the MGO algorithm with rational function fits with (nominator, denominator)-degrees, $(L_f, M_f) = (6, 3)$, $(L_\phi, M_\phi) = (4, 3)$, to perform the analytic continuation. The Gauss-Freud quadrature integration was carried out using $n = 10$ nodes.

7.2 Weber's Equation

Having solved the Airy problem with the numerical MGO method, I continue on to Weber's Equation, eq. (5.16 We) from section 5.3:

$$\left(2E - \hat{k}^2 - \hat{x}^2\right) |\psi\rangle = |0\rangle . \quad (7.16)$$

The exact solution is given by eq. (5.17).

7.2.1 Analytic Derivation of MGO Solution to Weber's Equation

Similar to the Airy problem, I will repeat the analytic calculations of [7, p.158-163] for benchmarking against my numerical implementation. The MGO procedure is similar to the Airy example except for one important change; The transformation matrix component B_t from eq. (6.70) this time changes sign along the ray, and therefore the argument, φ , of B_t should be chosen carefully to avoid branch cuts in the square root function of eq. (6.72). In eqs. (5.19) and (5.20) in section 5.3 we saw that the dispersion symbol and ray phase space trajectory were given by:

$$\mathcal{D}(x, k) = -k^2 - x^2 + 2E. \quad (7.17)$$

$$\mathbf{z}(\tau) = \begin{pmatrix} x(\tau) \\ k(\tau) \end{pmatrix} = \sqrt{2E} \begin{pmatrix} \cos 2\tau \\ -\sin 2\tau \end{pmatrix}. \quad (7.18)$$

The derivative of \mathbf{z} therefore is:

$$\partial_\tau \mathbf{z} = 2\sqrt{2E} \begin{bmatrix} -\sin(2\tau) \\ -\cos(2\tau) \end{bmatrix}. \quad (7.19)$$

The QR decomposition gives the symplectic transformation:

$$Q_t = \begin{bmatrix} -\sin 2t \\ -\cos 2t \end{bmatrix} = \begin{bmatrix} A_t \\ B_t \end{bmatrix}, \quad R_t = 2\sqrt{2E}, \quad (7.20a)$$

$$\mathbf{S}_t = \begin{bmatrix} A_t & B_t \\ -B_t & A_t \end{bmatrix} = \begin{bmatrix} -\sin 2t & -\cos 2t \\ \cos 2t & -\sin 2t \end{bmatrix} = \frac{1}{\sqrt{2E}} \begin{bmatrix} k(t) & -x(t) \\ x(t) & k(t) \end{bmatrix}. \quad (7.20b)$$

As before, B_t has full rank, $\rho = 1$, $\det a_{\varsigma\varsigma} = 1$, $\Lambda_{\rho\rho} = |B_t| = |\cos(2t)|$. As mentioned, this time $B_t = -x(t) = -\cos 2t$ changes sign along the circular phase space trajectory. The prefactor, eq. (6.72), thereby becomes (Ref. [7, p. 159]):

$$\mathcal{N}_t = c_0 \frac{\exp\left[i \int_0^t d\xi k(\xi) \dot{x}(\xi)\right]}{(-2\pi i)^{\rho/2} \sqrt{\Lambda_{\rho\rho} R_t \det a_{\varsigma\varsigma}}} = c_0 \frac{\exp[i2E(t - \frac{1}{4}\sin(4t))]}{2\sqrt{-\pi i} (2E)^{1/4} |\cos(2t)|^{1/2} e^{i\varphi/2}}, \quad (7.21)$$

where

$$\varphi = \left\lfloor \frac{4t - \pi}{2\pi} \right\rfloor \pi = \arg B_t = \arg[-\cos(2t)].$$

is the argument of B_t restricted to be monotonically increasing (the argument increases in increments of π since $B_t \in \mathbb{R}$).

With eq. (6.71) the transformed phase space coordinates becomes (Ref. [7, p. 160]):

$$\mathbf{Z}_t(\tau) = \mathbf{S}_t \mathbf{z}(\tau) = \begin{bmatrix} -\sin 2t & -\cos 2t \\ \cos 2t & -\sin 2t \end{bmatrix} \sqrt{2E} \begin{pmatrix} \cos 2\tau \\ -\sin 2\tau \end{pmatrix} = \sqrt{2E} \begin{pmatrix} \sin(2\tau - 2t) \\ \cos(2\tau - 2t) \end{pmatrix}. \quad (7.22)$$

The Jacobian in the rotated phase space is obtained from eq. (6.74):

$$J_t(\tau) = \dot{X}_t = 2\sqrt{2E} \cos(2(\tau - t)) = 2K_t(\tau). \quad (7.23)$$

the envelope is given by eq. (6.73):

$$\Phi_t(\tau) = \sqrt{\frac{J_t(t)}{J_t(\tau)}} = \sqrt{\frac{K_t(t)}{K_t(\tau)}} = [\cos(2(\tau - t))]^{-1/2}, \quad (7.24)$$

where I used $K_t(t) = \sqrt{2E}$. We obtain the phase from eq. (6.75):

$$\Theta_t(\tau) = \int_t^\tau d\xi \dot{X}_t(\xi) K_t(\xi) = 2E \int_t^\tau 2 \cos^2(2(\xi - t)) \quad (7.25)$$

$$= 2E \left[\frac{1}{2} \cos(2(\tau - t)) \sin(2(\tau - t)) + (\tau - t) \right]. \quad (7.26)$$

Now, I isolate τ in eq. (7.22) to obtain:

$$\tau - t = \frac{1}{2} \sin^{-1} \left(\frac{X_t}{\sqrt{2E}} \right), \quad \cos(2(\tau - t)) = \sqrt{1 - \frac{X_t^2}{2E}}, \quad \sin(2(\tau - t)) = \frac{X_t}{\sqrt{2E}}. \quad (7.27)$$

Next, I note that $X_t(t) = 1$ and therefore $\epsilon := X_t - X_t(t) = X_t$. Therefore, inserting eq. (7.27) into eqs. (7.24) and (7.25) gives the eikonal fields:

$$\Phi_t(\epsilon) = \left(1 - \frac{\epsilon^2}{2E} \right)^{-1/4}, \quad (7.28)$$

$$\Theta_t(\epsilon) = \frac{\epsilon}{2} \sqrt{2E - \epsilon^2} + E \sin^{-1} \left(\frac{\epsilon}{\sqrt{2E}} \right), \quad (7.29)$$

$$\Psi_t(\epsilon) = \Phi_t(\epsilon) \exp[i\Theta_t(\epsilon)]. \quad (7.30)$$

Finally, for the combined phase function, f , of eq. (6.78b) I need to determine:

$$\begin{aligned} -\frac{1}{2} \frac{A_t}{B_t} \epsilon^2 - K_t(t) \epsilon &= -\frac{1}{2} \tan(2t) \epsilon^2 - [-B_t x(t) + A_t k(t)] \epsilon \\ &= -\frac{1}{2} \tan(2t) \epsilon^2 - \frac{x^2(t) + k^2(t)}{\sqrt{2E}} \epsilon = -\frac{1}{2} \tan(2t) \epsilon^2 - \sqrt{2E} \epsilon. \end{aligned}$$

Therefore $f_t(\epsilon)$ is:

$$f_t(\epsilon) = \frac{\epsilon}{2} \sqrt{2E - \epsilon^2} + E \sin^{-1} \left(\frac{\epsilon}{\sqrt{2E}} \right) - \frac{1}{2} \tan(2t) \epsilon^2 - \sqrt{2E} \epsilon. \quad (7.31)$$

The final solution is obtained by multiplying the prefactor of eq. (7.21) with the inverse metaplectic transformed field, Υ_t from eq. (6.78):

$$\Upsilon_t = \int_{C_0} d\epsilon \Phi_t(\epsilon) \exp[i f_t(\epsilon)] \quad (7.32)$$

At this point in Ref. [7], Nicolas Alexander Lopez notes that the only time dependent term in $\Phi_t(\epsilon)$ and $f_t(\epsilon)$ is the term with $\tan(2t)$, which is π -periodic in time. This gives the quantization familiar from the QHO:

$$E = \nu + \frac{1}{2}, \quad \nu \in \mathbb{Z}. \quad (7.33)$$

Also note, that the $\tan(2t)$ term has a singularity whenever $B_t = -\cos(2t) = 0$, i.e. when $t = \frac{\pi}{4} + \frac{\pi}{2}n$, $n \in \mathbb{Z}$. This is exactly the singularity which the SVD of B_t addresses and the reason for using eq. (6.79) rather than eq. (6.78). This concludes the analytic derivation for Weber's equation and I will now move on to the numerical results.

7.2.2 Numerical Results for Weber's Equation

I will present the numerical results from Weber's equation in the same manner I presented the results from the Airy problem on figs. 7.1 to 7.3. First, on fig. 7.4 I show the eikonal fields at five different time points in rotated phase space for the ground state of the QHO, i.e. the Weber equation with $\nu = 0$. Figure 7.4 (a) shows the ray manifold in (x, k) space. To follow the definition from [7] I started the ray at time $t = -\frac{\pi}{2} \approx -1.57$ and traced the ray until it reached a full cycle which happened at time $t \approx \frac{\pi}{2}$. On fig. 7.4 I only show plots from the first half of the cycle. As expected analytically from eq. (7.18) the ray trace is a perfect circle of radius $\sqrt{2E_0} = 1$. The caustics in (x, k) space are met at $t = -\pi/2, 0, \pi/2$, where the slope $\partial_x k(x) = \partial_\tau k(\tau)/\partial_\tau x(\tau)$ of the ray manifold becomes infinite. Since the trajectory in (x, k) -space is circular, the rotated manifold in fig. 7.4 (b) is also a (semi)circle. Note, that on fig. 7.4 (b) I only plot the current branch in rotated phase space. The branch is defined by having constant sign of the Jacobian J_t from eq. (7.23) and is therefore terminated where the slope $\partial_{X_t} K_t(X_t)$ of the ray manifold in rotated phase space becomes infinite. This is why the rotated ray manifold of fig. 7.4 (b) in general is a semicircle rather than a circle. Furthermore, for the first quarter of a cycle we have not yet traced an entire semicircle and therefore the rotated trajectories in fig. 7.4 (b) is less than a semi-circle at the first two shown time points, $t = -1.57$ and $t = -1.18$. On fig. 7.4 (c)-(e) I compare the numerically calculated eikonal fields Φ_t, Θ_t, Ψ_t with the analytic results from eqs. (7.28) to (7.30). In all three instances there is excellent agreement between the numerical and analytic results. On fig. 7.4 (e) I note how the caustics at $t = -\pi/2$ and at $t = 0$ have been successfully resolved; I.e. the field does not diverge in the neighbourhood of $\epsilon = 0$. In general, when we have sufficient information available the envelope $\Phi_t(\epsilon)$ and the field $\Psi_t(\epsilon)$ has two singularities at $\epsilon = \pm\sqrt{2E} = \pm 1$ in agreement with eq. (7.28). These singularities of course correspond to the two caustics of the semicircular ray manifold branch in the rotated phase space.

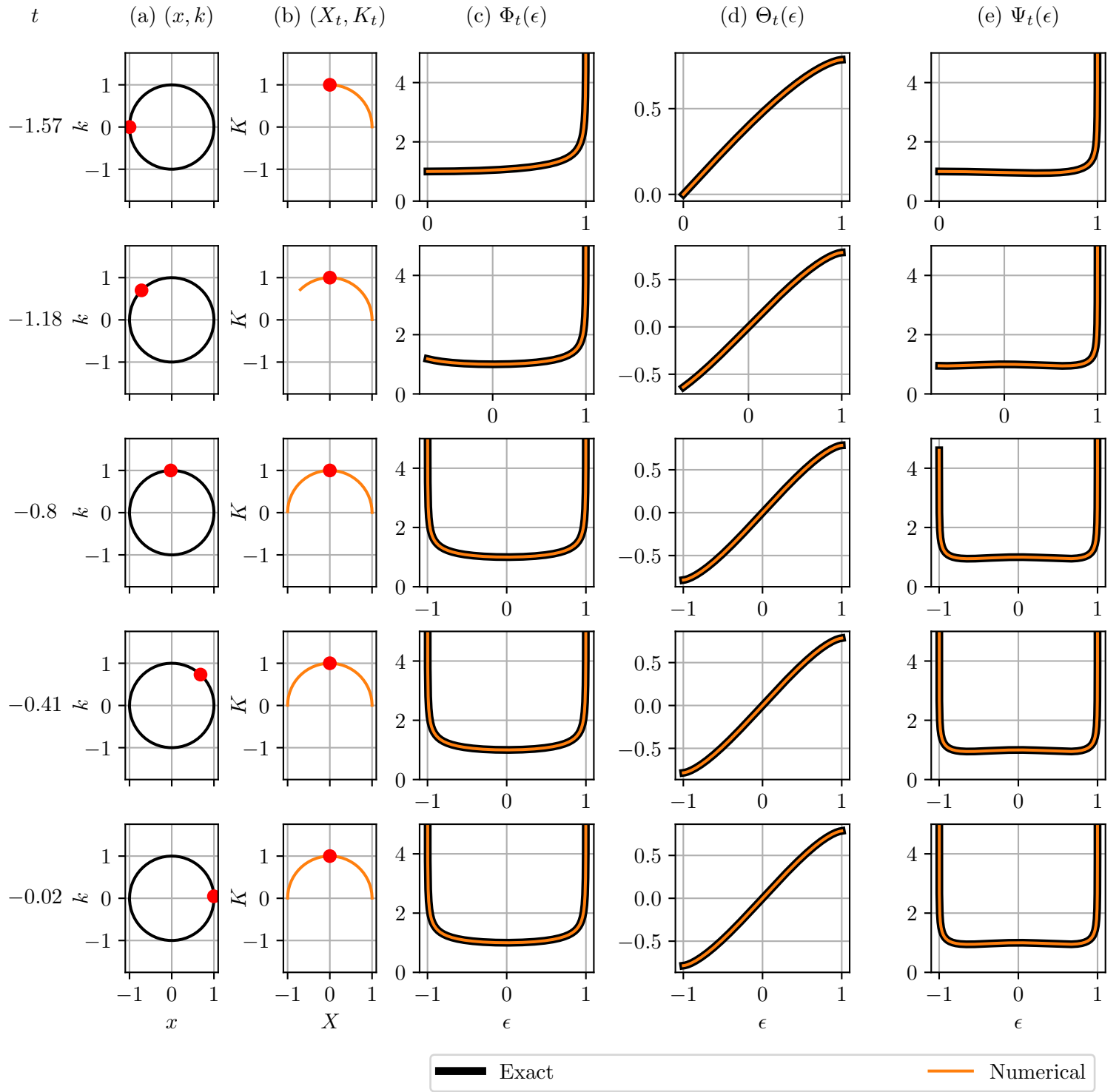


Figure 7.4: Illustration of the MGO algorithm at different time points for the Weber equation example with $\nu = 0$. (a) Ray manifold with red dot indicating phase space location at time t , (b) Current branch of symplectically transformed ray manifold, (c)-(e) Metaplectically transformed fields corresponding to symplectic transformation at time t : (c) eikonal envelope, (d) eikonal phase, (e) eikonal wave field. For (c)-(e) I have shown both the exact closed-form MGO result from eqs. (7.28) to (7.30) and the result from my numerical implementation. The ray tracing started at $t = -\pi/2$ and was automatically stopped after 1 cycle (at time $t \approx \pi/2$). Due to spatial constraints, I have only shown steps from the first half of the cycle.

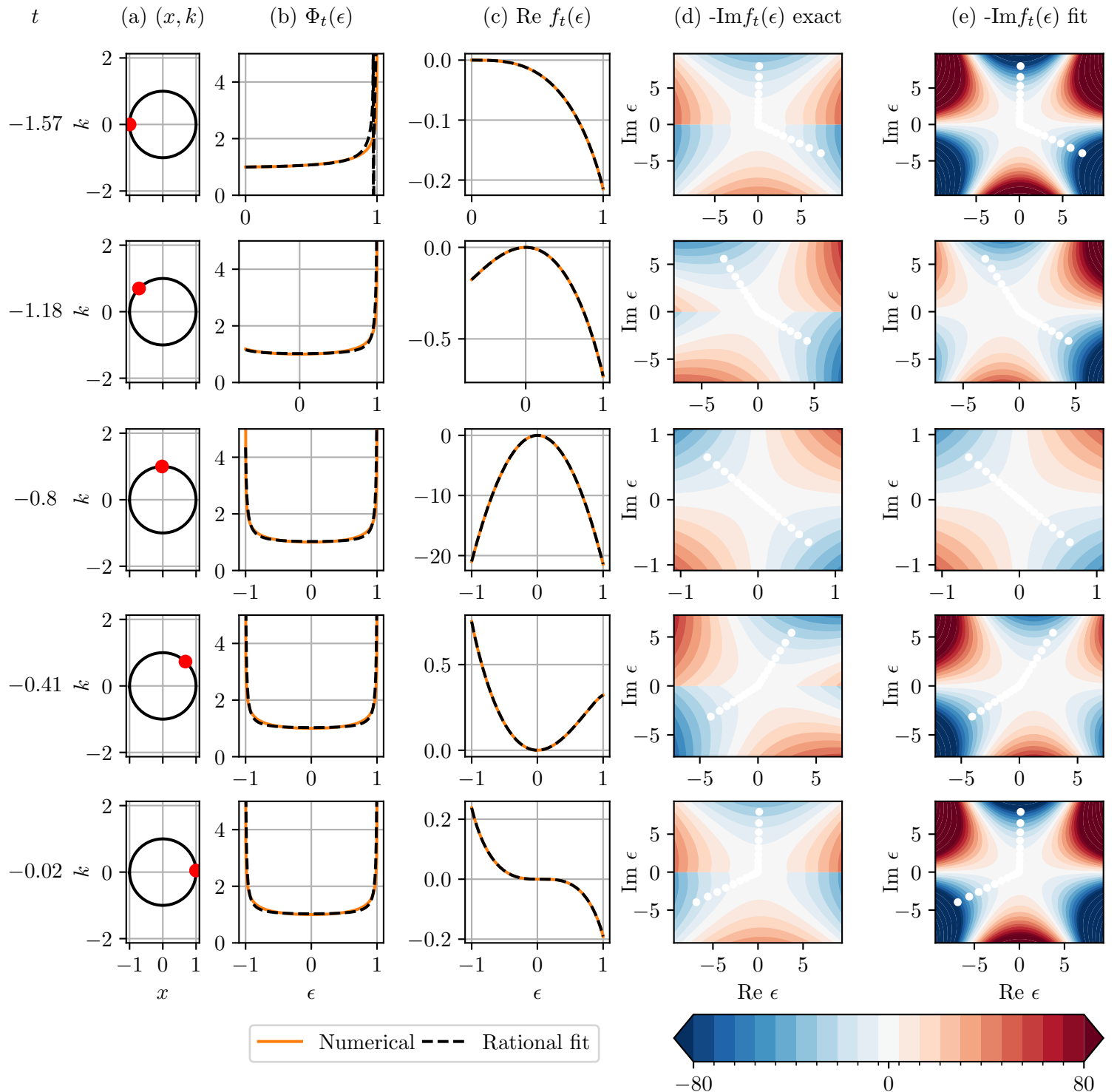


Figure 7.5: Inspection of fits needed for the analytic continuation in order to evaluate the steepest descent integral as part of the inverse metaplectic transform step for the Weber equation example with $\nu = 0$. (a) Ray manifold with red dot indicating phase space location at time t , (b)-(c) Metaplectically transformed envelope, g , and phase factor, f , as a function of $\epsilon = X_t - X_t(t) \in \mathbb{R}$, (d) exact “-Im” part of the analytically continued phase factor from eq. (7.31) evaluated on $\epsilon \in \mathbb{C}$, (e) fit of f evaluated on $\epsilon \in \mathbb{C}$. For both (b) and (c) I have included the numerical result (which in Figure 7.4 was found to agree with the exact result along $\text{Re } \epsilon$), and the rational function fit with (nominator, denominator)-degrees: $(L_\Phi, M_\Phi) = (2, 2)$ and $(L_f, M_f) = (6, 3)$. For (d) and (e) I have also shown the Gauss quadrature node loci along the steepest descent contour used to evaluate the integral of the inverse metaplectic transform.

Moving on, on fig. 7.5 I inspect the rational function fits needed for the analytic continuation to calculate the steepest descent integrals of eq. (7.32). On fig. 7.5 (b)-(c) I show $\Phi_t(\epsilon)$ and $f_t(\epsilon)$ as a function of $\epsilon = X_t - X_t(t) \in \mathbb{R}$. I show both the numerical results and rational function fit with (nominator, denominator) degrees $(L_\Phi, M_\Phi) = (2, 2)$ and $(L_f, M_f) = (6, 3)$. The fit of $\Phi_t(\epsilon)$ on fig. 7.5 (b) appears to agree well with the numerical data except for a misplaced singularity closed to $\epsilon = 1$ which is visible at the starting time point $t = -1.57$. By experimenting with the choice of degrees of the rational function one might avoid this behaviour, but I found it to be a general problem of the rational function fits that they might produce such spurious singularities within the branch domain. On fig. 7.5 (c) it is difficult visually to discern the rational fit from the numerical values of $f_t(\epsilon)$. Nevertheless, when we extend the rational fit to the complex plane in fig. 7.5 (e) and compare this with the exact contour plot of fig. 7.5 (d) obtained from eq. (7.31) we do in fact see a visual difference. Away from $x = 0$ and towards the caustics at $x \rightarrow \pm 1$, the fit from numerical data on fig. 7.5 (e) deviates more and more from the exact contour plot on fig. 7.5 (d). Fortunately, all fits have the correct qualitative behaviour in the complex plane; I.e. the directions of ascents and descents are close to the same for the numerical and exact contour plots. I have indicated the Gauss-Freud quadrature nodes along the numerically obtained steepest descent line paths on both fig. 7.5 (d) and fig. 7.5 (e). Especially for the plot at time $t = -1.18$, the straight line approximation deviates visually from the apparently curved true path of steepest descent. To summarize, fig. 7.2 highlights two potential issues in my current numerical implementation: First, the rational function fits do not agree perfectly with the numerical data and this makes the analytic continuation more inaccurate. Second, the straight line contour deviates slightly from the true curved steepest descent contour. Finally, as a third related and important point; Though not visible from fig. 7.5, the quality of my rational function fits is quite sensitive to the choice of fitting parameters (i.e. degrees in the rational functions) and this may influence the final solution significantly. I will return to this discussion in a later section.

Having analyzed the steps in the numerical MGO implementation, I am now in a position to perform the integration in eq. (7.32), calculate the prefactor in eq. (7.21), interpolate along each branch and superpose the branch contributions according to eq. (6.80). Doing all of this numerically yields the final result shown in fig. 7.6 for the energy levels $\nu = 0, 1, 2, 3$. On this figure, I present the exact result from eq. (5.17) together with the GO result from fig. 5.6 and the result of applying the numerical MGO algorithm in two different ways. For the solution labeled MGO (I) on fig. 7.6 I have used rational function fits with (nominator, denominator)-degrees $(L_\Phi, M_\Phi) = (2, 2)$ and $(L_f, M_f) = (6, 3)$. This is exactly the fits which I inspected on fig. 7.5 with $\nu = 0$. For comparison, the solution labeled MGO (II) uses more accurate non-linear fits on the form of the exact analytic expressions in eqs. (7.28) and (7.31). This is to illustrate the error introduced by the rational function fitting. When applying the numerical MGO algorithm, fitting with rational functions of course requires less supervision compared to manually deriving the form of Φ_t and f_t analytically. An important motivation of MGO is precisely to implement a fully automated field reconstruction algorithm and therefore the rational

function fit approach is to be preferred if it gives acceptable accuracy.

As a general conclusion, the MGO solutions on fig. 7.6 match the true wave functions well and, as opposed to the GO solutions, solves the problem of having non-finite wave fields at the caustics $x = \pm\sqrt{2E}$. For the higher energy levels $\nu = 2$ and $\nu = 3$ it is difficult to visually discern the exact results of eq. (5.17) from the numerical MGO results. Of course, just like GO, MGO in its' current formulation is limited to only provide solutions in the non-evanescent region. At the first excited state with $\nu = 1$ the red-curve MGO (II) solution using non-linear fits agrees very well with the exact result. The same could be said for the more automated MGO (I) solution using rational fits had it not been for a minor error close to the first caustic, $x = -\sqrt{2E_1} \approx -1.73$. For the ground state with $\nu = 0$, there is a visually discernible error in both of the numerical MGO results compared to the exact ground state wave function. It is noticeable how the difference between the red MGO (II) curve and the exact result is most exaggerated close to $x = 0$, exactly the region where B_t from eq. (7.20) vanishes. Even though I have used the SVD formulation from eq. (6.79) in my numerical implementation, it is natural to suspect that the error is related to the singularity of the current MGO representation at $B_t = 0$. In Ref. [7], Nicolas Alexander Lopez presents an entirely new formulation of MGO based on Gaussian coherent states which is free from singularities at $B_t = 0$ and should therefore solve this problem. It would be interesting to investigate this formulation of MGO further in a future work. Alternatively, some of the error may also be explained by the straight-line approximation to the true steepest descent path and the limited number ($n = 10$) of Gauss-Freud quadrature nodes. Meanwhile, the difference between the blue MGO (I) curve and the red MGO (II) curve must be prescribed to the error of the rational function fits. It is interesting to see that the error between the exact and numerical values of $f_t(\epsilon)$ in the complex plane which I observed at time $t = -0.02$ in fig. 7.5 (d) and (e) does not manifest itself as a significant difference between the MGO (I) and MGO (II) results at position $x = 1$. This suggests, that I can trust the MGO results as long as the fits agree well with the numerical data on the real axis of ϵ . As was the case for $\nu = 1$, there is however a spurious numerical error close to the first caustic, $x = -\sqrt{2E_0} \approx -1$, for the blue-curve MGO (I) ground state result. This numerical error is most likely caused by the poor fit of $\Phi_t(\epsilon)$ seen at $t = -1.57$ on fig. 7.4. To investigate the error introduced by my rational function fit approach further, I have plotted fig. 7.7 which I will now present.

Thus far, all results on figs. 5.5, 7.1, 7.2 and 7.4 to 7.6 have used fit parameters (i.e. nominator/denominator degrees) for the rational functions which were manually hand picked as those parameters which gave the most accurate fitting of Φ_t and f_t . Figure 7.7 shows ground state MGO solutions of the Weber equation with $\nu = 0$ with different nominator/denominator degrees for the rational fits as part of the analytic continuation. For each solution, I have calculated the root mean square (RMS) error between the exact $\psi_0(x)$ and numerical MGO result. The 9 solutions which are labeled in the legend and fully opaque in the plot are the fits with the lowest RMS error. None of the 9 labeled MGO solutions fit the exact function without error, but with an RMS below 0.2

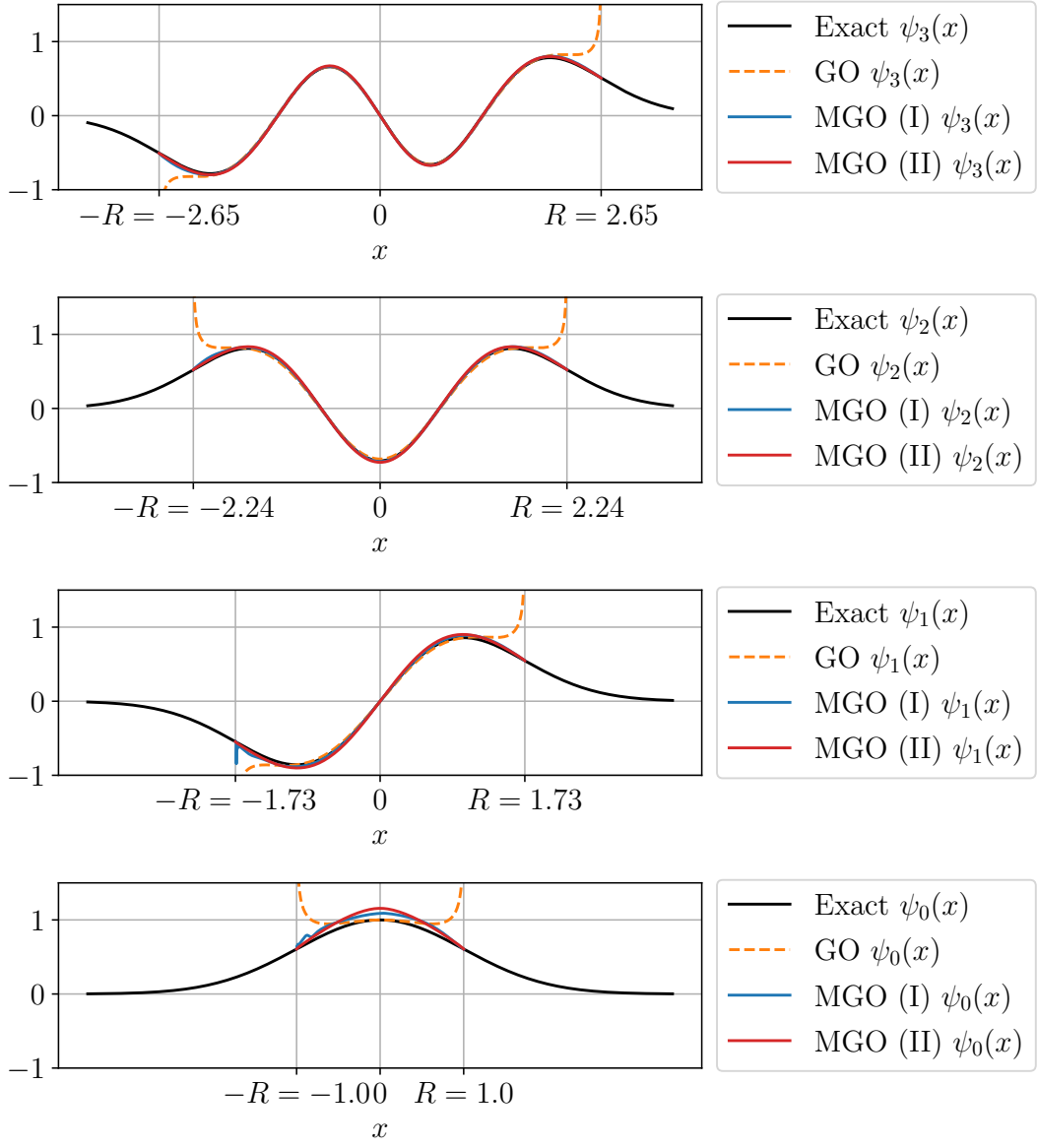


Figure 7.6: MGO solutions to Weber's Equation, eq. (5.16 We), for four different orders $\nu = 0, 1, 2, 3$. For each ν , I have shown the exact wave function, eq. (5.17), the GO approximation and solutions from two different ways of applying the MGO algorithm. $R = \sqrt{2E}$ denotes the radius of the classical (non-evanescent) region of the QHO. For MGO (I), I used rational function fits with (nominator, denominator)-degrees $(L_\Phi, M_\Phi) = (2, 2)$ and $(L_f, M_f) = (6, 3)$ to perform the analytic continuation. For MGO (II) I used non-linear fits with the forms given from the exact analytic expressions in eqs. (7.28) and (7.31).

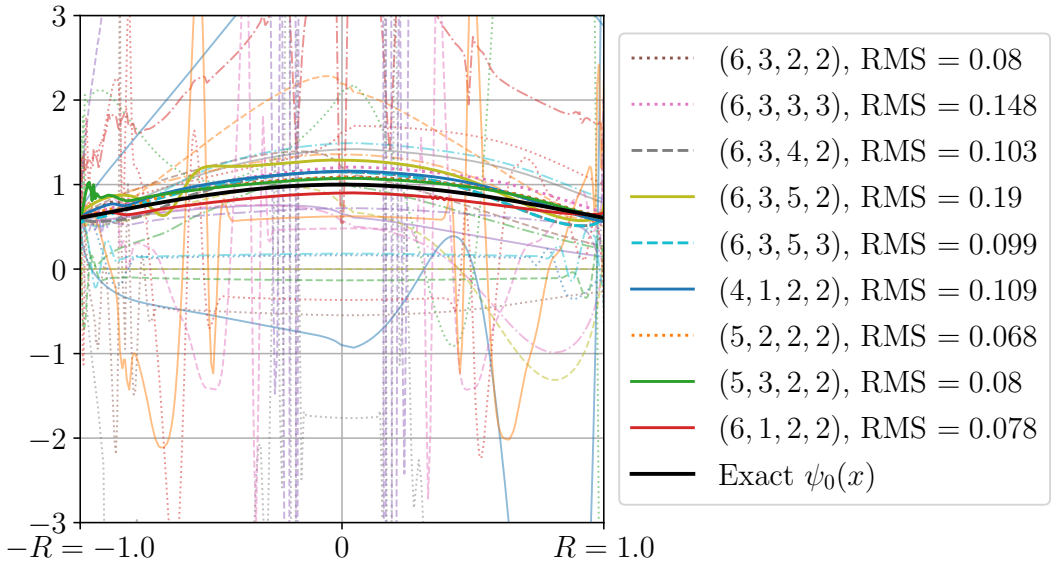


Figure 7.7: Examples of MGO solutions to Weber’s Equation, eq. (5.16 We), with different fitting parameters in the rational function fits used for the analytic continuation. The tuples in the legend denotes the rational function fit parameters in the order $(L_f, M_f, L_\Phi, M_\Phi)$ where L denotes the nominator degree of the rational function and M denotes the denominator degree. I have only labeled the best 9 solutions and written the root mean square error of these (compared to the exact solution). Behind the labeled solutions are also shown worse-performing examples to illustrate the sensitiveness of the results on the choice of fitting parameters. $R = \sqrt{2E}$ denotes the radius of the classical (non-evanescent) region of the QHO.

they all fit the solution reasonable well except for numerical issues close to the caustic for some. Behind the fully-opaque labeled solutions I have also included more transparent lines corresponding to worse-performing solutions. There are too many lines to really discern the individual solutions from each other, but the plots nevertheless illustrates the great variety in solutions obtained when changing the parameters of the fits for the analytic continuation. The really problematic solutions which appear entirely unstable correspond to the cases where the rational function fits of $\Phi_t(\epsilon)$ had singularities within the branch domain $\epsilon \in [-1, 1]$. This problem can be counteracted by performing a non-linear optimization on top of the linear least square method used to fit the rational functions, but I found that this procedure significantly increased the time to run the MGO algorithm. This discussion of fig. 7.7 generally shows that my numerical implementation in its’ current state is quite unstable due to its’ sensitivity to the choice of fitting parameters. However, there are many strategies one could try out to alleviate the issue. For instance, one could make a simple automated procedure to find the best fitting parameters for the rational function fits before running the entire MGO algorithm. Al-

ternatively, one could regularize the fits (using either polynomial or rational functions) by also fitting to the derivatives of Φ_t, f_t to avoid over-fitting. A third and perhaps best option might be to find a way to avoid the fitting all together and calculate $\Phi_t(\epsilon), f_t(\epsilon)$ in the complex plane directly. However, exploring these strategies is not within the scope of this thesis project.

This concludes the presentation of the numerical MGO results for Weber's equation. All in all, this first numerical implementation of the MGO algorithm has successfully reproduced the exact wave functions with a good accuracy, especially for higher orders, and with minor improvements the method can only become even better.

7.3 X-B Coupling at the upper hybrid layer in a warm plasma

As a final example of applying the numerical implementation of the MGO algorithm I will consider the coupling of X-mode waves to electron Bernstein waves (EBWs) at the UH resonance. The EBW is a mode which does not appear within the cold plasma theory of chapter 2, but instead depends on the inclusion of kinetic effects (Ref. [46]). EBWs are electrostatic modes propagating perpendicular to the background magnetic field (Ref. [47]). The dispersion branches of the X-mode and EBW modes combine close to the UH layer, thereby allowing for conversion between the modes (Ref. [47]). As is common I shall call the coupling between the modes for XB coupling. To describe the waves I use the model from Ref. [46], but instead of making a series expansion of the electrostatic dispersion relation, I use the form of Ref. [48]. The dispersion symbol I consider therefore is:

$$\mathcal{D}(x, k, \omega) = K_1(x, k, \omega)k^2 - \left(\frac{\omega}{c}\right)^2(S^2 - D^2) \quad (7.34a)$$

$$K_1 = 1 + \frac{\omega_{pe}^2}{\omega_{ce}^2} \exp(-\lambda) \int_0^\pi d\psi \frac{\sin\left(\psi\left(\frac{\omega}{\omega_{ce}}\right)\right) \sin(\psi) \exp(-\lambda \cos(\psi))}{\sin\left(\pi\left(\frac{\omega}{\omega_{ce}}\right)\right)} \quad (7.34b)$$

$$S = 1 - \frac{\omega_{pe}^2(x)}{\omega^2 - \omega_{ce}^2}, \quad D = \frac{\omega_{ce}}{\omega} \frac{\omega_{pe}^2}{\omega^2 - \omega_{ce}^2} \quad (7.34c)$$

$$\lambda = \frac{v_{Te}^2}{2\omega_{ce}^2} k_x^2, \quad v_{Te}^2 = \frac{2T_e}{m_e} \quad (7.34d)$$

$$\omega_{pe}^2(x) = \frac{e^2}{\epsilon_0 m_e} n_e(x), \quad \omega_{ce} = \frac{e B_0}{m_e}, \quad (7.34e)$$

where for convenience I have repeated the fundamental quantities. The scenario I'm considering simulates the conditions close to the UH layer in the MAST-Upgrade machine located at Culham in Oxfordshire, England. The UH layer resides between the second and third electron cyclotron harmonic. The density is assumed to be linear with parameters:

$$n_e(x) = n_0(1 - x/\ell_n), \quad n_0 = 2.07 \times 10^{19} \text{ m}^{-3}, \quad \ell_n = 0.284 \text{ mm} \quad (7.35)$$

The B -field is assumed constant with magnitude:

$$B_0 = 0.511 \text{ T}. \quad (7.36)$$

For the temperature, I will consider both the case of a linear and a constant temperature profile:

$$T_e(x) = T_0(1 - x/\ell_T), \quad T_0 = 38.5 \text{ eV}, \quad \ell_T = 0.207 \text{ mm} \quad (7.37)$$

$$\text{Alternatively with constant temperature: } T_e(x) = T_0 \quad (7.38)$$

The source has a frequency of $f(t = 0) = 34.8 \text{ GHz}$. From the dispersion relation I thereby obtain the initial condition:

$$(k_0, f_0) = (0.159 \text{ mm}^{-1}, 34.8 \text{ GHz}) \quad \text{or} \quad (7.39a)$$

$$(k_0, \omega_0) = (0.159 \text{ mm}^{-1}, 2.187 \times 10^{11} \text{ s}^{-1}). \quad (7.39b)$$

On fig. 7.8 I have shown a plot of the dispersion surface where $\mathcal{D}(x, k, \omega) = 0$ in (k, f) -space (where $f = \frac{\omega}{2\pi}$ is the frequency). I have indicated with a red dot the initial (k_0, f_0) value for the ray trace. The trace starts out on the X-mode branch. The X-mode branch has positive group velocity (i.e. a positive slope in (k, f) -space) and is the same branch as the one predicted from a cold treatment of the plasma dispersion relation. However in a cold treatment, the X-mode branch would normally flatten out, but in this case we instead see that the X-mode connects to EBW branches. The EBW branches only occur when including kinetic effects in the derivation of the dispersion relation.

As can be seen on fig. 7.8, the initial X-mode branch connects with the EBW branch at the point where the group velocity goes to zero. This point is the UH layer. Within cold plasma theory, the UH layer is a resonance, but in a warm treatment with kinetic effects, the layer only gives a finite amplification of the incoming X-mode. The fact that the X- and EBW branches connect means, that the incoming initial X-mode wave (which has a positive group velocity) will be amplified and at the UH layer couple to the outgoing EBW mode (which has a negative group velocity but also a positive wave number $k > 0$).

On fig. 7.9 is seen the solution of tracing and field reconstruction for the dispersion relation of eq. (7.34) with a constant temperature profile, eq. (7.38). On fig. 7.9 (a) I show the solution within GO, on fig. 7.9 (b) the MGO solution and on fig. 7.9 (c) I show the ray phase space trajectory. First, note on fig. 7.9 (c) how the ray starts with a very small initial k and then reaches the UH layer at about $x \approx 12.5$. At this point, the X-mode continues a bit further in the evanescent region before turning into an EBW mode. The caustic is met at $x \approx 15.5$ and the outgoing branch of the ray manifold is the EBW branch which has a very high wave number (k up to 50 mm^{-1}) compared to the incoming X-wave (which has $k_0 = 0.159 \text{ mm}^{-1}$). The object of interest for the study of parametric decay instabilities is the amplitude gain and the initial phase of the electric field is therefore irrelevant. For this reason, together with the physical field $E(x)$

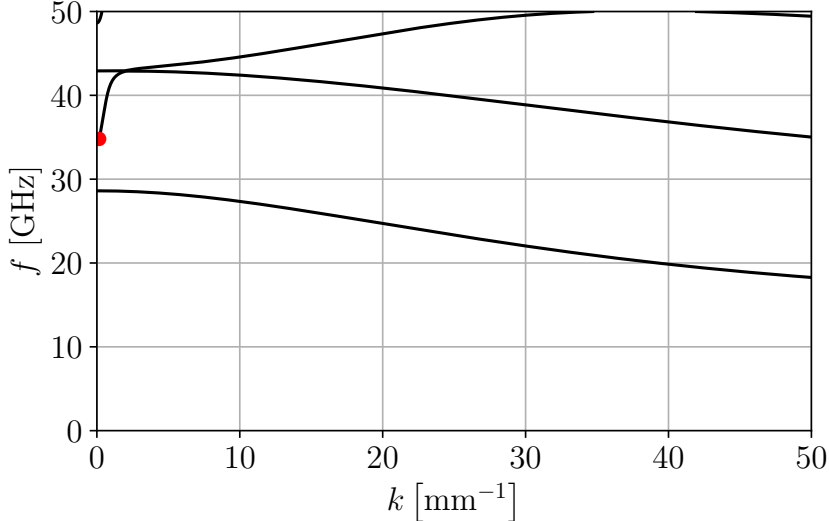


Figure 7.8: Overview of branches satisfying the XB coupling dispersion relation, eq. (7.34), in frequency and (transverse) wave number space. The red dot indicates the (k_0, f_0) value of eq. (7.39) used as initial condition for the ray tracing. The initial branch with positive slope (i.e. positive group velocity) is the X-mode branch also found in cold plasma treatments

I have also plotted the complex field amplitude $\pm |\tilde{E}(x)|$ where $E(x) = \text{Re}\{\tilde{E}(x)\}$. The complex field amplitude corresponds to the maximal envelope obtained when varying the initial phase of the electric field and can therefore be used to estimate the field amplification in a general setting, where the initial phase is irrelevant.

On fig. 7.9 (a) the GO solution is seen to diverge at the caustic. This is both reflected in the complex field amplitude going to $\pm\infty$ and in the real field diverging. The initial amplitude was set to $E(0) = 1$ and from the GO-solution we should therefore predict an infinite amplification which is of course unrealistic. Judging from the GO field amplitude shortly before the caustic, the true amplification factor might be a factor of 2 or 3, but it is difficult to tell due to breakdown of the eikonal approximation at the caustic. In contrast hereto, the MGO solution on fig. 7.9 (b) does not diverge at $x = 15.5$ as we would hope for. Judging from the highest crest of the MGO solution the field amplification is about a factor of 2.7. The GO and MGO solutions look qualitatively alike in that they have a slow modulation to begin with which is turned into a rapid oscillation close to the caustic. However, the two solutions do not agree in terms of the exact field values, neither away from the caustic or close to it.

To inspect the solution of the XB-coupling with constant temperature profile further, I consider the ingoing and outgoing field separately on fig. 7.10. As before, (a) is the GO

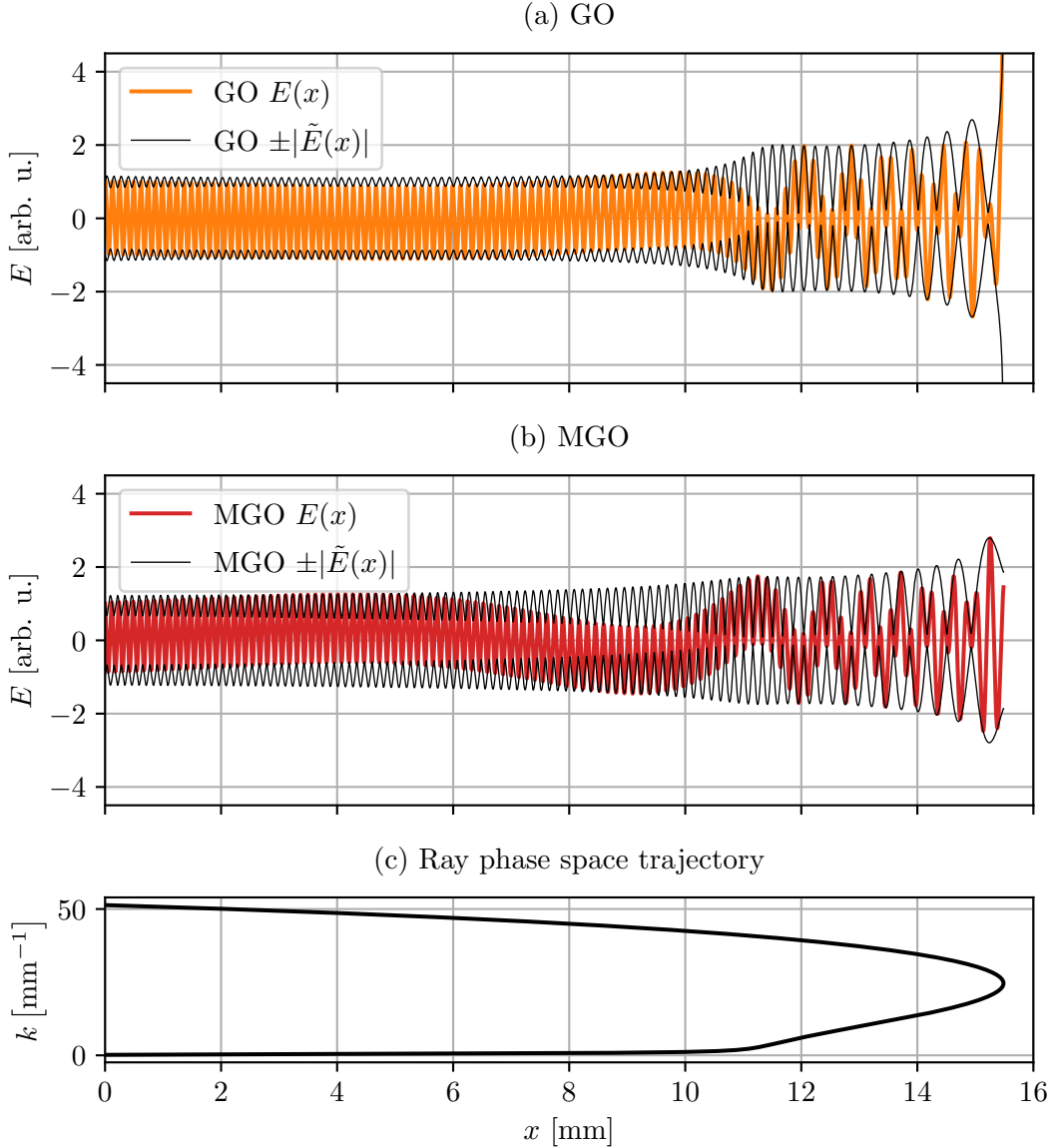


Figure 7.9: MGO field solutions for the XB coupling at the UH layer governed by eqs. (7.34) to (7.36) and (7.38) with a **constant temperature profile**. (a) GO approximation, (b) MGO approximation, (c) Ray phase space trajectory constituting the ray manifold. For (a) and (b) I have shown both the field, $E(x)$, and the amplitude, $|\tilde{E}(x)|$, of the complex field representation (i.e. $E(x) = \text{Re } \tilde{E}(x)$). For the MGO algorithm, I used rational function fits with (nominator, denominator)-degrees, $(L_f, M_f) = (4, 1), (L_\Phi, M_\Phi) = (2, 1)$ to perform the analytic continuation.

solution and (b) the MGO solution. On both fig. 7.10 (a) and (b) the incoming X-wave is black and the outgoing EBW is coloured. Figure 7.10 shows how, for both the GO and MGO solution, the incoming X-wave has a long wavelength due to its' low wave number, whereas the outgoing EBW is rapidly oscillating in agreement with the high outgoing k -values. While the EBW branch is almost constant for $x \lesssim 12$ mm, the X-wave is the source of the initial slow modulation of the combined wave. It also appears from fig. 7.10 that the difference between the GO and MGO solutions is found in the X-wave.

In the Weber example on fig. 7.7 in section 7.2.2 I showed how the numerical MGO implementation in its' current state is very sensitive to errors in the fits influenced by the choice of fitting parameters. The question is of course whether or not we can trust the MGO results of the XB coupling example. To answer this, I show on fig. 7.11 the rational function fits of $\Phi_t(\epsilon)$ and $f_t(\epsilon)$ from eqs. (6.73) and (6.78b) at five different time steps of the MGO algorithm for the current XB coupling example with constant temperature, eq. (7.38). Judging from the plots, the fits have excellent agreement with the numerical data. The only visual error is found at the lowest part of the current branch (i.e. the lowest ϵ -values), where some of the fits does not follow the numerical data exactly. Since it is only the contribution close to $\epsilon = 0$ which is important for MGO, this minor fitting error should not be important. Of course, as we saw in section 7.2.2, even though the fits of $\Phi_t(\epsilon)$ and $f_t(\epsilon)$ look perfect on the real axis of ϵ there might be a greater error in the complex plane. However, as I also discussed in section 7.2.2, judging from the final results of the Weber example in section 7.2.2 on fig. 7.6 I would not expect such a fitting error which is not visible on $\text{Re}\{\epsilon\}$ to give a significant error in the final solution.

The results of figs. 7.9 to 7.11 were all for a constant temperature profile, eq. (7.38). I will now show how the result changes, when I allow the temperature profile to vary linearly according to eq. (7.37). As before, I present the wave field and ray trace on fig. 7.12 for both the GO approximation, fig. 7.12 (a), and the MGO approximation, fig. 7.12 (b). First, note on fig. 7.12 (c) how the ray trace still has a caustic at $x \approx 15.5$ mm. However, as opposed to the case of the constant temperature profile, the ray manifold now also has a turning point at $x \approx 13.2$ mm where k goes from increasing to decreasing. To the best of my knowledge, there is no physical reason why this turning point should be significant, but from an MGO viewpoint it means that the B_t component of the symplectic transformation matrix eq. (6.70) changes sign and thereby crosses 0. Judging from the results of the Weber equation in section 7.2.2, it is reasonable to suspect that this point might also be problematic for this XB-coupling example. On fig. 7.12 (a) the GO solution is seen to propagate with a constant amplitude until it reaches the UH layer where there is an amplification. The amplification is finite at first, but at the caustic the field as usual grows without limits. On fig. 7.12 (b) I show the corresponding MGO result and indeed the caustic problem has been resolved. The MGO field behaves somewhat similar to the GO field up to the UH layer, but unfortunately it has a discontinuous jump close to the point where $B_t \rightarrow 0$. Since the electric field should always be continuous, this rapid change is most likely unrealistic. The fact that it happens at $B_t \rightarrow 0$ suggests

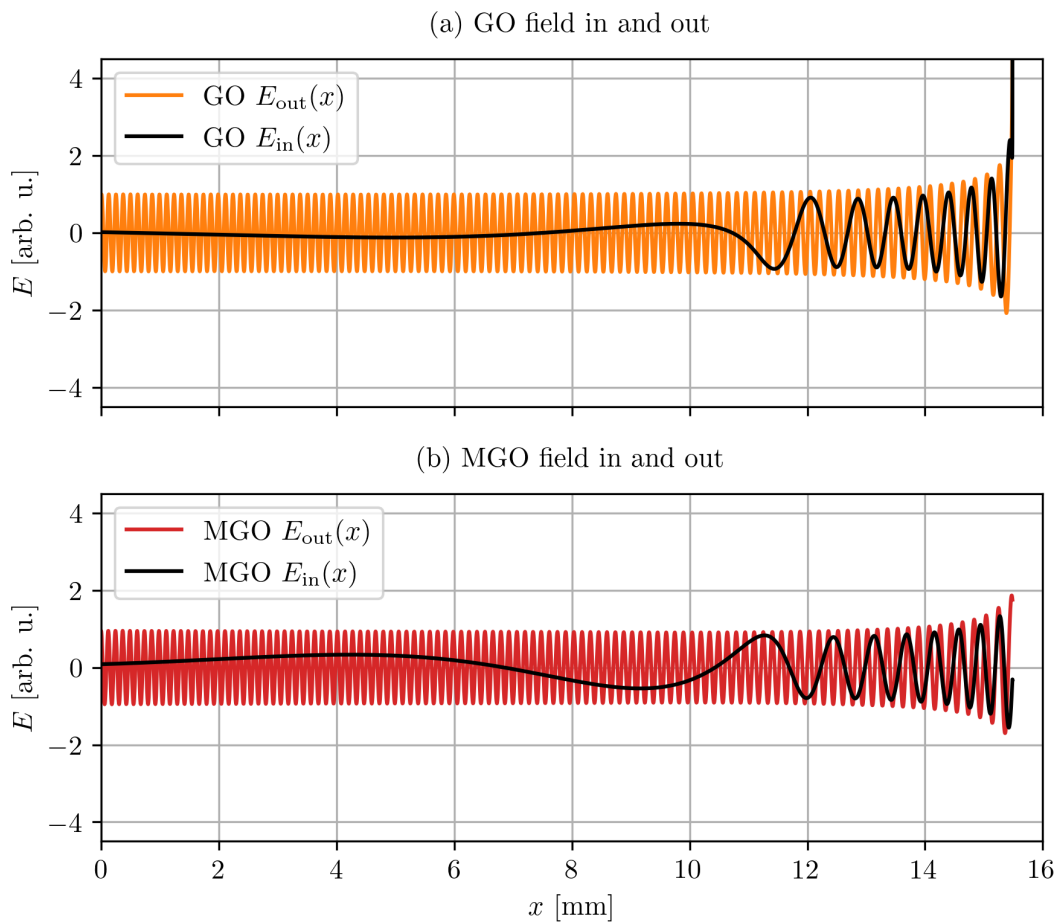


Figure 7.10: Ingoing and outgoing fields for the XB coupling at the UH layer governed by eqs. (7.34) to (7.36) and (7.38) with a **constant temperature profile**. (a) GO approximation, (b) MGO approximation.

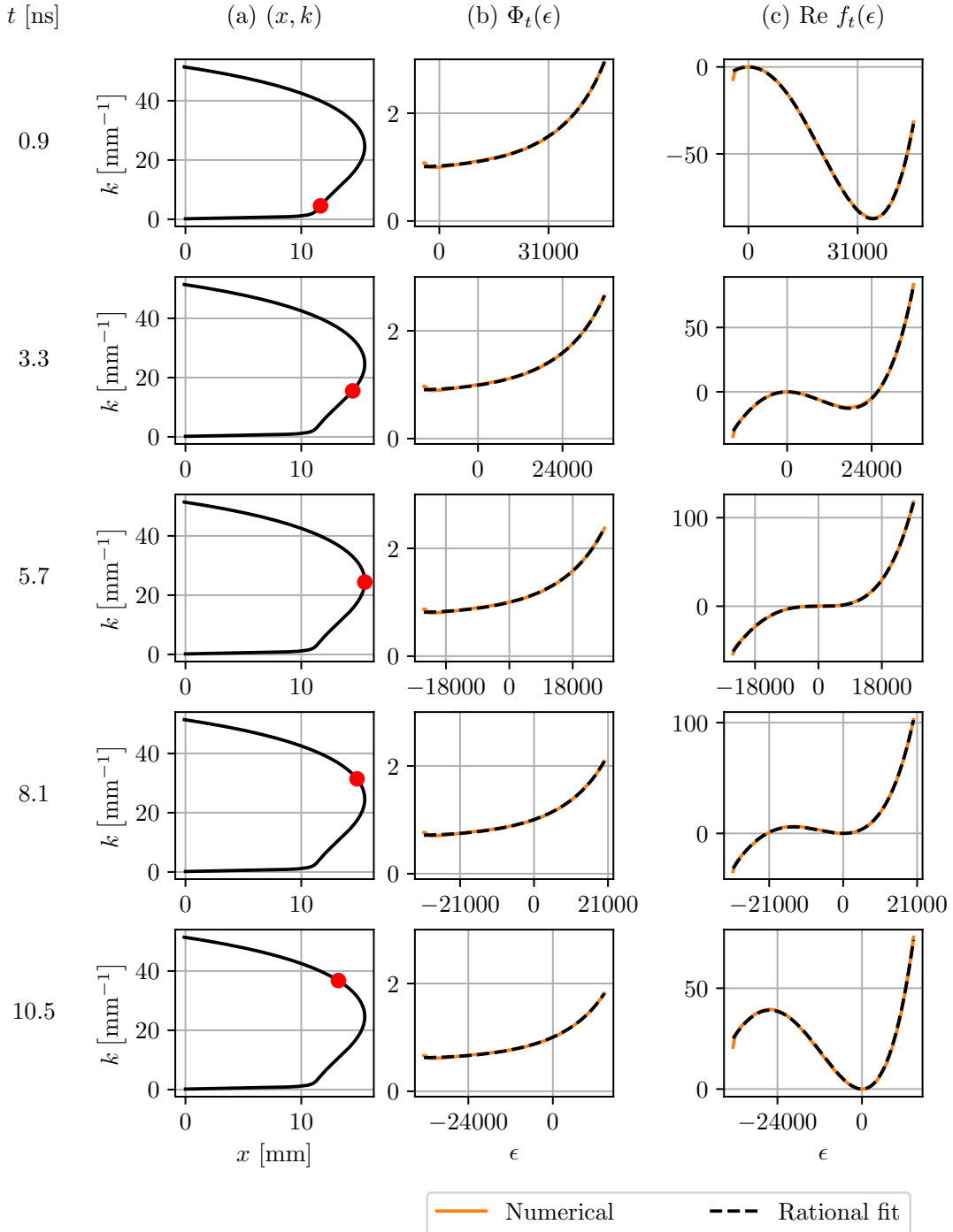


Figure 7.11: Inspection of fits for the XB coupling example with a **constant temperature profile**. (a) Ray manifold with red dot indicating phase space location at time t , (b)-(c) Metaplectically transformed envelope, Φ , and phase factor, f , where I have included the numerical result and the rational function fit with (nominator, denominator)-degrees: $(L_f, M_f) = (4, 1)$ and $(L_\Phi, M_\Phi) = (2, 1)$.

that it might be related to the general singularity problem of the current representation of MGO.

To investigate the matters further I present on fig. 7.13 (a) and (b) the incoming and outgoing GO and MGO fields respectively. The incoming branch appears well-behaved with a slow oscillation, but the outgoing branch of the MGO solution has the discontinuity problem at the point where $B_t \rightarrow 0$.

On fig. 7.14 I inspect the rational function fits of $\Phi_t(\epsilon)$, $f_t(\epsilon)$ at five different time points. The caustic is met at time $t = 10$ ns and the manifold maximum where $B_t = 0$ is met at $t = 18.9$ ns. The fits of $\Phi_t(\epsilon)$ this time clearly introduce a minor error which may be reflected in the final solution. Yet more problematic, at time $t = 18.9$ ns the envelope $\Phi_t(\epsilon)$ appears to have a singularity at $\epsilon = 0$ which is exactly the behaviour we are trying to avoid with the MGO framework. Perhaps this problem can be resolved by increasing the resolution by making the step size of the ray trace smaller in the regions of high curvature of the ray manifold as suggested in Ref. [7, p. 140]. Meanwhile, the fits of $f_t(\epsilon)$ are seen to fit the numerical data well except for the point where $B_t = 0$ at time $t = 18.9$ ns. In summary this analysis suggest three possible explanations behind the problem of the discontinuity seen on fig. 7.12: First, the field in rotated phase space is not free from caustics close to $\epsilon = 0$ at time $t = 18.9$ ns within the current resolution. Second, the rational function fits perform poorly, especially at $t = 18.9$ ns. And finally, the current formulation of MGO might in general be more imprecise whenever $B_t \rightarrow 0$. This last issue may be resolved by the Gaussian coherent state formulation in [7, p. 145].

This concludes the presentation of the main results of this thesis.

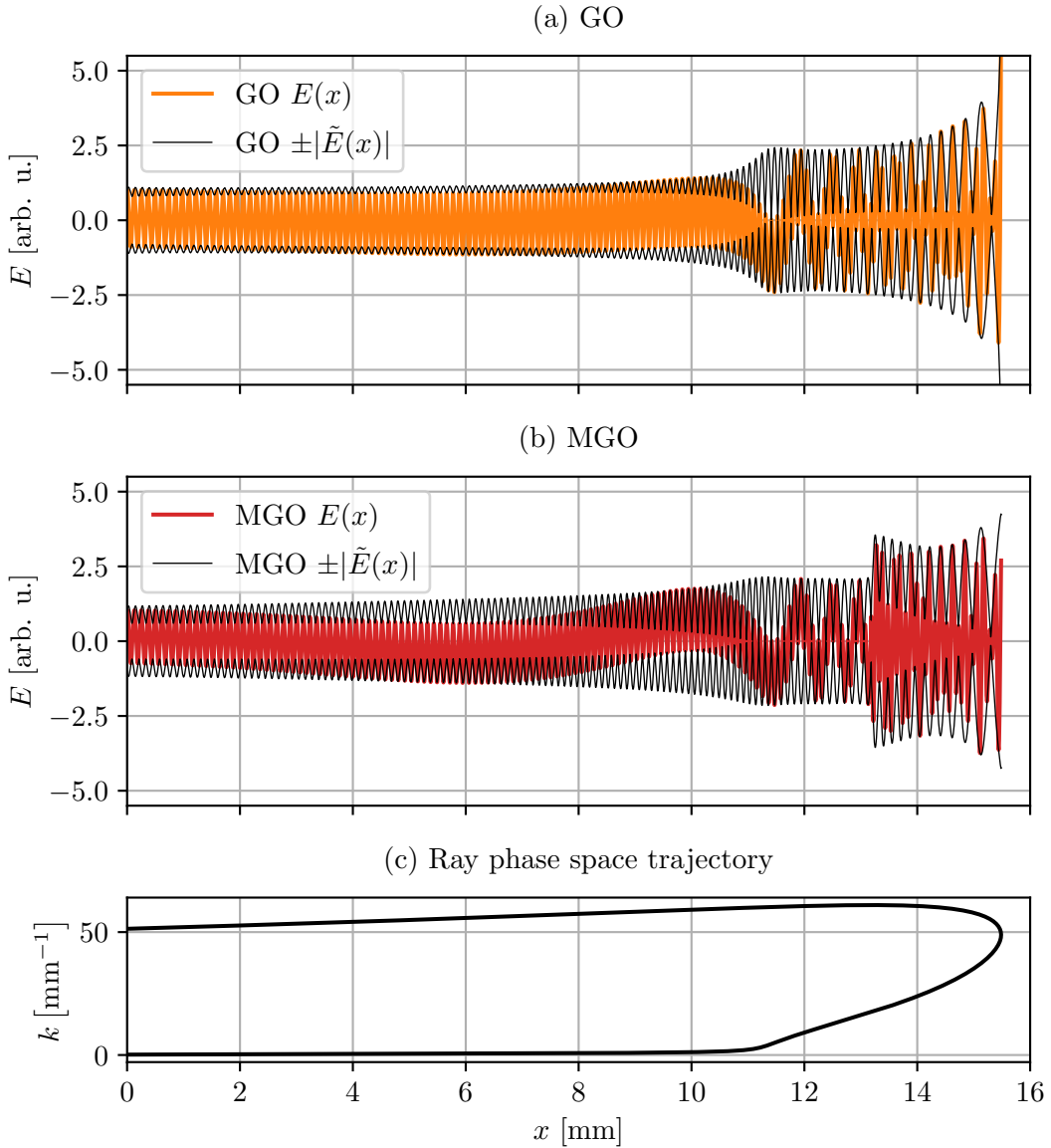


Figure 7.12: MGO field solutions for the XB coupling at the UH layer governed by eqs. (7.34) to (7.37) with a **variable temperature profile**. (a) GO approximation, (b) MGO approximation, (c) Ray phase space trajectory constituting the ray manifold. For (a) and (b) I have shown both the field, $E(x)$, and the amplitude, $|\tilde{E}(x)|$, of the complex field representation (i.e. $E(x) = \text{Re } \tilde{E}(x)$). For the MGO algorithm, I used rational function fits with (nominator, denominator)-degrees, $(L_f, M_f) = (4, 1)$, $(L_\Phi, M_\Phi) = (2, 1)$ to perform the analytic continuation.

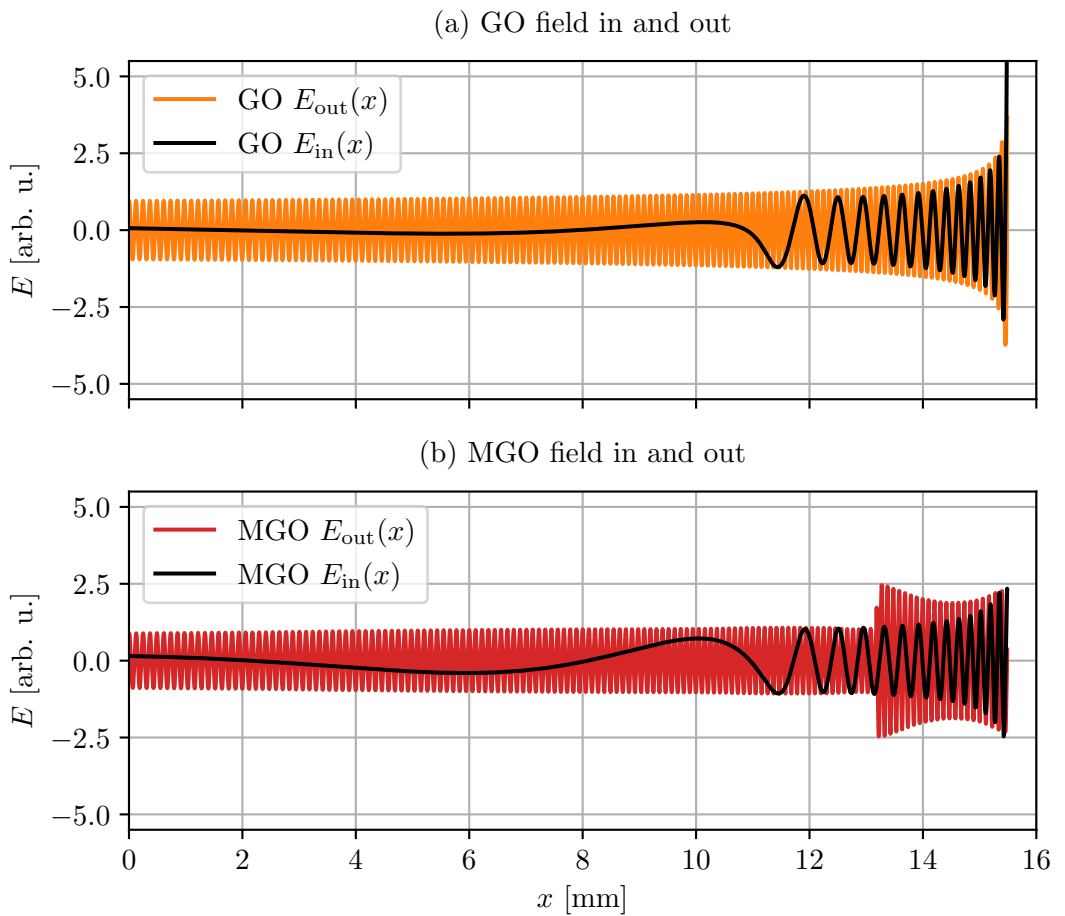


Figure 7.13: Ingoing and outgoing fields for the XB coupling at the UH layer governed byeqs. (7.34) to (7.37) with a **variable temperature profile**. (a) GO approximation, (b) MGO approximation.

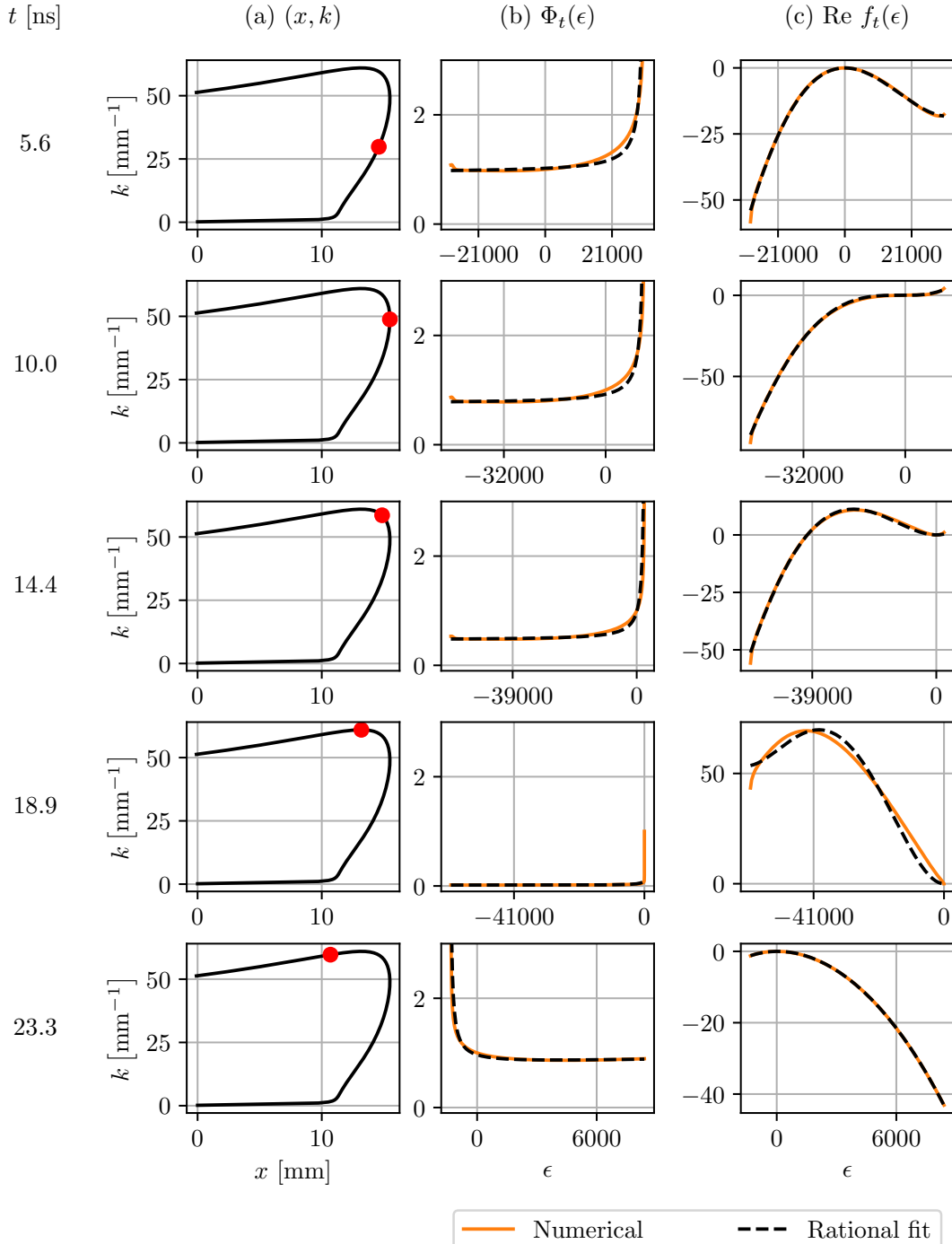


Figure 7.14: Inspection of fits for the XB coupling example with a **variable temperature profile**. (a) Ray manifold with red dot indicating phase space location at time t , (b)-(c) Metaplectically transformed envelope, Φ , and phase factor, f , where I have included the numerical result and the rational function fit with (nominator, denominator)-degrees: $(L_f, M_f) = (4, 1)$ and $(L_\Phi, M_\Phi) = (2, 1)$.

8 Conclusion

In this project I investigated the newly proposed MGO method for simulating wave equations in caustic regions where conventional ray based methods become unreliable. I developed an automated numerical implementation of the method and applied it to the benchmarking examples of Airy's and Weber's equation in 1D. Both examples have a relevant interpretation within plasma physics as well as within quantum mechanics. In both examples I found that the MGO method reconstructed the exact solutions with good accuracy.

Besides the Airy and Weber equation, I also found the algorithm to perform well on the case of X-B-coupling close to the UH layer in a plasma with a constant temperature profile. A case with an entirely different and more complicated dispersion relation and more challenging magnitude scaling of variables compared to the non-dimensionalized examples of Airy's and Weber's equation. Finally, I showed how my current numerical implementation fails to reconstruct the correct field in the more complicated example of X-B-coupling with a varying temperature profile. I suggest three possible contributing error sources behind this behavior. The next obvious steps is to resolve these minor challenges. The curvature-dependent adaptive discretization procedure suggested in Ref. [7, p. 140] and the Gaussian-coherent state formulation suggested in Ref. [7, p. 145] can most likely help resolving these last issues.

The Python code developed as part of this thesis is openly available at GitHub, Ref. [13]. Many technical issues have been solved during the project and hopefully the progress made will benefit coming iterations of MGO codes. Overall I found the MGO method to be a very promising platform for reduced numerical wave modeling. Since the method makes no assumptions on the wave equation this work only scratches the surface of the possible applications of this new reduced modeling paradigm.

Bibliography

- [1] Francis F. Chen. *Introduction to Plasma Physics and Controlled Fusion*. 2015, E1–E1. ISBN: 9783319223087. DOI: 10.1007/978-3-319-22309-4\}11.
- [2] Thomas H. Stix. *Waves in Plasmas*. Springer-Verlag New York, 1992.
- [3] Ernesto Mazzucato. *Electromagnetic waves for thermonuclear fusion research*. eng. World Scientific Publishing Co., 2014, pp. 1–204. ISBN: 9789814571814. DOI: 10.1142/9789814571814.
- [4] I. Y. Dodin et al. “Quasioptical modeling of wave beams with and without mode conversion. I. Basic theory”. In: *Physics of Plasmas* 26.7 (July 2019). ISSN: 10897674. DOI: 10.1063/1.5095076.
- [5] E R Tracy et al. *Ray tracing and beyond: Phase space methods in Plasma wave theory*. eng. Cambridge University Press, 2012, pp. 1–521. ISBN: 9780521768061. DOI: 10.1017/CBO9780511667565.
- [6] David J. Griffiths. *Introduction to quantum mechanics*. eng. Ed. by David J. (David Jeffery) Griffiths, David J. Griffiths, and Darrell F. Schroeter. Third edition. Cambridge, United Kingdom: Cambridge University Press, 2018. ISBN: 9781107189638.
- [7] Nicolas Alexander Lopez. “Metaplectic geometrical optics”. PhD thesis. Princeton University, Nov. 2022.
- [8] N. A. Lopez and I. Y. Dodin. “Metaplectic geometrical optics for ray-based modeling of caustics: Theory and algorithms”. In: *Physics of Plasmas* 29.5 (May 2022). ISSN: 10897674. DOI: 10.1063/5.0082241.
- [9] Richard W. Ziolkowski and Georges A. Deschamps. “Asymptotic evaluation of high-frequency fields near a caustic: An introduction to Maslov’s method”. eng. In: *Radio science* 19.4 (1984), pp. 1001–1025. ISSN: 0048-6604. DOI: 10.1029/RS019i004p01001.
- [10] N. A. Lopez and I. Y. Dodin. “Pseudo-differential representation of the metaplectic transform and its application to fast algorithms”. In: *Journal of the Optical Society of America A* 36.11 (Nov. 2019), p. 1846. ISSN: 1084-7529. DOI: 10.1364/josaa.36.001846.
- [11] N A Lopez and I Y Dodin. “Restoring geometrical optics near caustics using sequenced metaplectic transforms”. In: *New Journal of Physics* 22.8 (Aug. 2020), p. 083078. ISSN: 1367-2630. DOI: 10.1088/1367-2630/aba91a. URL: <https://iopscience.iop.org/article/10.1088/1367-2630/aba91a>.
- [12] Sean M. Donnelly, Nicolas A. Lopez, and I. Y. Dodin. “Steepest-descent algorithm for simulating plasma-wave caustics via metaplectic geometrical optics”. In: *Physical Review E* 104.2 (Aug. 2021). ISSN: 24700053. DOI: 10.1103/PhysRevE.104.025304.
- [13] Rune Højlund. *Github Repository: plasma-ray-tracer*. 2023. URL: <https://github.com/runehoejlund/plasma-ray-tracer.git>.

- [14] Henrik Bruus and Karsten Flensberg. *Many-Body Quantum Theory in Condensed Matter Physics: An Introduction*. eng. Oxford Univ. Press, 2004.
- [15] R Glowinski et al. *Flux Coordinates and Magnetic Field Structure*. Springer-Verlag, 1991, pp. 1–38. ISBN: 9783642755972.
- [16] Ole Christensen. *Functions, Spaces and Expansions*. Springer, 2010. ISBN: 978-0-8176-4979-1.
- [17] L.E. Ballentine. *Quantum mechanics : a modern development*. eng. Singapore: World Scientific, 2015. ISBN: 978-981-4578-57-8.
- [18] George B Arfken, Hans J Weber, and Frank E Harris. *Mathematical Methods for Physicists*. eng. Elsevier Inc., 2013, pp. 1–1205. ISBN: 9780123846549. DOI: 10.1016/C2009-0-30629-7.
- [19] Y Zhou and I Y Dodin. “Weyl calculus on a curved configuration space. Supplementary material for the article ”Quasioptical modeling of wave beams with and without mode conversion. I. Basic theory””. In: *Physics of Plasmas* 26.7 (2019). DOI: 10.1063/1.5095076.
- [20] Henrik Schlichtkrull. *Curves and Surfaces - Lecture Notes for Geometry 1*. Tech. rep. University of Copenhagen, 2011. URL: <http://www.math.ku.dk/>.
- [21] Kenneth Kuttler. *Elementary Differential Equations*. eng. 1st ed. Vol. 1. Textbooks in Mathematics. Milton: CRC Press, 2018. ISBN: 9781138740914. DOI: 10.1201/9781315183138.
- [22] Yu. A. Kravtsov and Yury L. Orlov. *Geometrical Optics of Inhomogeneous Media*. 1st ed. Berlin: Springer, 1990.
- [23] Wikipedia contributors. *Jacobi's formula — Wikipedia, The Free Encyclopedia*. https://en.wikipedia.org/w/index.php?title=Jacobi%27s_formula&oldid=1153212981. 2023. URL: https://en.wikipedia.org/wiki/Jacobi%27s_formula.
- [24] Ian Goodfellow, Yoshua Bengio, and Aaron Courville. *Deep Learning*. MIT Press, 2016. URL: <http://www.deeplearningbook.org>.
- [25] Jorge Nocedal and Stephen J. Wright. *Numerical Optimization*. 2006. ISBN: 978-0387-30303-1.
- [26] Richard L. Burden. *Numerical analysis*. eng. Ed. by J. Douglas. Faires. 7. ed. Pacific Grove, Calif: Brooks/Cole, 2001. ISBN: 0534382169.
- [27] The Theano Development Team et al. “Theano: A Python framework for fast computation of mathematical expressions”. eng. In: (2016). DOI: 10.48550/arxiv.1605.02688.
- [28] Martín Abadi et al. *TensorFlow: Large-Scale Machine Learning on Heterogeneous Systems*. 2015. URL: <https://www.tensorflow.org/>.
- [29] Adam Paszke et al. “PyTorch: An Imperative Style, High-Performance Deep Learning Library”. eng. In: (2019). DOI: 10.48550/arxiv.1912.01703.
- [30] Inc. Wolfram Research. *Mathematica*. Champaign, Illinois, 2023. URL: <https://www.wolfram.com/mathematica>.
- [31] a division of Waterloo Maple Inc. Maplesoft. *Maple*. Waterloo, Ontario, 2022.

- [32] Aaron Meurer et al. “SymPy: symbolic computing in Python”. In: *PeerJ Computer Science* 3 (Jan. 2017), e103. ISSN: 2376-5992. DOI: 10.7717/peerj-cs.103. URL: <https://doi.org/10.7717/peerj-cs.103>.
- [33] The SciPy Community. *SciPy IVP Solver Documentation*. URL: https://docs.scipy.org/doc/scipy/reference/generated/scipy.integrate.solve_ivp.html.
- [34] The SciPy Community. *Scipy Documentation: Flood Fill Algorithm*. URL: https://scikit-image.org/docs/stable/auto_examples/segmentation/plot_floodfill.html.
- [35] The Scipy Community. *SciPy LinearNDInterpolator Documentation*. URL: <https://docs.scipy.org/doc/scipy/reference/generated/scipy.interpolate.LinearNDInterpolator.html>.
- [36] Amparo Gil, Javier Segura, and Nico M Temme. *Numerical Methods for Special Functions*. Society for Industrial and Applied Mathematics, 2007. DOI: 10.1137/1.9780898717822. URL: <https://epubs.siam.org/doi/abs/10.1137/1.9780898717822>.
- [37] J. Heading. *An introduction to phase-integral methods*. eng. Ed. by J. Heading. London: London, 1962.
- [38] The SciPy Community. *SciPy Airy Function Documentation*. URL: <https://docs.scipy.org/doc/scipy/reference/generated/scipy.special.airy.html>.
- [39] B. E. A. Saleh. *Fundamentals of photonics*. eng. Ed. by M. C. Teich. 2nd ed. A John Wiley & Sons: New Jersey, 2007. ISBN: 9780471358329.
- [40] V.P. Maslov and M.V. Fedoriuk. *Semi-Classical Approximation in Quantum : Mechanics*. Ed. by V.P. Maslov and M.V. Fedoriuk. Mathematical Physics and Applied Mathematics ; 7. Dordrecht ; D. Reidel Publ. Co., 1981.
- [41] Joseph B. Keller. “Semiclassical Mechanics”. eng. In: *SIAM review* 27.4 (1985), pp. 485–504. ISSN: 0036-1445. DOI: 10.1137/1027139.
- [42] A Jaun, E R Tracy, and A N Kaufman. “Eikonal waves, caustics and mode conversion in tokamak plasmas”. eng. In: *Plasma physics and controlled fusion* 49.1 (2007), pp. 43–67. ISSN: 0741-3335. DOI: 10.1088/0741-3335/49/1/004.
- [43] Herbert. Goldstein, Charles. Poole, and John. Safko. *Classical mechanics*. eng. Ed. by Herbert. Goldstein et al. 3. ed. Upper Saddle River, NJ: Pearson / Addison-Wesley, 2002. ISBN: 0321188977.
- [44] Leslie Copley. *Mathematics for the Physical Sciences*. 2014.
- [45] Cheng-De Zheng and Zhi-Bin Li. *Generalized multivariate matrix Padé approximants*. Tech. rep. 2023.
- [46] Søren Kjer Hansen. *Parametric Decay Instabilities in the Electron Cyclotron Resonance Heating Beams at ASDEX Upgrade*. eng. 2019.
- [47] Mads Givskov Senstius. “Simulations of Three-Wave Interactions in Microwave Heated Fusion Plasmas”. eng. PhD thesis. 2020.
- [48] F. W. Crawford and J. A. Tataronis. “Absolute instabilities of perpendicularly propagating cyclotron harmonic plasma Waves”. In: *Journal of Applied Physics* 36.9 (1965), pp. 2930–2934. ISSN: 00218979. DOI: 10.1063/1.1714609.

- [49] Endre Süli and D. F. (David Francis) Mayers. *An introduction to numerical analysis*. Cambridge University Press, 2003, p. 433. ISBN: 9780521810265.

A Appendix

A.1 Notation

For reference I give here an overview of the notation used in this thesis:

- $\mathbf{:=}$ denotes a definition.
- N -dimensional vectors are written with bold symbols: $\mathbf{a} \in \mathbb{C}^N$.
- $M \times N$ matrices are written with bold, italic and sans-serif typeface $\mathbf{A} \in \mathbb{C}^{M \times N}$. Matrix elements are written in sans serif italic A_{ij} .
- A real- or complex-valued function of a function (i.e. a functional) is written with square brackets around the argument, e.g. $f[x(\tau)]$.
- Gradients of scalar valued functions are written in the short hand notation $\partial_{\mathbf{x}} f$. For instance, if $f : \mathbb{R}^N \rightarrow \mathbb{R}$ the gradient is defined as:

$$\partial_{\mathbf{x}} f := \begin{pmatrix} \frac{\partial f}{\partial x_1} \\ \frac{\partial f}{\partial x_2} \\ \vdots \\ \frac{\partial f}{\partial x_N} \end{pmatrix} \quad (\text{A.1})$$

For vector valued functions $\mathbf{f} : \mathbb{R}^N \rightarrow \mathbb{R}^M$ I write the generalized gradient (transposed jacobian matrix) in the same way:

$$\partial_{\mathbf{x}} \mathbf{f} := \begin{pmatrix} \frac{\partial f_1}{\partial x_1} & \frac{\partial f_2}{\partial x_1} & \dots & \frac{\partial f_M}{\partial x_1} \\ \frac{\partial f_1}{\partial x_2} & \frac{\partial f_2}{\partial x_2} & \dots & \frac{\partial f_M}{\partial x_2} \\ \vdots & \vdots & & \vdots \\ \frac{\partial f_1}{\partial x_N} & \frac{\partial f_2}{\partial x_N} & \dots & \frac{\partial f_M}{\partial x_N} \end{pmatrix} \quad (\text{A.2})$$

I do not distinguish between functions of one or more variables when writing the derivative. So for both $f(x), f : \mathbb{R} \rightarrow \mathbb{R}$ and $f(x, y), f : \mathbb{R}^2 \rightarrow \mathbb{R}$, I write the derivative with respective to x as $\partial_x f$. However, I do distinguish between partial and total derivatives for a functional $f[t, g(t)]$ which has an indirect dependence on t . The total derivative d_t is defined by the chain rule:

$$d_t f[t, g(t)] := \partial_t f[t, g(t)] + (\partial_t g) \partial_g f[t, g(t)]. \quad (\text{A.3})$$

- If nothing is written, integrals are assumed to integrate over all space and time, e.g. $\int dt := \int_{-\infty}^{\infty} dt$.

- Volume integrals are denoted by a bold symbol infinitesimal element:

$$\int d\mathbf{x} := \int_{-\infty}^{\infty} dx_1 \int_{-\infty}^{\infty} dx_2 \cdots \int_{-\infty}^{\infty} dx_N,$$

where $\mathbf{x} \in \mathbb{R}^N$.

- Vectors are assumed to be column matrices in Cartesian coordinates and dot products between vectors \mathbf{a}, \mathbf{b} are either indicated with $\mathbf{a} \cdot \mathbf{b}$ or $\mathbf{a}^T \mathbf{b}$. The T denotes the transpose.
- I use implicit outer products between vectors such that $\mathbf{ab} := \mathbf{a} \otimes \mathbf{b}$. The outer product is defined by satisfying:

$$\begin{aligned} (\mathbf{a} \cdot \mathbf{bc}) &= (\mathbf{a} \cdot \mathbf{b})\mathbf{c} \\ (\mathbf{bc} \cdot \mathbf{a}) &= \mathbf{b}(\mathbf{c} \cdot \mathbf{a}). \end{aligned}$$

Note that the two expressions are not equal so dotting a tensor (i.e. an outer product) from the left is not the same as dotting from the right. Since I use Cartesian coordinates, the outer product has a simple matrix representation. For instance for $\mathbf{a}, \mathbf{b}, \mathbf{c} \in \mathbb{R}^3$:

$$[\mathbf{bc}] = \begin{pmatrix} b_1 \\ b_2 \\ b_3 \end{pmatrix} \begin{pmatrix} c_1 & c_2 & c_3 \end{pmatrix} = \begin{pmatrix} b_1 c_1 & b_1 c_2 & b_1 c_3 \\ b_2 c_1 & b_2 c_2 & b_2 c_3 \\ b_3 c_1 & b_3 c_2 & b_3 c_3 \end{pmatrix}.$$

Written as matrix products, the dot products with tensors and vectors are:

$$\mathbf{a} \cdot \mathbf{bc} = \mathbf{cb}^T \mathbf{a} = [\mathbf{bc}]^T \mathbf{a}, \quad (\text{A.4})$$

$$\mathbf{bc} \cdot \mathbf{a} = \mathbf{bc}^T \mathbf{a} = [\mathbf{bc}]\mathbf{a}, \quad (\text{A.5})$$

$$\mathbf{ab} \cdot \mathbf{cd} = \mathbf{a}(\mathbf{b} \cdot \mathbf{c})\mathbf{d} = \mathbf{ab}^T \mathbf{cd}^T = [\mathbf{ab}][\mathbf{cd}]. \quad (\text{A.6})$$

A special case is outer products with the gradient $\partial_{\mathbf{x}}$. The outer product $\partial_{\mathbf{x}} \mathbf{f}$ gives in my Cartesian coordinates the matrix of eq. (A.2). More generally, the parentheses determine what the differential operator acts upon. To take a few examples with $\mathbf{f} : \mathbb{R}^N \rightarrow \mathbb{R}^N, \mathbf{v} : \mathbb{R}^N \rightarrow \mathbb{R}^N$:

$$\mathbf{v} \cdot (\partial_{\mathbf{x}} \mathbf{f}) = (\mathbf{v} \cdot \partial_{\mathbf{x}}) \mathbf{f} = \sum_{i=1}^N v_i \partial_{x_i} \mathbf{f} = [\partial_{\mathbf{x}} \mathbf{f}]^T \mathbf{v}. \quad (\text{A.7a})$$

$$(\partial_{\mathbf{x}} \mathbf{f}) \cdot \mathbf{v} = \sum_{i=1}^N (\partial_{x_i} f_i) v_i = [\partial_{\mathbf{x}} \mathbf{f}] \mathbf{v} \quad (\text{A.7b})$$

$$\partial_{\mathbf{x}}(\mathbf{f} \cdot \mathbf{v}) = \partial_{\mathbf{x}} \sum_{i=1}^N f_i v_i = \sum_{i=1}^N (\partial_{x_i} f_i) v_i + f_i (\partial_{x_i} v_i) = (\partial_{\mathbf{x}} \mathbf{f}) \cdot \mathbf{v} + (\partial_{\mathbf{x}} \mathbf{v}) \cdot \mathbf{f} = [\partial_{\mathbf{x}} \mathbf{f}] \mathbf{v} + [\partial_{\mathbf{x}} \mathbf{v}] \mathbf{f} \quad (\text{A.7c})$$

- The $:$ operation denotes the double dot product (Ref. [15]):

$$\mathbf{ab} : \mathbf{cd} = \sum_{ij} a_i b_j c_j d_k, \quad \mathbf{abc} : \mathbf{def} = \sum_{ijk} a_i b_j c_k d_k e_j f_i, \dots \quad (\text{A.8})$$

In particular I can write the matrix contraction with the double dot product:

$$\mathbf{kk} : \mathbf{M} = \sum_{ij} k_i k_j M_{ij} = \mathbf{k}^T \mathbf{M} \mathbf{k}. \quad (\text{A.9})$$

And the Taylor expansion of $f(\mathbf{x})$ can be written as

$$f(\mathbf{x} + \mathbf{a}) = f(\mathbf{x}) + \frac{1}{2} \mathbf{aa} : \partial_{\mathbf{x}} \partial_{\mathbf{x}} f(\mathbf{x}) + \frac{1}{3!} \mathbf{aaa} : \partial_{\mathbf{x}} \partial_{\mathbf{x}} \partial_{\mathbf{x}} f(\mathbf{x}) + \dots \quad (\text{A.10 Taylor})$$

- Operators are indicated with a hat: \hat{A} .
- I use Dirac bracket notation introduced in section 3.1 of chapter 3.
- The Weyl symbol of an operator, introduced in section 3.2 of chapter 3, will be written in a calligraphic typeface $\mathcal{A}(\mathbf{z})$.

Finally, as is common in physics, variables are often introduced without explicit definition of the set to which they belong. E.g. the dimensions of physical quantities such as the position $\mathbf{x} \in \mathbb{R}^3$ or the velocity $\mathbf{v} \in \mathbb{R}^3$, are not stated explicitly, but assumed known from the context (or from the physical world in which we live). Similarly, functions are defined without explicitly stating their domain and codomain. This saves valuable space and allows convenient abuse of notation, such that I can e.g. represent a field¹ by using the same letter ψ to denote both its' Hilbert space vector $|\psi\rangle$, the field's position representation $\psi(\mathbf{x})$ and it's momentum representation $\psi(\mathbf{k})$.

¹A field is simply a function of position and time.

A.2 Acronyms

Below is a list of the acronyms used in the thesis.

AAH Altar-Appleton-Hartree

BC boundary condition

CMA Clemmow-Mullay-Allis

EBW electron Bernstein wave

EM electromagnetic

GO geometrical optics

IVP initial value problem

MGO metaplectic geometrical optics

NIMT near identity metaplectic transform

ODE ordinary differential equation

ONB orthonormal basis

PDE partial differential equation

QHO quantum harmonic oscillator

RHS right hand side

RMS root mean square

SPA stationary phase approximation

SVD singular value decomposition

UH upper hybrid

B Gauss Quadrature

In Ref. [12], Donnelly, Lopez, and Dodin propose a numerical method for evaluating the inverse metaplectic transform, eq. (6.40), using Gauss-Freud quadrature along contours of steepest descent in the complex plane. In this appendix I give a short introduction to the Gauss quadrature method. For further references the reader is encouraged to consult Refs. [36, 12].

B.1 Polynomial Interpolation

An elementary tool in numerical analysis is the ability to approximate a function $f(x)$ by a n 'th degree polynomial: $f(x) \approx P_n(x)$. If the derivatives of $f(x)$ up to degree n are known, then the Taylor expansion provides a method of achieving this. If instead the function values at $n + 1$ points are known we can use the method of Lagrange interpolation (Refs. [49, 36]):

Theorem B.1.1 (Lagrange Interpolation). Let f be a function defined on $[a, b] \subset \mathbb{R}$ with known values at $x_0, \dots, x_n \in [a, b]$, $n \in \mathbb{N}$. Then there exists a unique polynomial $P_n(x)$ of degree n which satisfies:

$$f(x_j) = P_n(x_j) \quad \forall j = 0, \dots, n \quad (\text{B.1a})$$

The polynomial is known as the Lagrange interpolation of $f(x)$ and is given by:

$$P_n(x) = \sum_{i=0}^n f(x_i) \ell_i(x), \quad (\text{B.1b})$$

where $\ell_i(x)$ is the i 'th Lagrange polynomial of degree n defined by

$$\ell_i(x) \equiv \prod_{\substack{l=0 \\ l \neq i}}^n \frac{x - x_l}{x_i - x_l}. \quad (\text{B.1c})$$

Proof. By noticing that $\ell_i(x_j) = \delta_{ij}$ it is straightforward to check that the interpolation in Eq. (B.1b) does indeed satisfy Eq. (B.1a). Uniqueness is proved by contradiction: Assume there exists a polynomial $Q_n \neq P_n$ of degree n satisfying Eq. (B.1a). Then $P_n - Q_n$ is also a n 'th degree polynomial. But $P_n - Q_n$ must have $n + 1$ distinct roots at x_0, \dots, x_n . This is one too many roots for a nontrivial n 'th degree polynomial according to the fundamental theorem of algebra. Thus, the only possibility is that $P_n - Q_n = 0$ in contradiction with the assumption that $P_n \neq Q_n$. \square

If f is a polynomial of at most degree n then its' Lagrange interpolation is of course exact. However, if this is not the case there exists a nice theorem giving a boundary of the error encountered by approximation f with P_n :

Theorem B.1.2 (Lagrange Interpolation Error). If f is $n + 1$ times differentiable and continuous on $[a, b]$, then for each $x \in [a, b]$ there exists a $\xi \in [a, b]$ such that the error $R_n(x)$ of the Lagrange interpolation $P_n(x)$ is:

$$R_n(x) \equiv f(x) - P_n(x) = \frac{f^{(n+1)}(\xi)}{(n+1)!} \prod_{j=0}^n (x - x_j). \quad (\text{B.2a})$$

Moreover, for all $x \in [a, b]$:

$$|R_n(x)| = |f(x) - P_n(x)| \leq \frac{\max_{\xi \in [a,b]} |f^{(n+1)}(\xi)|}{(n+1)!} \left| \prod_{l=0}^n (x - x_l) \right|. \quad (\text{B.2b})$$

Proof. The proof of Eq. (B.2a) follows from Rolle's Theorem and can be found e.g. in [49, p. 183]. The absolute bound in Eq. (B.2b) follows directly from (B.2a). \square

B.2 Sturm-Liouville Theory and Orthogonal Polynomials

Sturm-Liouville Theory is the study of second order ODEs formulated as eigenvalue problems equipped with BCs on the general form, Ref. [18, p. 384]:

$$\mathcal{L}(x)\psi(x) \equiv \left[p_0(x) \frac{d^2}{dx^2} + p_1(x) \frac{d}{dx} + p_2(x) \right] \psi(x) = \lambda \psi(x) \quad (\text{B.3a})$$

$$\psi(a) = \psi_a, \quad \psi(b) = \psi_b, \quad (\text{B.3b})$$

Possible solutions of Eq. (B.3) are restricted to exist in a Hilbert space, \mathcal{H} , defined by the BCs of Eq. (B.3b). If we define the inner product of the Hilbert space as the square integral:

$$\langle \psi_1 | \psi_2 \rangle \equiv \int_a^b dx \psi_1^*(x) \psi_2(x), \quad (\text{B.4})$$

then it straightforward to show that the operator $\mathcal{L}(x)$ will be hermitian iff $p'_0(x) = p_1(x)$ and sufficient BCs are met (prime, $'$, denotes differentiation). That is, given $\psi_1, \psi_2 \in \mathcal{H}$:

$$\begin{aligned} \langle \psi_1 | \mathcal{L} \psi_2 \rangle &= \langle \mathcal{L} \psi_1 | \psi_2 \rangle \\ &\Updownarrow \\ p'_0 &= p_1 \quad \text{and} \quad [p_0(\psi_1^* \psi'_2 - \psi_1^{*\prime} \psi_2)]_{x=a}^{x=b} = 0. \end{aligned} \quad (\text{B.5})$$

Note, how both Dirichlet BCs, $\psi(a) = \psi(b) = 0$ and Neumann BCs $\psi'(a) = \psi'(b) = 0$ satisfy the requirements for hermiticity. With the hermiticity of \mathcal{L} follows a range of desired properties, including the existence of a complete eigenbasis which can be used to expand any solution [18, Ch. 8]. However, even in the case that \mathcal{L} is not hermitian with respect to the simple inner product, Eq. (B.4), we may introduce a non-negative weight function, $\omega(x)$, to come to the rescue:

$$\langle \psi_1 | \psi_2 \rangle_\omega \equiv \int_a^b dx \omega(x) \psi_1^*(x) \psi_2(x). \quad (\text{B.6})$$

If we multiply both sides of the eigenvalue problem, Eq. (B.3a) with $\omega(x)$ we get

$$\omega(x)\mathcal{L}(x)\psi(x) = \left[\omega(x)p_0(x)\frac{d^2}{dx^2} + \omega(x)p_1(x)\frac{d}{dx} + \omega(x)p_2(x) \right]\psi(x) = \omega(x)\lambda\psi(x).$$

When comparing this with Eq. (B.5) it is evident that the new operator, $\omega(x)\mathcal{L}(x)$, is hermitian iff

$$(\omega p_0)' = \omega p_1 \quad \text{and} \quad (\text{B.7})$$

$$[\omega p_0(\psi_1^*\psi_2' - \psi_1^{*\prime}\psi_2)]_{x=a}^{x=b} = 0. \quad (\text{B.8})$$

The first of these requirements, Eq. (B.7), can be satisfied with the weight function

$$\omega(x) = \frac{A}{p_0(x)} \exp\left(\int^x dx' \frac{p_1(x')}{p_0(x')}\right), \quad (\text{B.9})$$

where $A \in \mathbb{C}$ is a complex constant which, if possible, should be chosen such that $\omega(x)$ is non-negative for all $x \in (a, b)$.

Different second order ODEs are categorized and named depending on their form of p_0, p_1, p_2 . For each different type of Sturm-Liouville problem, Eq. (B.9), allows us to find a weight $\omega(x)$ which hermitizes the differential operator and thereby yields a family of orthogonal eigenfunctions (the Gram-Schmidt procedure may be used for orthogonalisation in case of eigenvalue degeneracy). Often the eigenfunctions are polynomials. Based on Ref. [18, p. 345, Table 7.1 and Ch. 8.2] we have listed some important examples of Sturm-Liouville problems with polynomial eigenfunctions in Table B.1. Note how the intervals $[a, b]$ in Table B.1 are defined to ensure the hermiticity BC, Eq. (B.8), i.e. $\omega(a)p_0(a) = \omega(b)p_0(b) = 0$.

| Name | \mathcal{L} | A in (B.9) | weight, $\omega(x)$ | $[a, b]$ |
|-----------|---|--------------|---------------------|---------------------|
| Laguerre | $x\frac{d^2}{dx^2} + (1-x)\frac{d}{dx} + a$ | 1 | e^{-x} | $[0, \infty]$ |
| Hermite | $\frac{d^2}{dx^2} - 2x\frac{d}{dx} + 2\alpha$ | 1 | e^{-x^2} | $[-\infty, \infty]$ |
| Legendre | $(1-x^2)\frac{d^2}{dx^2} - 2x\frac{d}{dx} + l(l+1)$ | -1 | 1 | $[-1, 1]$ |
| Chebyshev | $(1-x^2)\frac{d^2}{dx^2} - x\frac{d}{dx} + n^2$ | i | $(1-x^2)^{-1/2}$ | $[-1, 1]$ |

Table B.1: Examples of second order ODEs and associated inner product weights given by Eq. (B.9). Each ODE has a complete set of orthogonal eigenfunctions, which in all these cases are polynomials.

B.3 Gaussian Quadrature

We now turn our attention to the determination of definite integrals on the form

$$\int_a^b dx f(x). \quad (\text{B.10})$$

From the Sturm-Liouville theory in Section B.2, we know that we can choose a basis of polynomials, $\{p_i\}_{i=0}^\infty$, which are orthogonal on the interval $[a, b]$. That is

$$\langle p_i | p_j \rangle_\omega = \langle p_i | p_i \rangle_\omega \delta_{i,j} \quad (\text{B.11})$$

Assume we have such a basis, $\{p_i\}_{i=0}^\infty$, of real-valued polynomials with a corresponding non-negative weight function ω . For a start we will assume that $f(x)$ is simple enough to be factorized as:

$$f(x) = \omega(x)g(x), \quad \deg(g) = 2n - 1 \quad (\text{B.12})$$

where the latter notation means that $g(x)$ is a polynomial of degree $2n - 1$.

Now, consider the n 'th polynomial, p_n . The orthogonality of $\{p_i\}_{i=0}^\infty$ means that any polynomial, q , with degree lower than n will be orthogonal to p_n . That is:

$$\text{If } \deg(q) \leq n - 1 \Rightarrow \langle q | p_n \rangle_\omega = \sum_{i=0}^{n-1} \langle q | p_i \rangle_\omega \langle p_i | p_n \rangle_\omega = 0 \quad (\text{B.13})$$

From polynomial division of $g(x)$ and $p_n(x)$ we know that there exists polynomials q and r such that:

$$g(x) = p_n(x)q(x) + r(x), \quad (\text{B.14a})$$

$$\deg(p_n) = n, \quad \deg(q) \leq n - 1, \quad \deg(r) \leq n - 1 \quad (\text{B.14b})$$

Using the factorization in Eq. (B.12) with the relations in Eqs. (B.13) and (B.14) the integral of interest, Eq. (B.10), becomes:

$$\int_a^b dx f(x) = \int_a^b dx \omega(x)g(x) = \langle 1 | g \rangle_\omega = \langle q | p_n \rangle_\omega + \langle 1 | r \rangle_\omega = \langle 1 | r \rangle_\omega. \quad (\text{B.15})$$

Thus, evaluating the integral has been turned into a problem of evaluating the weighted integral of $r(x)$. This can be done elegantly by letting x_1, \dots, x_n be the n roots of $p_n(x)$, i.e. such that $p_n(x_i) = 0 \forall x_i$. This means, that p_n may be factorized on the form:

$$p_n(x) = a_n \prod_{l=1}^n (x - x_l). \quad (\text{B.16})$$

The trick now is to interpolate the polynomial $r(x)$ through the n roots of $p_n(x)$. Since the polynomial $r(x)$ is at most of degree $n - 1$, it is uniquely determined by its' Lagrange polynomial interpolation through the n roots of p_n given by:

$$r(x) = \sum_{j=1}^n r(x_j) \ell_j(x). \quad (\text{B.17})$$

Here $\ell_j(x)$ is the j 'th Lagrange polynomial of degree $n-1$ defined from the n interpolation points:

$$\ell_j(x) = \prod_{\substack{l=1 \\ l \neq j}}^n \frac{x - x_l}{x_j - x_l} = \left(\frac{1}{x - x_j} \prod_{l=1}^n (x - x_l) \right) \left(\prod_{\substack{l=1 \\ l \neq j}}^n (x_j - x_l) \right)^{-1} \quad (\text{B.18})$$

We can rewrite the first product on the RHS in the Lagrange polynomial above using Eq. (B.16):

$$\frac{1}{x - x_j} \prod_{l=1}^n (x - x_l) = \frac{1}{x - x_j} \frac{p_n(x)}{a_n} \quad (\text{B.19})$$

If we take the limit of this as $x \rightarrow x_j$ using L'Hôpital's rule we get an expression for the second product in the Lagrange polynomial of Eq. (B.18):

$$\prod_{\substack{l=1 \\ l \neq j}}^n (x_j - x_l) = \lim_{x \rightarrow x_j} \left[\frac{1}{x - x_j} \prod_{l=1}^n (x - x_l) \right] = \lim_{x \rightarrow x_j} \left[\frac{1}{x - x_j} \frac{p_n(x)}{a_n} \right] = \frac{p'_n(x_j)}{a_n}. \quad (\text{B.20})$$

Thus, the Lagrange polynomial of Eq. (B.18) is:

$$\ell_j(x) = \frac{p_n(x)(x - x_j)^{-1}}{p'_n(x_j)}. \quad (\text{B.21})$$

Putting Eqs. (B.15), (B.17), (B.21) together we get:

$$\int_a^b dx f(x) = \int_a^b dx \omega(x) g(x) = \sum_{j=1}^n r(x_j) \langle 1 | \ell_j(x) \rangle = \sum_{j=1}^n \frac{\langle p_n(x) | (x - x_j)^{-1} \rangle}{p'_n(x_j)} r(x_j), \quad (\text{B.22})$$

As our final piece, note that since x_j are roots of p_n :

$$g(x_j) = p_n(x_j) q(x_j) + r(x_j) = r(x_j) \quad (\text{B.23})$$

With this, we arrive at a simple n -point sum for evaluating the definite integral of Eq. (B.22):

$$\int_a^b dx f(x) = \sum_{j=1}^n w_j \frac{f(x_j)}{\omega(x_j)}, \quad (\text{B.24a})$$

$$\text{where } w_j \equiv \frac{\langle p_n | (x - x_j)^{-1} \rangle_\omega}{p'_n(x_j)}. \quad (\text{B.24b})$$

In the formula above, p_n is the n 'th polynomial in a family of real-valued orthogonal polynomials, x_1, \dots, x_n are the n roots of p_n and $\omega(x)$ is the appropriate non-negative

weight function, which ensures orthogonality of the polynomials on the interval $[a, b]$ (see examples of weight functions in Table B.1). We have thereby reduced the integral to a finite sum. The Gauss quadrature method is also applicable to functions which are not polynomials, but in these cases it introduces a finite error. The reader may consult Ref. [36] for further reading on the quadrature method in general or Ref. [12] for specific formulas related to the evaluation of the metaplectic transform and for information on the Freud-quadratures used there.

Technical
University of
Denmark

Brovej, Building 118
2800 Kgs. Lyngby
Tlf. 4525 1700

<https://www.fysik.dtu.dk/english>